AFGL-TR-77-0098 (I)

(12)

ADA044161

ROTATING GRAVITY GRADIOMETER DEVELOPMENT - Volume 1

C.B. Ames, R.B. Clark, P.M. LaHue, and R.W. Peterson

Hughes Research Laboratories
3011 Malibu Canyon Road
Malibu, CA 90265

April 1977

Final Report
Period 1 August 1975 through 31 January 1977

Approved for public release; distribution unlimited.

Sponsored by
Defense Advanced Research Projects Agencies (DOD)
ARPA ORDER NO. 2895

DDC

AIR FORCE GEOPHYSICS LABORATORY
AIR FORCE SYSTEMS COMMAND
UNITED STATES AIR FORCE
HANSCOM AFB, MASSACHUSETTS 01731

AD No.
DDC FILE COPY

The views and conclusions contained in this document are those of the authors and should not be interpreted as necessarily representing the official policies, either expressed or implied, of the Defense Advanced Research Projects Agency or the U.S. Government.

AIR FORCE (1) JULY 26, 1977--195

Qualified requestors may obtain additional copies from the Defense Documentation Center. All others should apply to the National Technical Information Service.

UNCLASSIFIED

SECURITY CLASSIFICATION OF THIS PAGE (When Data Entered)

REPORT DOCUMENTATION PAGE		READ INSTRUCTIONS BEFORE COMPLETING FORM
1. REPORT NUMBER AFGL-TR-77-0098(I)	2. GOVT ACCESSION NO.	3. RECIPIENT'S CATALOG NUMBER
4. TITLE (and Subtitle) ROTATING GRAVITY GRADIOMETER DEVELOPMENT, Volume 1		5. TYPE OF REPORT & PERIOD COVERED Final Report 1 Aug 75 - 31 Jan 77 6. PERFORMING ORG. REPORT NUMBER
7. AUTHOR(s) C.B. Ames, R.B. Clark, P.M. LaHue, and R.W. Peterson		8. CONTRACT OR GRANT NUMBER(s) F19628-76-C-0107
9. PERFORMING ORGANIZATION NAME AND ADDRESS Hughes Research Laboratories 3011 Malibu Canyon Road Malibu, CA 90265		10. PROGRAM ELEMENT, PROJECT, TASK AREA & WORK UNIT NUMBERS 76000601 62701E
11. CONTROLLING OFFICE NAME AND ADDRESS Air Force Geophysics Laboratory Hanscom AFB, Massachusetts 01731 Monitor/Jack A. Cook, Lt. Col. USAF/LW		12. REPORT DATE April 1977 13. NUMBER OF PAGES 180
14. MONITORING AGENCY NAME & ADDRESS (if different from Controlling Office) Air Force Geophysics Laboratory L.G. Hanscom Field Bedford, Massachusetts		15. SECURITY CLASS (of this report) UNCLASSIFIED 15a. DECLASSIFICATION DOWNGRADING SCHEDULE

16. DISTRIBUTION STATEMENT (of this Report)

Approved for public release; distribution unlimited

DDC
RECEIVED
SEP 15 1977
B

17. DISTRIBUTION STATEMENT (of the abstract entered in Block 20, if different from Report)

18. SUPPLEMENTARY NOTES

This research was sponsored by the Defense Advanced Research Projects Agencies (DOD) ARPA Order No. 2895

19. KEY WORDS (Continue on reverse side if necessary and identify by block number)

Gravity Gradiometer	Airborne Gradiometer
Gravitational Mass Sensor	Vertical Deflection
Gravitational Gradient Sensor	Motion Isolation and Stabilization
Gravity Mapping	Inertial Guidance
Mass Detection	Navigation

20. ABSTRACT (Continue on reverse side if necessary and identify by block number)

The purpose of this contract was to further the development of the Hughes Rotating Gravity Gradiometer (RGG); this effort is a direct continuation of two prior Air Force contracts (F19628-72-C-0222 and F19628-75-C-0201). The stated performance objective for these contracts was the design, construction and demonstration of the Rotating Gravity Gradiometer capable of operating in an airborne environment and producing no more than one (1) Eötvös Unit (EU) of noise, at an

DD FORM 1 JAN 73 1473 EDITION OF 1 NOV 65 IS OBSOLETE

UNCLASSIFIED

SECURITY CLASSIFICATION OF THIS PAGE (When Data Entered)

equivalent ten second integration time, in the determination of the components of a gravity gradient tensor.

The scope of effort in this contract was limited to studies and performance tests and demonstrations in the laboratory environment. Two RGG sensors were involved. The first, RGG-1, was built in 1974 and 1975 under the prior contracts. The second, RGG-2, was designed and built during the course of this contract. The initial scope of work included various tasks to test and modify RGG-1, with the goal of determining configuration changes to be incorporated in RGG-2.

The design for RGG-2 was frozen in April 1976; however, RGG-1 testing continued through November 1976. RGG-2 was assembled and ready for grooming and initial performance evaluation by December 1976. Since this contract was completed on 31 January 1977, the period of RGG-2 performance evaluation was limited to a brief span of a few weeks. However, during that short time, it was conclusively demonstrated that significant progress had been made toward achieving the ultimate performance goals.

Specifically, the performance results obtained with RGG-2 demonstrate that: (1) The design goals have been met for thermal and electronics noise. (2) The sensor output noise goals have nearly been met for the vertical spin axis orientation. (3) Considerable optimism is warranted that the sensor output noise goals can be met for the horizontal spin axis orientation. (4) Continued development is both necessary and warranted.

A second purpose of this contract was to study the requirements of a platform needed to stabilize up to three RGG sensors in an airborne mapping environment. The results of this study, conducted under subcontract by Incosym, Inc., is reported in Volume II of this Final Report. The study results are encouraging, particularly because an existing DoD platform has been identified as being suitable to support a triad of RGG sensors.

In summary, the availability of a platform and the performance success of RGG-2 permit immediate consideration of a follow-on program which would test and demonstrate all the components of a gravity gradiometer system. It is the recommendation of this report that the Hughes RGG sensor be integrated with a platform at the earliest possible time, and tested in the laboratory environment. It is also the recommendation of this report that the RGG-1 sensor be retrofitted up to the RGG-2 configuration to permit simultaneous development and test efforts.

TABLE OF CONTENTS

SECTION		PAGE
	LIST OF ILLUSTRATIONS	5
1	SUMMARY AND ACCOMPLISHMENTS	9
	A. Introduction	9
	B. RGG Sensor Development Overview	10
2	RGG-2 DESIGN FEATURES	17
	A. Mechanical Configuration	17
	B. Assembly Techniques	64
	C. Electrical	86
3	RGG ENVIRONMENTAL OPERATIONAL COMPENSATION CONCEPTS	93
	A. Angular Rate Compensation	93
	B. DTG Automatic Temperature Compensation Concept	98
4	RGG-2 SYSTEM OUTPUT DATA FORMAT	103
5	NEW EXTERNAL ELECTRONICS	105
	A. Temperature Control	105
	B. New Analog Rotor Speed Control Servo	107
	C. Signal Conditioner Improvements	107
	D. Built-In Monitors	108
	E. Printing TERMINAL	108
6	RGG-1 BALANCE TUBE INSPECTION	109

SECTION		PAGE
7	STATIC BALANCE ADJUSTMENTS OF RGG-2	113
	A. The Tare Weight Concept	113
	B. Balance Screw Adjustment Computation	113
	C. Adjustment Trial Results	114
8	DYNAMIC BALANCING OF THE RGG-2 ROTOR	117
9	RGG-2 TEST DATA SUMMARY	121
	A. RGG-2 Orientation Test	121
	B. Spin Axis Vertical: Transient Response and 5 Hour Run	124
	C. Spin Axis Horizontal: Transient Response and 3 Hour Run	129
	D. Angular Rate Scale Factor Tests	129
	E. Windage Tests	133
	APPENDIX A – Windage Effects on Rotating Gravity Gradiometer at Low Pressure	135
	APPENDIX B – RGG-2 Data Printout Description and Format	145
	APPENDIX C – Vibration Testing of the Non-Spinning RGG for Coefficient Estimation and Compensation	151
	APPENDIX D – Tare Weight Selection for Initial Arm Balancing	169

LIST OF ILLUSTRATIONS

FIGURE		PAGE
2-1	Pivot-arm and end mass assembly of RGG-2	18
2-2	Inner rotor end bells of RGG-2	19
2-3	Sensing structure of RGG-2	20
2-4	Special billet and nearly completed pivot-arm	21
2-5	Box for transporting pivot-arm	23
2-6	Sensing structure of RGG-1 with an inner rotor removed	24
2-7	Arm compliance minimized	27
2-8	Set-up for lateral deflection testing of pivots	28
2-9	Cross section of RGG-2 rotor assembly	33
2-10	Transducer mounts, stops for end masses, and thermistor mount	35
2-11	Arrangement of transducer mounts and counterweights	36
2-12	Anisoelastic coefficient adjusters, compliant transducer mount and counter-weight for transducer mount	37
2-13	Location of anisoelastic coefficient adjusters	39
2-14	Outer rotor of RGG-2	44
2-15	Rotor asembly of RGG-2 with initial alignment pins in place and with lid removed	44
2-16	Inner rotor assembly being lowered into outer rotor	45
2-17	Skew axis alignment fixture	46
2-18	Sensing arm coordinates for mass properties	48

FIGURE		PAGE
2-19	Sectional view of RGG-2	49
2-20	Spin bearing assemblies, Mod C	50
2-21	Moc C bearing stator disassembled	52
2-22	Oil reservoir and bladder of Mod C bearing	53
2-23	RGG drag cups, one with speed control slotted disc	56
2-24	Upper stator half with spin motor and rotary transformer stators in place	57
2-25	Rotary transformers	58
2-26	Coupling capacitor for DTG	59
2-27	Stator of RGG-2	61
2-28	PE/LED rotor speed sensor	62
2-29	The completed RGG-2	63
2-30	Flow bench used for cleaning and assembly	66
2-31	Rotor match-boring	69
2-32	Final assembly procedure RGG-2	80
2-33	Mod C bearing with evacuation and fill ports	82
2-34	Oil degassing and bearing filling apparatus	83
2-35	Differential torque generator (DTG) schematic	87
3-1	Rotating field compensation process	97
3-2	Equivalent process	97
3-3	Gradiometer sensor output for 50% ON-OFF duty cycle	100

FIGURE		PAGE
5-1	GGI electronics built for rotating gravity gradiometer serial No. 2	106
9-1	RGG-2 transient response plot to a 35 kG mass at 0.3 m	125
9-2	Principal gradient noise and trend (spin axis vertical)	127
9-3	Cross gradient noise and trend plot (spin axis vertical)	128
9-4	RGG No. 2 transient response to moving mass plot (spin axis horizontal)	130
9-5	RGG-principal gradient noise and trend plot (spin axis horizontal)	131
9-6	RGG No. 2 cross gradient noise and trend plot (spin axis horizontal)	132

Rotating Gravity Gradiometer

SECTION 1

SUMMARY AND ACCOMPLISHMENTS

A. INTRODUCTION

This report documents the progress made during this 18-month, $958,880 contract to continue the development of the Hughes Rotating Gravity Gradiometer (RGG). Because the scope of work included both the development of the RGG and studies of platform requirements, this Final Report is written in two volumes to better distinguish between these two major tasks. Volume I addresses the tasks associated with the sensor development and Volume II, written under subcontract by Incosym, Inc., presents the findings and preliminary specifications for an inertial platform to support the RGG in an airborne environment.

The performance goals for the RGG remain identical to the original AFGL/DMA/DARPA statements made for the two prior AFGL contracts. Specifically, Hughes has been directed toward achieving gravity gradiometer performance in an airborne environment such as that provided by a C-135/C-141 aircraft flying in benign weather conditions. The gradiometer system performance goal is to determine the components of the gravity gradient tensor to an accuracy such that the individual RGG contributes no more than one (1) Eotvos Unit (EU) of noise when measured with an equivalent 10-second integration time. Three RGG sensors are required to measure all the components of the tensor. The sensitive axes of these three RGG sensors must be precisely aligned with respect to each other and with respect to the earth's gravity field, and isolated from angular and translational disturbances. Thus, a requirement exists for a Vibration Isolation Alignment and Leveling System (VIALS).

When the RGG triad is mounted on a VIALS, at least two of the RGGs must be oriented with their sensitive axes tilted in the g-field. Hence, the requirement that a gradiometer be capable of operating in any orientation. For this reason, this Report will separate performance results for the RGG fixed in the two extreme positions: spin axis vertical (SAV) and spin axis horizontal (SAH).

PRECEDING PAGE BLANK-NOT FILMED

It is important to recognize that all Hughes RGG performance data are stated in terms of 10-sec data sampling intervals and a total integration time equal to 10.1 sec. Also, all Hughes RGG gravity gradient test results are recorded in terms of the EU magnitude at the tensor element.

The 10-sec integration time is relatively short compared to requirements for other gradiometer missions such as those involving surface vehicles. The reader is cautioned as to the difficulties of interpretation if 10-sec data is to be compared with data taken for a different integration time. However, random noise figures are easily compared using a square-root time ratio. Thus, the equivalent of one EU of thermal noise at 10 sec is 0.4 EU at 1 min, or to 0.2 EU at 4 min, etc. Ten seconds is one of the stringent requirements that is made necessary by the operating parameters of the airborne mission. As stated in earlier Hughes reports, the airborne environment is still considered to be the most difficult. It is encouraging to note that the results of this contract continue to indicate that the airborne mission is feasible, practical, and achievable.

B. RGG SENSOR DEVELOPMENT OVERVIEW

Two RGG sensors were involved in the conduct of this 18-month effort. The first Hughes gradiometer, designed and built under the prior AFGL/DMA/DARPA contracts, is referred to as "RGG-1," Rotating Gravity Gradiometer serial No. 1. The second sensor, designed and built during the course of this contract, is designated "RGG-2." A third sensor will be referred to as "RGG-1S." This gradiometer is really nothing more than the RGG-1 modified such that the stator and rotors contain the pivot-arm (sensing) structure which was built as a spare component under the prior contract. Thus, during the course of this contract RGG-1 has evolved into RGG-1S, and only two Hughes gradiometers currently exist: RGG-1S and RGG-2.

At the start of this contract RGG-1 was not operational due to lubrication problems with the original hydrodynamic oil-lubricated journal bearings (Mod A spin bearings). Procurement of a set of modified bearings was initiated under Contract F19628-75-C-0201; under this contract the new bearings ("Mod B") were installed and tested in RGG-1. The test results were very encouraging in terms of both the spin bearing performance and the operation of the RGG sensor. Thus, September 1975 was the milestone date when the basic RGG-1 sensor, in the ungroomed state, was first demonstrated in the vertical and horizontal spin axis orientations (SAV and SAH). The specific performance results are shown in Table 1-1.

The terminology "grooming," used throughout this report, is meant to describe those adjustments and modifications made to the operational RGG sensor which improve on the as-manufactured condition of the sensor. The purpose of grooming is to minimize the RGGs responsiveness to environmental disturbances.

Typically, grooming is an iterative operation which starts with measuring the RGG output phase and magnitude while the RGG is being subjected to translational or rotational vibrations. The RGG outputs can be converted to estimates of specific error coefficients, which can then be stated in adjustment nomenclature (e.g., turns of a balance screw). The RGG is partially disassembled so that the trimming operations can be made. After reassembly, the process is repeated. Error coefficients are masured both for the rotating and nonrotating conditions and for many SAV and SAH orientations. This process is described in a contract report entitled "RGG R&D Design Evaluation Report," dated March 1976, and in Appendix C of this report.

Significant progress has been made during the past 18 months in the art of grooming the RGG. At the outset, studies of the vibration test equipment, known as the "laboratory VIALS," were required prior to making needed equipment modifications to eliminate unwanted structural resonances and motion cross-couplings. This was accomplished successfully. A significant grooming achievement concerned the use of the nonrotating vibration tests. First, a test technique was

Table 1-1. Hughes RGG Performance History

		Magnitude(EU)				
		SAV			SAH	
		Output	σ		Output	σ
RGG-1						
1975	March[a]	12,500	300		150,000	400
	June[a]	8,000	50		120,000	300
	Sept	4,000	10		120,000	100
1976	Jan	3,200	5		120,000	25
	April	—	2		120,000	25
	Aug	—	—		178,000	—
	Nov	—	—		30,500	—
			(5 hours)	Drift EU/day		(5 hours)
RGG-2						
1977	Jan	46	1.2	1.5	35,500	15

[a]Prior AFGL Contract

T2137

developed which obviated the need to disassemble the RGG; this not only accelerated the task of grooming but resulted in more accurate test results. Second, it was then shown that the estimates made in the nonspinning and spinning modes could be correlated. This fact further accelerated the grooming process. It is this type of progress, plus the increased understanding and familiarity with the techniques that has made the grooming process relatively straightforward.

The progress made with the spin bearings has been demonstrably successful. The Mod B bearings were tested soon after the start of this contract and proved effective when installed on RGG-1. Several design changes were made, however, before the "Mod C" bearings were fabricated for RGG-2. The changes resulted from an intensive review of the Mod B design and the early test results by Hughes, Shaker, and Incosym personnel. Two pairs of Mod C bearings were fabricated, thus, a spare set is readily available in case of need in either RGG-1S or RGG-2. To date, the second (spare) set has not been used. This fact particularly demonstrates that the Mod B bearings have operated in RGG-1S for the past 16 months without failure, and operated sufficiently well that it has not yet been necessary to replace them, and that no major problems have been encountered with Mod C bearings.

The early success with the Mod B bearings permitted achievement of the second major RGG-1 milestone in early January 1976: the decision to authorize unattended 24-hour, 7-day-per-week operation of RGG-1. This decision is a reflection of the confidence in both the RGG safety features and the lubrication retention capability of the Mod B bearings. The new mode of operation also had a very practical and beneficial effect in accelerating the grooming process. Continuous operation of the RGG sensor meant that test continuity could be maintained from day to day and throughout the weekends. As a result, knowledge of the RGG performance characteristics was gained at a very rapid rate from that date on.

One of the accomplishments made in February 1976, soon after authorization of continuous operation of RGG-1, was the discovery of

a previously unidentified magnetic sensitivity. Two closed loops had been unintentionally designed into the RGG-1 pivot-arm structure. One loop is formed by the two arm plates and the two proof masses. The fact that the loops are "closed" means that they have a very low dc resistance which permitted circulating eddy currents to be created when the loops were rotated in the earth's magnetic field. The problem was easily fixed by providing insulation to electrically "open" the loops. The first open-loop test, in August 1976, proved the effectiveness of this simple solution (this fix was also incorporated in RGG-2). The August test results were ironic in that they proved that the magnetic effect had been canceling the RGG-1 output, rather than adding to it. This fact is shown in Table 1-1 by observing that the SAH output increased from 120,000 EU to 178,000 EU after incorporation of the fix.

Also in February 1976, the RGG-1 g-squared sensitivity, i.e., the large output magnitude (120,000 EU) in the SAH orientation, was recognized to be a significant problem. It was originally intended that the anisoelastic properties of the arm plates would be trimmed by altering the dimensions of the slots in the arm plates. However, before any such attempts were made, a test was made of sample arm plate deflections under static loads. This test soon revealed the difficulty and undesirability of the slot trimming method. It was then decided that the arm plates of RGG-2 should be made without slots, and that the anisoelastic properties could be adjusted with devices attached to the arm plates. These devices are called "ACAs," anisoelastic coefficent adjusters. Although it was impossible to convert the slotted RGG-1 arm plates to the unslotted condition, a test of the ACA concept was made. The test results is reported in Table 1-1 where it is shown that the RGG-1S output was reduced from 178,000 EU to 30,500 EU. The ACAs used for this demonstration were incorrectly sized; had they been correctly sized, the SAH output would have been reduced to less than 10,000 EU. Then, by trimming the ACAs, the SAH output could have been further reduced. Unfortunately time did not remain to either resize or trim;

in fact, all RGG-1 testing was terminated in November 1976 in favor of assembling the new RGG-2 sensor. Nevertheless, the effectiveness of the ACA concept was demonstrated successfully in the November 1976 test.

As stated above and described in Section 2, RGG-2 was built with unslotted arm plates. During assembly, very small (less than 200 EU/g^2 ACAs were installed on the RGG-2 arm plates. The intent was to have the small ACAs for balance, yet be able to observe the RGG-2 g-squared sensitivity properties essentially in the nonadjusted condition. As seen in Table 1-1, the RGG-2 as-manufactured SAH output magnitude is almost as low as the RGG-1S output magnitude (with the "first'cut" ACAs installed). Thus, we can say that the g-squared sensitivity of the nonadjusted RGG-2 is improved over RGG-1S by a factor of approximately five (178,000 versus 35,500). Time did not remain on this contract to demonstrate the effectiveness of the ACAs on RGG-2, thereby proving that the SAH output can be reduced to the goal values.

In February 1976, the RGG-1 SAH performance was recognized to be a serious g-squared sensitivity problem. From that date on, priority was given to studies and experiments to develop a better understanding of the basic error mechanism. These activities led to the development of the compliant transducer amount (discussed in Section 2), the ACA concept, and replacement of the RGG-1 pivot-arm sensing assembly with an identical pivot-arm assembly (originally manufactured as a spare component). Although these and other activities were helpful in exonerating many components such as the spin bearings, transducers and mounts, electronics, spin speed, and a possibly-damaged pivot-arm assembly, etc., the exact source mechanism for the sensitivity problem remains to be identified. Despite this fact, the effectiveness of the ACA demonstration in November 1976 and the improved SAH performance demonstrated by the nonadjusted RGG-2, provide a high degree of confidence that ACA-adjusted RGG-2 SAH performance will match the excellent January 1977 SAV performance results (see Table 1-1).

The RGG-2 performance data in Table 1-1 is very limited because only one month remained for testing after the sensor was fabricated; all laboratory test work on this contract had to be completed by 1 February 1977. The detailed test results are reported in Section 9 of this report. They are highly encouraging. As pointed out throughout this report, development tasks remain. However, the accomplishments under this contract have been significant. The January 1977 demonstrations prove that RGG-2 instrument is superior to its RGG-1 predecessor, and that the performance goals are within reach.

SECTION 2

RGG-2 DESIGN FEATURES

A. MECHANICAL CONFIGURATION

The mechanical configuration of the RGG-2 is described in the following pages, along with the design rationale that led to the choice of that configuration. The RGG-2 was based strongly on the design of the RGG-1, with changes made only as deemed necessary to provide needed improvements. It should not be necessary to refer to previous RGG-1 documents in order to understand the description of RGG-2.

1. Sensing Structure

The heart of an RGG is the sensing structure. The masses, arms, pivots, and flanges of the sensing structure are seen in Figure 2-1. The flanges are tied together by the inner rotor shells shown in Figure 2-2. Figure 2-3 shows a complete sensing structure with all accessories added.

a. Pivot-Arms

The basic part of the sensing structure is the pivot-arm, seen in Figure 2-4 in two early stages of manufacture. The pivot arm consists of four arms, six pivots, two end flanges and one center flange, all machined in one piece from a specially-forged billet of alluminum alloy 6061-T6. Following rough machining to within 0.06 inch of final size, a heat stabilization was applied. This consisted of overaging at 425 F for 8 hours, then cycling 10 times from +212 F to -100 F. The pivot arm, as shown in Figure 2-4, was treated for stress relief at 375 F for 4 hours just before final machining.

The final sizing of the pivots was done by electrical discharge machining. During this machining process specially fitted spacers were attached between the arms to support the weight as the pivots became increasingly small and compliant. Following inspection, the

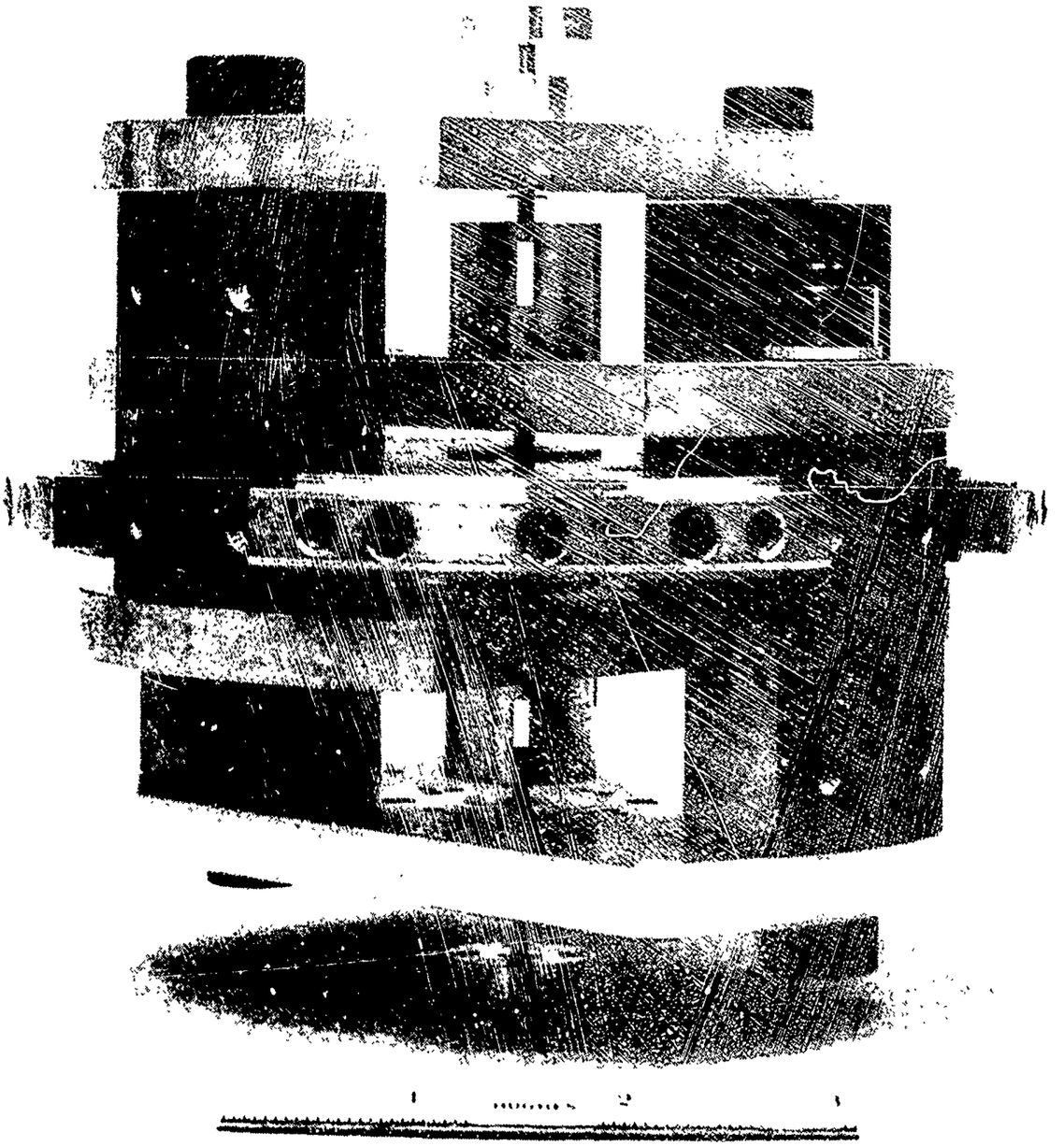

Figure 2-1. Pivot-arm and end mass assembly of RGG-2.

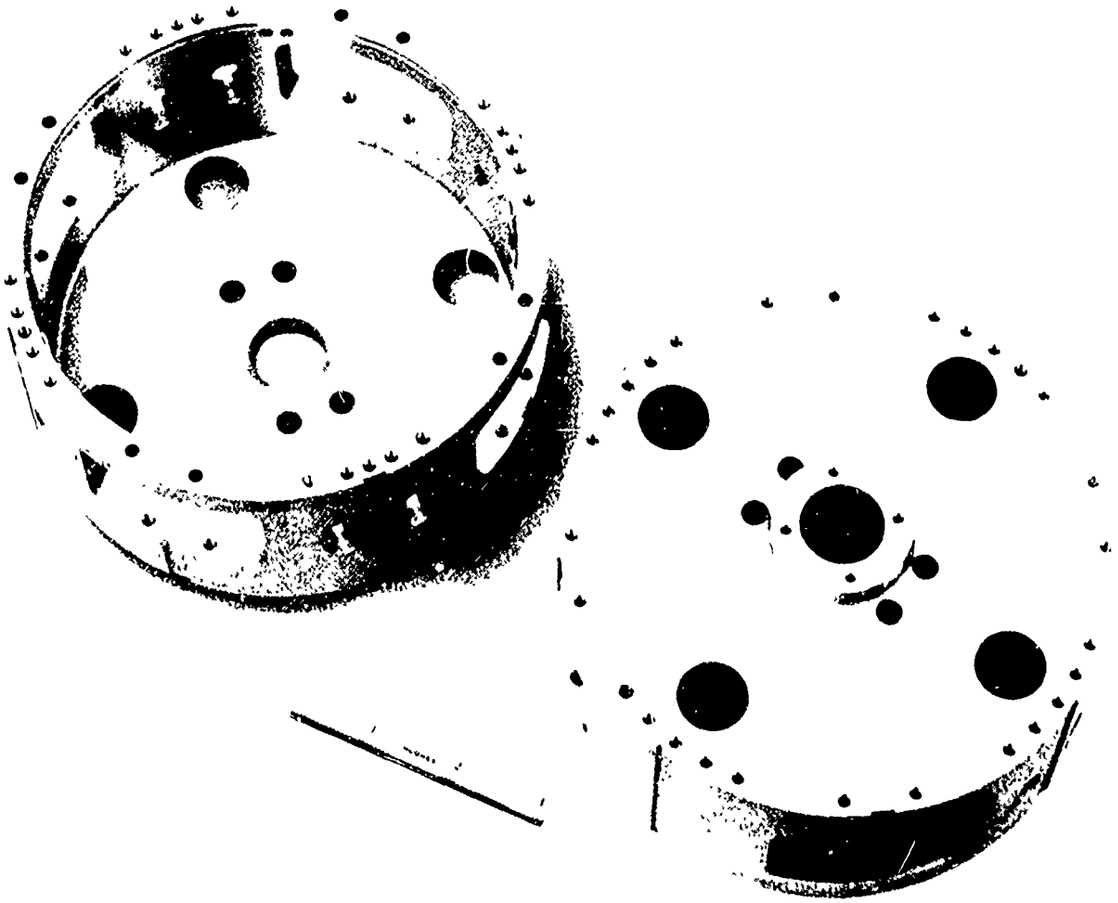

Figure 2-2. Inner rotor end bells of RGG-2.

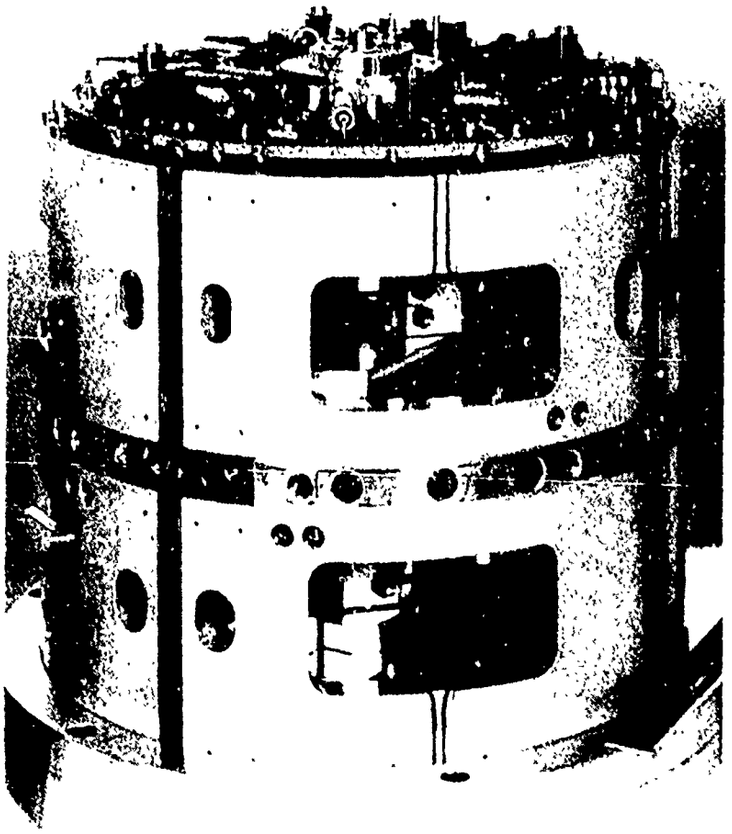

Figure 2-3. Sensing structure of RGG-2 (the inner rotor assembly).

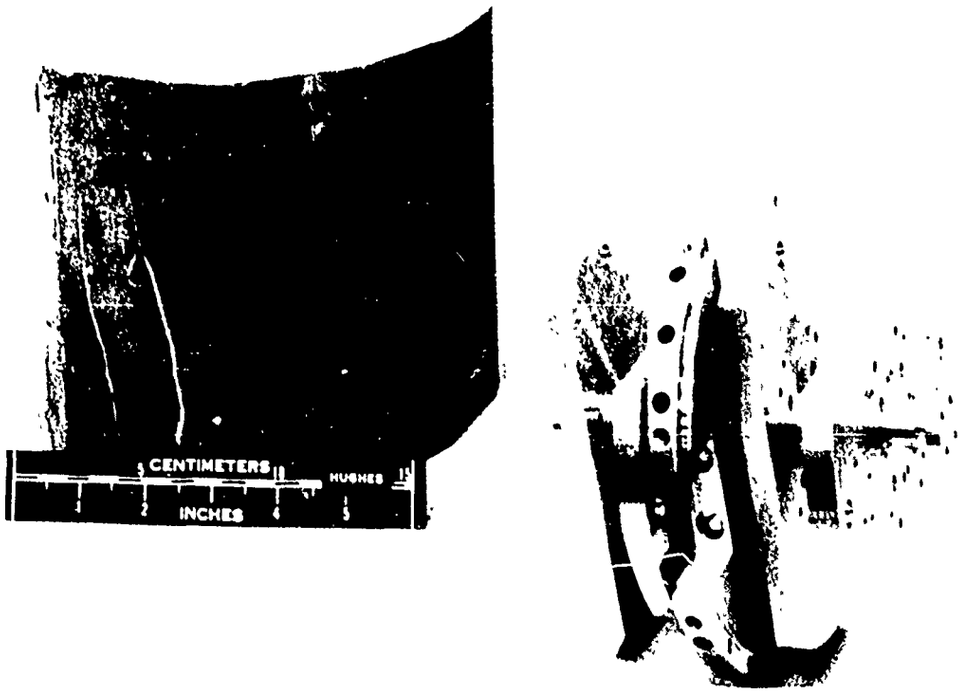

Figure 2-4. Special billet and nearly completed pivot-arm.

end masses were attached, thus adding rigidity; the assembly seen in Figure 2-1 was stored and transported in the special box shown in Figure 2-5.

Non-magnetic cutting tools were used for all finish cuts. All tolerances were held on this complex part, the largest tolerance being ±0.002 inch.

Rather than the single-bar type arm depicted in functional diagrams, each sensing arm is actually a pair of plates joined by pivots and bolted end masses to form a rigid box structure. The plates are interleaved to bring the centers of mass nearer to a common plane and to provide better support by the torsion pivots.

Two of the pivots are between the plates of the different arms. Two pivots support each arm by attachment through the flanges to the rotor structure. This arrangement supports each arm rigidly about all axes except for rotation about the common pivot axis. Having the flanges, pivots, and arm plates made from one piece avoids a difficult assembly process and promotes dimensional stability, as compared to an assembly built up from many parts.

b. End Masses

A high-density tungsten alloy, Mallory 1000, is used to fabricate the end masses. Each of the four masses weighs 1 pound. The end masses of RGG-2 are one-piece compared to the two pieces used in RGG-1. The two-piece end masses were necessary for assembly of RGG-1, as can be seen by comparing Figures 2-1 and 2-6. The one-piece end mass provides improved dimensional stability and permits a symmetrical, dynamically-balanced arrangement of coarse-balance screws.

The balance screws for the sensing arms are located in the end masses. There are four fine-balance screws and eight coarse-balance screws in each end mass. The balance screws are made of Mallory 1000 and have rolled threads to avoid a fit problem experienced on RGG-1.

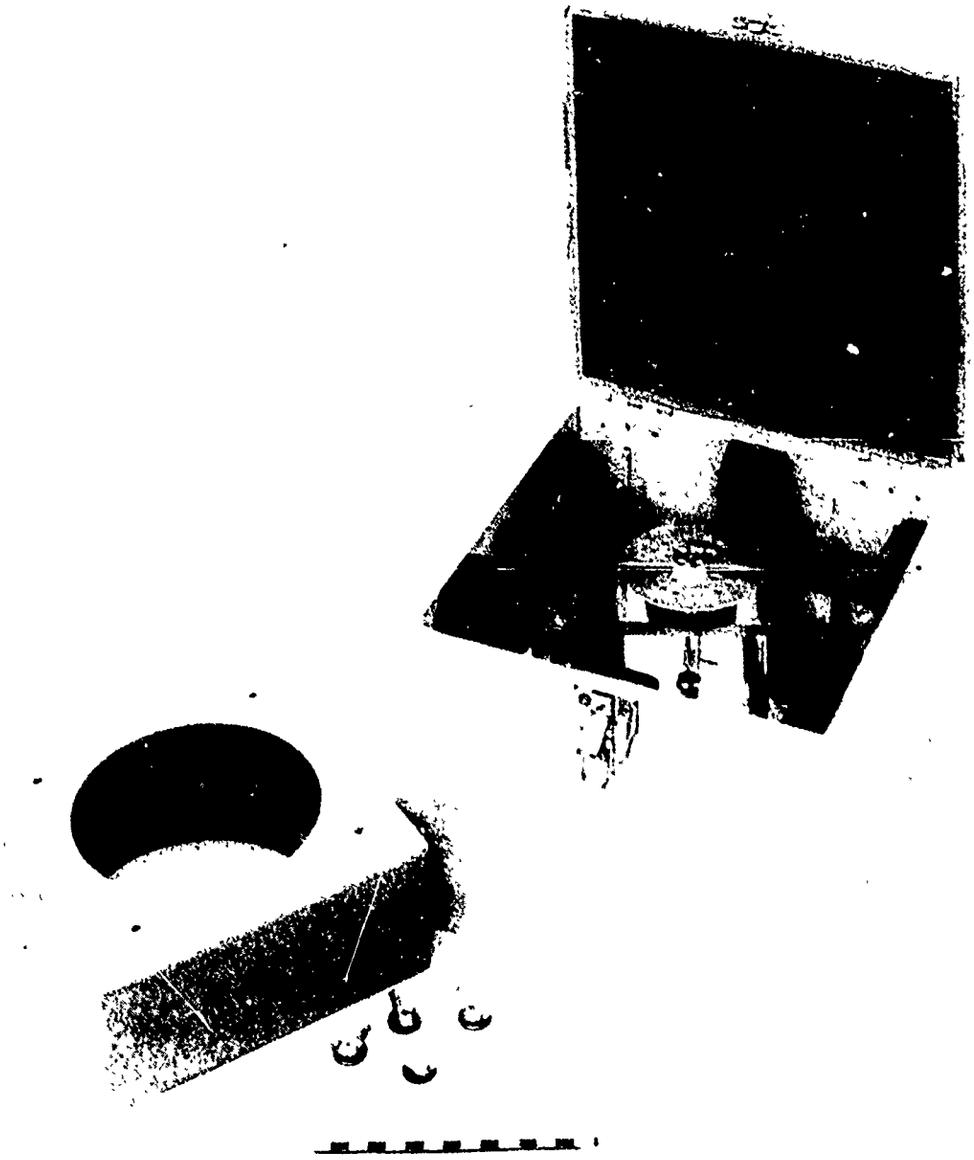

Figure 2-5. Box for transporting pivot-arm.

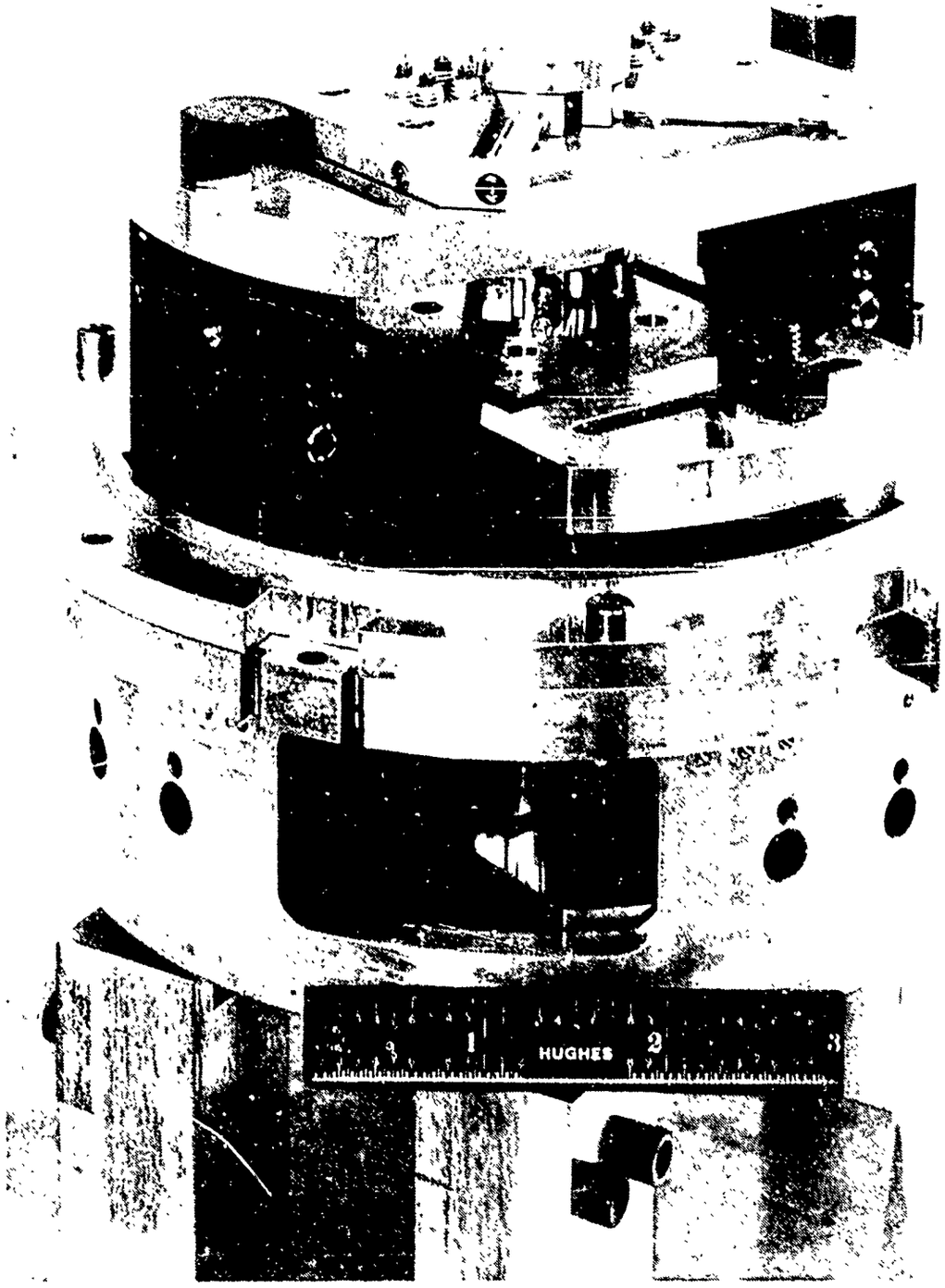

Figure 2-[illegible] Sensing structure [illegible]

The RGG-1 utilized Vibra-tite as a thread lock for the balance screws. This material became hard on long-term exposure to vacuum, making it difficult to adjust the screws. The balance screws of RGG-2 are locked into the end masses with nylon rods inserted through cross holes in the screws at mid-length. Screwing the balance screw into the tapped hole in the end mass causes the nylon rod to shear off flush with the thread at both ends; thus it provides a tight-fitting lock with constant torque. The debris from the shearing is readily cleaned away.

A beryllium copper bolt 0.3125 in. in diameter holds each end mass. Aluminum bushings are pressed into each end of each end mass to control the temperature coefficient of the assembly such that the 1700 pound preload on each bolt stays constant.

c. Eddy Current Loops Opened

The box structure formed by each sensing arm will develop eddy currents when rotated in a magnetic field unless the conductive loop is broken. Paralene C insulation 0.0005-inch-thick is therefore applied to the shanks of the beryllium-copper bolts, and 0.005-inch-thick mica washers are used on both sides of each arm plate where the bolt goes through. This results in complete electrical isolation of the bolts and the end masses and significantly reduces the sensitivity of RGG-2 to magnetic fields. This improvement was retrofitted to RGG-1S as well as being used on RGG-2 as originally assembled.

d. Arm Compliance Minimized

The R&D Design Evaluation Report reports on testing intended to result in an isoelastic arm structure. This was to be accomplished by special slots in the arm plates. It was later decided to eliminate all slots in the arm plates for the following reasons:

- The anisoelastic coefficient adjuster (ACA) was developed, permitting adjustment of the effective arm compliances to be done much more readily than lengthening of the slots in the arm plates.

- The stiffer arm structure requires less compensation.

- The expected lower radial compliance would tend to compensate for other sources of g-squared-sensitive torques that have the same polarity as high radial compliance.

Figure 2-7 shows test results obtained with four configurations of arm plate. For the RGG-2 candidate configuration it can be seen that the arm plate passes through the isoelastic condition (compliance difference equals zero) with the slot edge distance somewhere between 0.68 and 0.87 inch. It would be expected that both the radial and bending compliances would be lower for the RGG-2 final configuration. Improved measurement techniques will apparently be required to obtain better accuracy of prediction of the anisoelastic torques.

Simplified calculations of the expected compliances gave values much lower than those measured. Two reasons for this are:

- The press fit between the test arm plates and the arbor is a factor in the measurements.

- Simplified beam theory is not adequate for analysis of the arm plates. Local deflections near the points of load application are a significant part of the total compliance.

Additional effort towards the understanding and control of anis - elastic torques is desirable. However, the ACA concept effectiveness has been successfully demonstrated and is discussed later in this Section.

e. Pivot Resizing

Loads on the transducers due to lateral deflections of the pivots should be as small as possible to avoid anisoelastic effects. This is discussed in the R&D Design Evaluation Report starting on page 75. The design improvements listed there were incorporated. One of these was to incorporate end effects into the pivot design calculations. The end effects given in texts were not well suited to the RGG pivot configuration, so tests were conducted for pivot sizes in the range expected for the RGG-2 and an expression for the end effects was fitted to the data. The test set-up is sketched in Figure 2-8 and the results are tabulated in Table 2-1 for the following expression:

6318-2

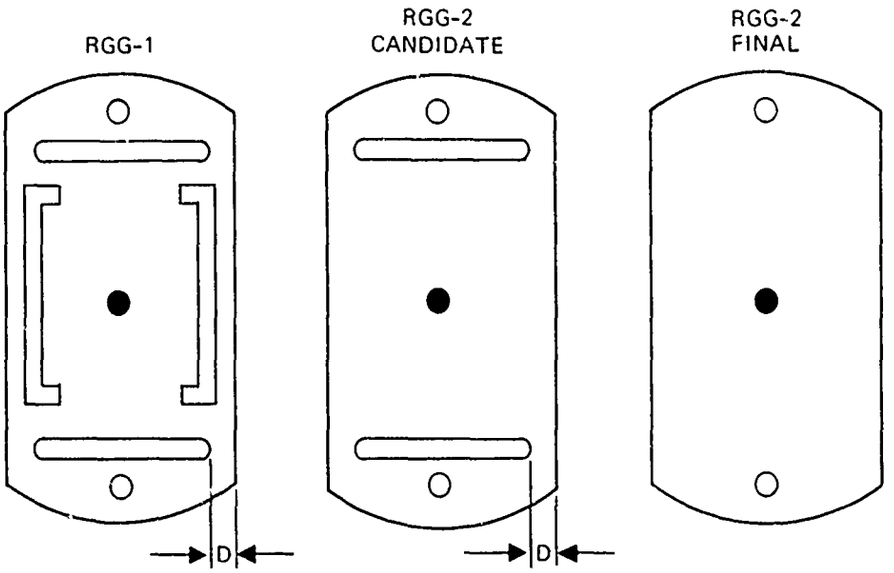

MEASURED COMPLIANCE		D = 0.87	D = 0.68		
RADIAL	2.83	0.52	0.95	0.88	10^{-6} IN/LB
BENDING	1.97	1.03	0.70	1.41	10^{-6} IN/LB
DIFF	+0.86	-0.52	+0.25	-0.53	10^{-6} IN/LB
ANISO COEF	+0.84	-0.55	+0.26	-0.56	10^{-5} EU/g^2
CONTROL	TRIM D	TRIM D		USE ADJUSTORS	

Figure 2-7. Arm compliance minimized.

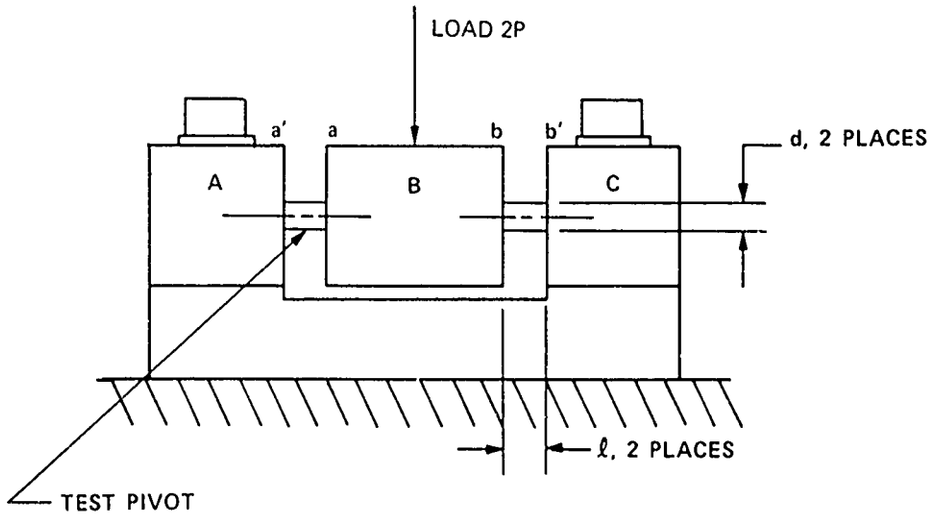

A, B, C AND PIVOTS ARE ONE PIECE OF ALUMINUM

DEFLECTION $y = \frac{(a+b) - (a'+b')}{2}$

Figure 2-8. Set-up for lateral deflection testing of pivots.

$$\text{lateral deflection } y = \left(\frac{PL^3}{12EI} - \frac{PL}{AG}\right)\left(1 + 0.1063\,\frac{d^{0.9}}{L^2}\right)$$

where

$\frac{PL^3}{12EI}$ = deflection due to bending

$\frac{PL}{AG}$ = deflection due to shear

$\left(1 + 0.1063\,\frac{d^{0.9}}{L^2}\right)$ - end effects, empirically derived

from which

$$K_L = \frac{P}{Y} = \frac{0.589Ed^2}{L\left(\frac{L^2}{d^2} + 2\right)\left(1 + 0.1063\,\frac{d^{0.9}}{L^2}\right)}$$

is the lateral spring constant (K_L) for pivots of the approximate sizes used in the RGG.

Estimates of the mass distribution of a sensing arm indicated that the 3.76 pound weight of an arm would be distributed 1.29 pounds on the outboard pivot and 2.47 pounds on the inboard pivot. The outboard pivots attach to the inner rotors and the inboard pivots attach to the center flange. See Figure 2-1. This factor determined the relative sizes of the inboard and outboard pivots.

Table 2-1. Pivot End Effects Data Versus Calculation

Pivot Size		Spring Constant K_L		Error in Calculation
Dia in.	Length in.	Measured lb/in.	Calculated lb/in.	%
0.1000	0.1275	70,000	69,896	-0.15
0.1250	0.1275	118,000	118,348	+0.29
0.1265	0.1640	96,944	96,714	-0.24
0.1375	0.1290	279,166	268,680	-3.76

12138

Another goal of the pivot resizing was to increase the sum mode frequency to remove it further from the one-omega rotation frequency while retaining the two-omega frequency near 35 Hz.

Thus, there were three requirements:

1. $K_1 + 4K_2 + K_3 + 2K_T = \omega_2^2 I$

2. $K_1 + K_3 = \omega_1^2 I$

3. $K_{1L} = 0.5238 K_{3L}$

where

$$K = \frac{GJ}{L\left(1 + 0.289 \frac{d^2}{L^2}\right)} = \text{torsional stiffness}$$

K_1 = torsional stiffness of outboard pivot

K_2 = torsional stiffness of differential pivot

K_3 = torsional stiffness of inboard pivot

K_T = torsional stiffness of transducers
= 92.6 in lb/rad

ω_2 = difference mode frequency
= 2π 35 rad/sec desired

ω_1 = sum mode frequency
= 2π 22.5 rad/sec desired

I = Moment of inertia of sensing arm
= 15.509 lb-in^2

K_{1L} = lateral stiffness of outboard pivot

K_{3L} = lateral stiffness of inboard pivot

$0.5238 = \frac{1.2933}{2.4690}$ = ratio of lateral loads on inboard and outboard pivots

Table 2-2. Pivot Sizes for RGG-2

	Outboard	Differential	Inboard
Length, inches	0.167	0.125	0.125
Diameter, inches	0.1069	0.1000	0.1225

T2139

Table 2-3. Natural Frequencies

	Diff(2ω), Hz	Spin(1ω), Hz	Sum, Hz	Transverse Hz
RGG-1	35.5	17.75	19	708
RGG-2 calculated	35.1	17.55	22.1	674
RGG-2 measured	34.667	17.334	22.045	---

T2140

The RGG-2 measurements were made on 8 December 1976 with the stator temperature control set at 110 F.

The vertical deflection of RGG-2 sensing arms with the spin axis horizontal is calculated to be 21.5 microinches. The differential pivots in this orientation should have deflections less than one microinch. It is believed that the pivot resizing contributed substantially to the reduced g^2-sensitivity of RGG-2 (discussed in a subsequent part of this section).

f. Inner Rotors Control Tension and Twist in Pivots

The initial twist in the pivots is thought to have an effect upon the axial acceleration sensitivity of the RGG, based on the results of tests with RGG-1. Therefore, RGG-2 incorporates features to permit a controlled twist to be added, and to permit control of the initial tension in the pivots and the alignment of their axes.

The inner rotor end bells seen in Figure 2-2 have diameters with precision fits to mating diameters on the end flanges and the center flange of the pivot arm. The end bells thus support the outboard pivots with respect to the center flange. The concentricities of the end bells and the pivot-arm are held to 0.0002-inch total runout so that the alignment of the pivot axes is rigidly maintained. While holding this axis alignment, however, the end bells can be rotated through small angles about the pivot axis with respect to the center flange. It is intended that at some future time the pivots will be twisted by rotating the end bells one milliradian in each direction from their initial setting, and the effects on the axial vibration sensitivity will be noted.

The inner rotor end bells were designed with flat tops to provide axial compliance. The outboard support pivots were placed in the plane of this flat top so that shear loads on the pivots would produce only radial loads, and not moments, in the end bells. This can be seen in Figure 2-9. Note that the outboard pivots attach to the end bells by means of stepped plates. The steps in these plates are matched with the measured compliances of the end bells to provide 10 pounds of preload in the outboard pivots.

Ten pounds was chosen as the initial preload because it will support the two 3.76-pound sensing arms at one gravity and all pivots will remain in tension. Also, 10 pounds causes a stress of only 1273 psi in the smallest pivot. The total stretch in all six pivots at this load is less than 100 microinches. Assembly of the end masses between the arms using the proper spacing, to be described in a later section, was expected to result in a fairly uniform 10-pound axial tension in the pivots when the pivot axis was placed in the horizontal orientation.

2. Rotor Assembly

The sensing structure described above must be supported for rotation, the output signal must be generated and transmitted, and other functions must be mechanized on the rotor assembly. A cross section of the rotor assembly is shown in Figure 2-9.

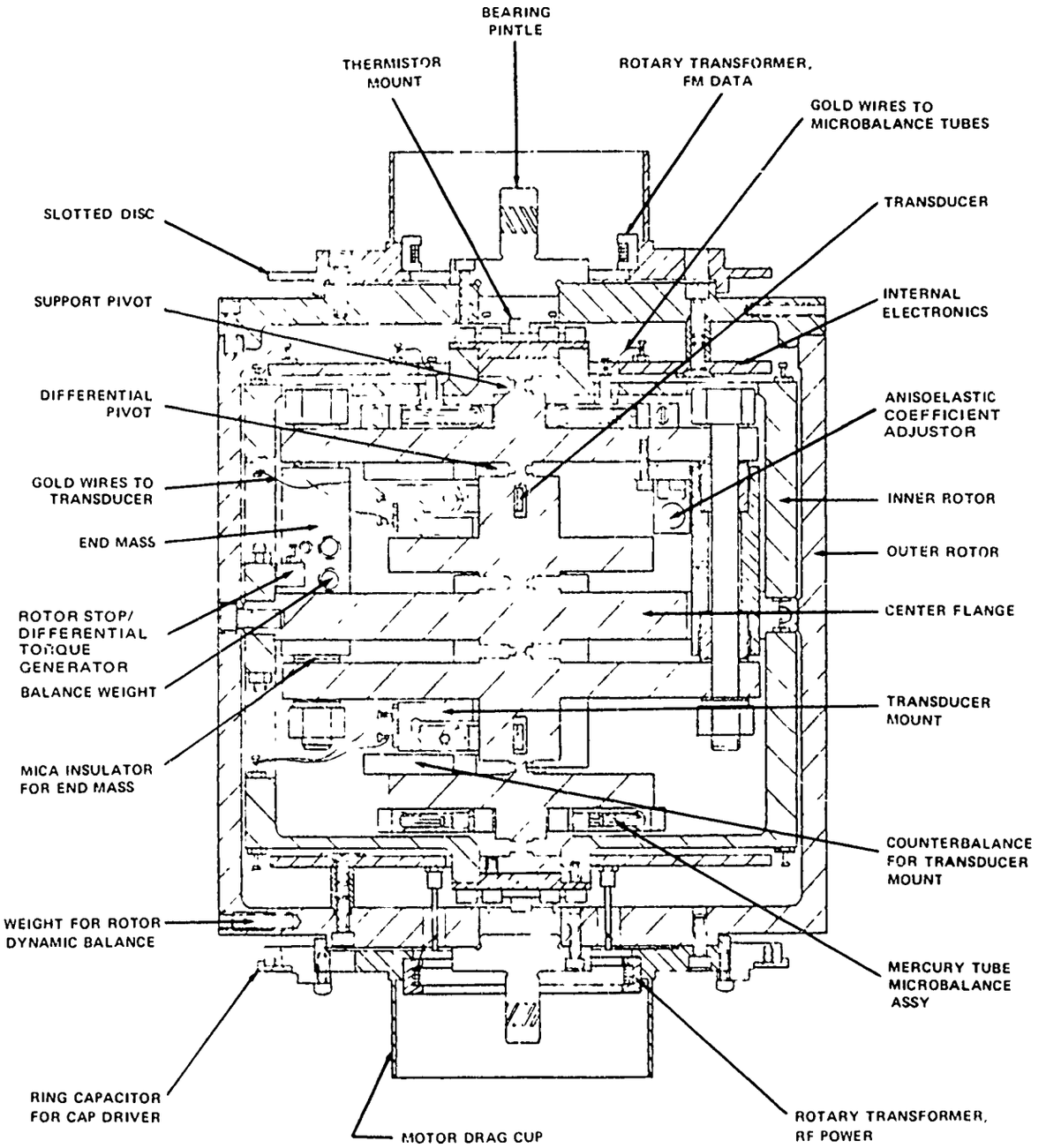

Figure 2-9. Cross section of RGG-2 rotor assembly.

a. Compliant Transducer Mounts

A pair of piezoelectric bender transducers are connected between the two sensing arms such that differential rotation between the sensing arms causes bending of the transducers. The transducers are isolated from most other forms of differential motion between the sensing arms by the so-called "compliant" transducer mounts pictured in Figure 2-10.

The central bar in Figure 2-10 is a stainless steel bar that substitutes for the relatively brittle barium titanate ceramic transducer while the transducer mounts are aligned and bolted down to the sensing arms. The mica insulators, clamping blocks, screws and nuts are also pictured.

The arrangement of the transducers between the sensing arms is sketched in Figure 2-11. Each transducer extends through the pivot axis by virtue of the rectangular holes placed in the central hubs (seen in Figure 2-1). Each transducer mount has a counterweight such as seen in Figure 2-12.

b. Differential Torque Generator

The small wedge-shaped parts seen in the foreground of Figure 2-10 act as mechanical stops for the end masses. They attach to the inside of the inner rotor and are set to permit each end mass to travel 0.005 inch (approximately 2 milliradians) in each direction from its rest position. A pair of such stops brackets each end mass. The stops avoid arm rotations or lateral deflections that might cause the pivots to yield. They offer great protection to the pivots when balance screws are being adjusted. They also protect the pivots against sudden rotor stops and other shocks.

The mechanical stops also serve a second very important function. They are insulated from the sensing structure and form the plates for electrostatic torquing of the sensing arm. They are connected electrically for either differential or sum mode torquing. In the future they could also be used as differential or sum mode capacitive

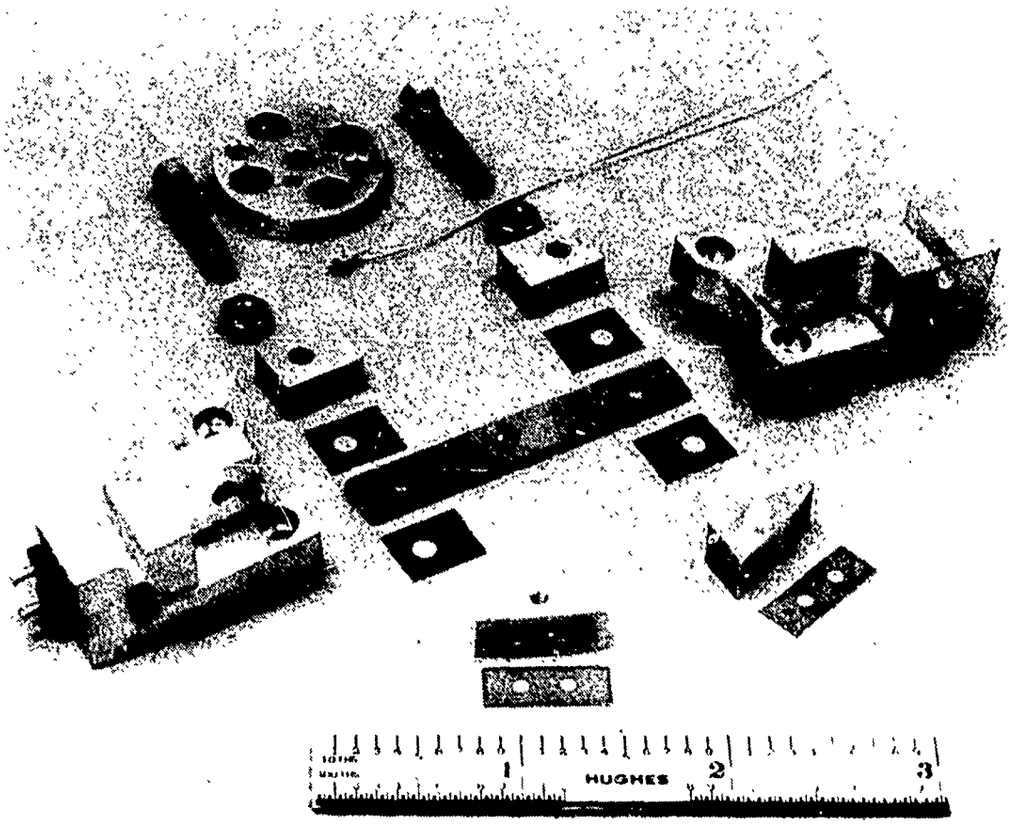

Figure 2-10. Transducer mounts, stops for end masses, and thermisto· mount.

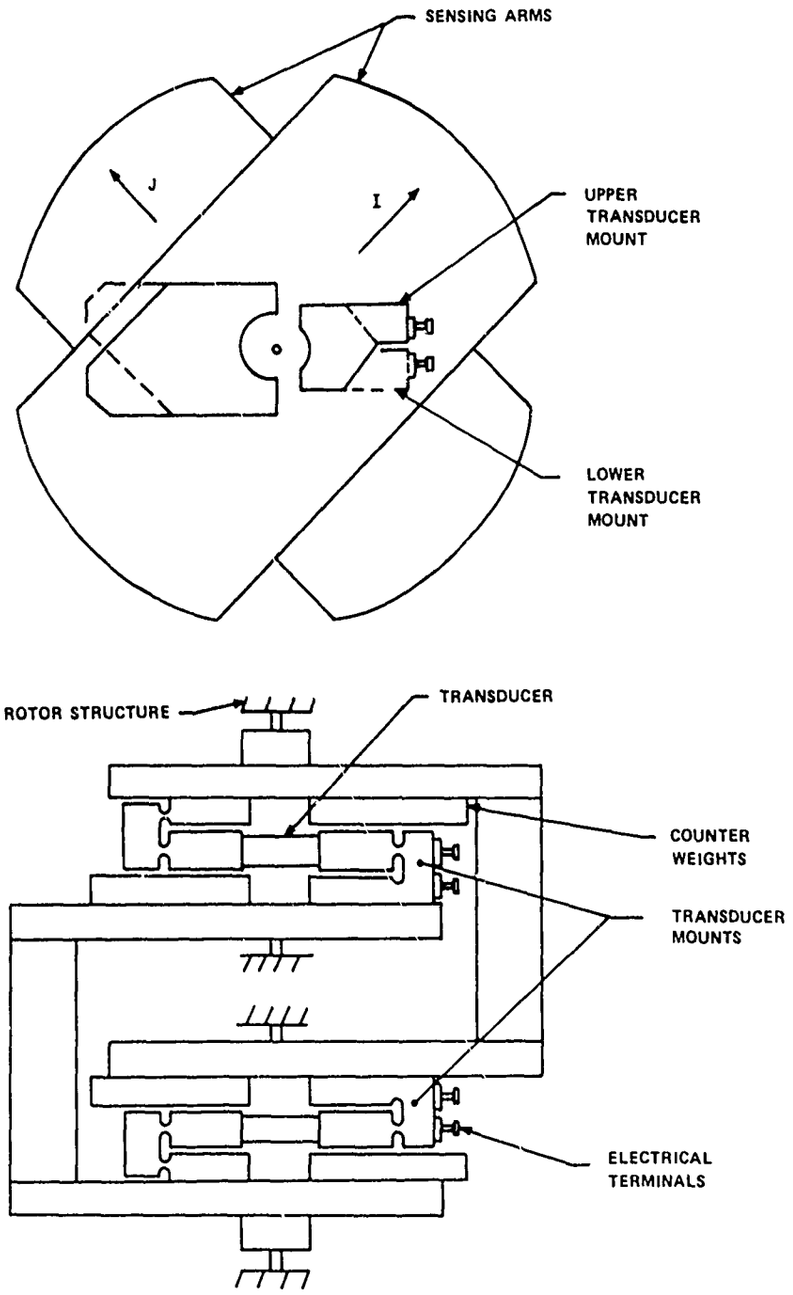

Figure 2-11. Arrangement of transducer mounts and counterweights.

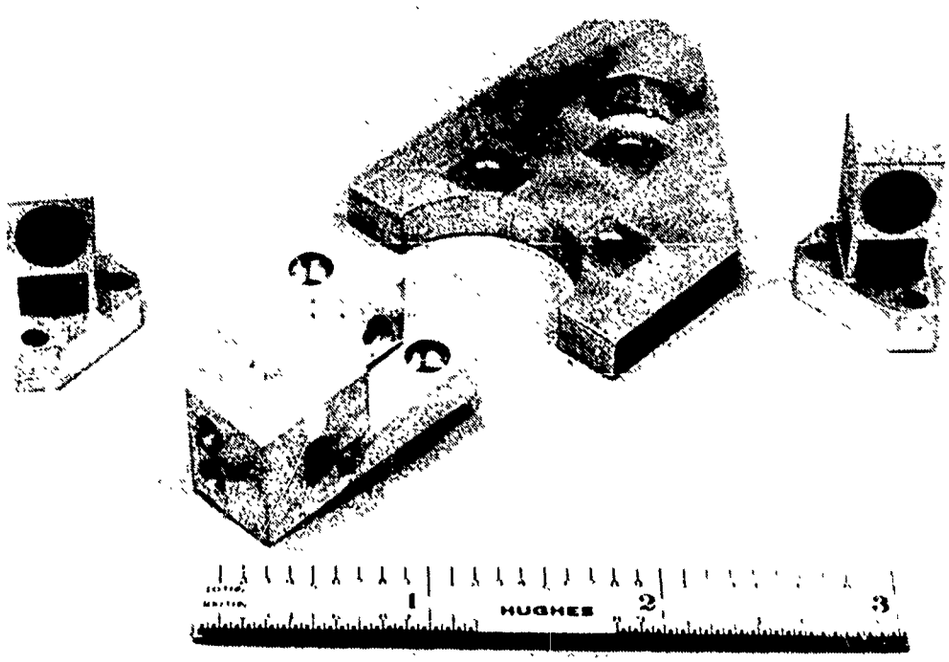

Figure 2-12. Anisoelastic coefficient adjusters, compliant transducer mount and counterweight for transducer mount.

pickoffs. Changing modes requires only the changing of four jumpers at the equatorial terminals seen in Figure 2-3. The stops are normally connected for use as a differential torque generator (DTG), a highly valuable feature of the RGG-2 that is discussed elsewhere in this report.

c. Anisoelastic Coefficient Adjustors

The as-manufactured g^2 sensitivity of RGG-2 is estimated to be approximately 33,000 EU/g^2. This compares very favorably with the 178,000 EU/g^2 estimated for RGG-1 before installation of the anisoelastic coefficient adjusters (ACA's). Thus, the basic design of RGG-2 achieved a 5:1 reduction of this sensitivity compared with the prior design. The 178,000 EU/g^2 sensitivity was subsequently reduced to approximately 30,000 EU/g^2 with the addition of the ACA's. It is significant to note that only one attempt was made to size the ACA's in RGG-1S; time did not permit the trimming operations which would have further reduced the 30,000 EU/g^2 figure. The important fact is that the success of the RGG-2 design, coupled with the demonstrated success of the ACA concept, suggests that RGG-2 can be adjusted to demonstrate a residual g^2 sensitivity at or near the goal value.

The g^2 sensitivity adjustment will require modification of the anisoelastic coefficient adjusters seen at the right and the left in Figure 2-12. Machining of the arm plates is not required. Instead, the adjusters are removed and reworked or replaced. The mass can be trimmed or the compliance of the flexures altered. After adjustment, the adjusters are bolted back in place on the arm plates. Rebalancing of the sensing arms is then required.

The location of the adjusters on the sensing arms just inside the end masses is shown in Figure 2-13. There are four ACA's in an RGG, two on each sensing arm. The configuration presently installed in RGG-2 is depicted, with the flex such that the maximum compliance is radial. The base, the dual flex and the carrier for the mass are machined from one piece of aluminum. The majority of the mass comes from a cylinder of Mallory 1000 press-fitted and bonded into the carrier.

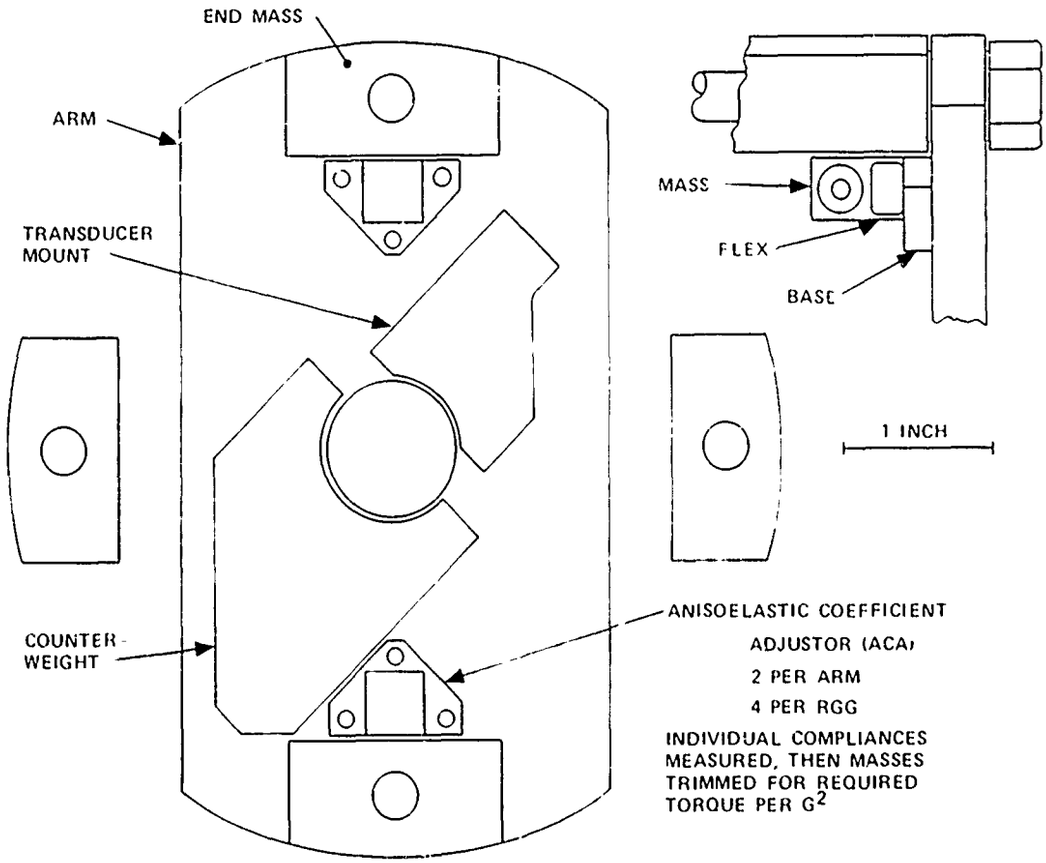

Figure 2-13. Location of anisoelastic coefficient adjusters.

Fine tuning of the adjusters is accomplished by measuring the mass and the compliance of the flex on each adjuster, then removing a controlled amount of mass to achieve the desired torque per acceleration-squared. The mass is removed by drilling a hole through the axis of the Mallory 1000 cylinder.

Table 2-4 shows some parameters of the adjusters. The existing ACA's in the RGG-2 are contributing slightly to the g^2-sensitivity instead of counteracting it. The ACA's to be installed later will have flexure axes oriented perpendicularly to the present ACA's, thereby giving the effect of softening the arm plates in bending. The flexes will be electrical discharge machined to a thickness of 0.0071 inch. The mass will initially be 10 grams to permit margin for tuning. The initial average mas of the RGG-1S adjusters was 16.57 grams. This was trimmed to 14.93 grams average after the compliances of the flexes were measured. Each adjuster was expected to generate 3.389 dyne cm/g^2.

The anisoelastic coefficient can be calculated using the following expression.

$$K = N \frac{m^2}{4} (K_r - K_b) g^2 / ((I_{yy} - I_{xx}) \times 10^{-9})$$

where

K = desired adjustment of anisoelastic coefficient EU/g^2

N = Number of adjusters = 4

m = mass of each adjuster, grams

K_r = radial compliance of flex, cm/dyne

K_b = bending compliance of flex, cm/dyne

g = 980.7 cm/sec^2

$I_{yy} - I_{xx}$ = 37,894 gm-cm^2

K = 32,400 EU/g^2 (based on initial test data)

It is expected that at least two ACA trimming iterations will be required to reduce the residual g^2-sensitivity of RGG-2 to a value that is compatible with the present state of the RGG development.

Table 2-4. Parameters of Anisoelastic Coefficient Adjusters

Use	Mass grams	Flex Thickness inch	Resonant Frequency Hz	Radial* Displacement inch	Anisoelastic** Coefficient EU/g^2
RGG-1S†	14.93	0.0165	231	0.00018	-165,000
RGG-2 present	10.0	0.0400	5289	0.000019	191
Example only	5.0	0.0135	1462	0.00024	2,500
Example only	10.0	0.0135	1034	0.00048	10,000
RGG-2 first adjust	9.0	0.0071	415	0.0030	-33,000
Maximum for RGG-2 size adjuster	10.0	0.0046	207	0.012	125,000

*The radial displacement listed occurs where an adjuster is used with its maximum compliance directed radially. For the RGG-1S and the RGG-2 adjustments the maximum compliances are perpendicular to the centrifugal force and the radial displacements will be less than 1% of those listed.

**The coefficient is based on the use of four adjusters.

†The RGG-1S adjuster design uses a larger mass and a longer, more narrow flex than RGG-2 in order to obtain the large adjustment needed.

T2141

d. Improved Heat Dissipation for Rotating Electronics

The rotating electronics circuit boards for RGG-2 were made in a flat configuration for ease of fabrication. They incorporate a copper cladding that collects the heat dissipated by the components and conducts it to the four mounting spacers. The cladding faces the inner rotor assembly so that the sensing structure is isolated from the hot spots caused by the components.

The beryllium copper mounting spacers for the electronic boards collect the heat from the cladding and carry it to the outer rotor. The only contacts between the electronic boards and the inner rotor assembly are small, flexible loops of wire that connect from the electronics to standoffs on the inner rotors. These may be seen in Figure 2-3.

The majority of the heat dissipated by the electronics (about 0.5 watt in the top board and 0.4 watt in the bottom board) is thus conducted directly through the ends of the outer rotor to the bearings. The bearings are the only significant heat energy conductors between the rotor and stator. This is in contrast to the RGG-1 configuration where the heat energy of the electronics must be conducted through the inner rotors to the center flange, then back through the separate outer rotor end bells and finally to the bearings.

A thermal simulation of the RGG-1 showed that the average temperature difference across each pivot for the electronics mounted to the inner rotor is 0.185 F. This value is reduced to 0.0044 F temperature difference in RGG-2 because the electronics are mounted to the outer rotor.

e. Windage Shield

The outer rotor of RGG-2 shields the sensing arms from air currents caused by shearing of the residual gases in the gap between the rotor and the stator. Appendix A describes the estimation of the windage torque and heat transfer at various low pressures. At 10 microns of mercury pressure (1×10^2 Torr) the windage torque is still 13% of that at atmospheric pressure.

The RGG-1S is sensitive to changes in the internal pressure because of openings in the outer wall of the rotor. The openings were eliminated in RGG-2 by the outer rotor design seen in Figure 2-14. A change of pressure in the RGG-2 from 9 microns to 200 microns caused a change in output magnitude of only 2 EU.

This low sensitivity demonstrates the effectiveness of the windage shield. The RGG-2 typically operates at less than 10 microns of mercury.

f. Alignment of Torsion and Spin Axes

The effective axis of the torsional pivots is defined by the inner rotor assembly seen in Figure 2-3. The spin axis is determined by the bearing pintles. The pintles are mounted on the ends of the outer rotor. The inner rotor assembly can be positioned within the outer rotor to obtain precise alignment of the pivot axis with the spin axis.

Figure 2-15 shows the inner rotor assembly in place in the outer rotor. It is held in alignment by special pins until the eight screws that secure the center flange to the outer rotor are fastened. Figure 2-16 shows the inner rotor assembly being lowered into the outer rotor.

The special pins seen in Figure 2-15 provide an estimated initial alignment of the spin and torsion axes to within 200 microradians. Misalignment of these axes creates a sensitivity to angular velocities of the stator at spin harmonic frequencies. It is desirable to reduce this "skew axis misalignment" to less than 10 microradians. This adjustment will require test data and a special test fixture as sketched in Figure 2-17.

The assembly of the inner rotor in the outer rotor plus the motor drag cups, rotary transformer rotors, capacitor plate for DTG, bearing pintles and dynamic balance screws completes the rotor assembly. This assembly has proven to have the accessibility for balance adjustment and the durability, rigidity and accuracy envisioned during its design.

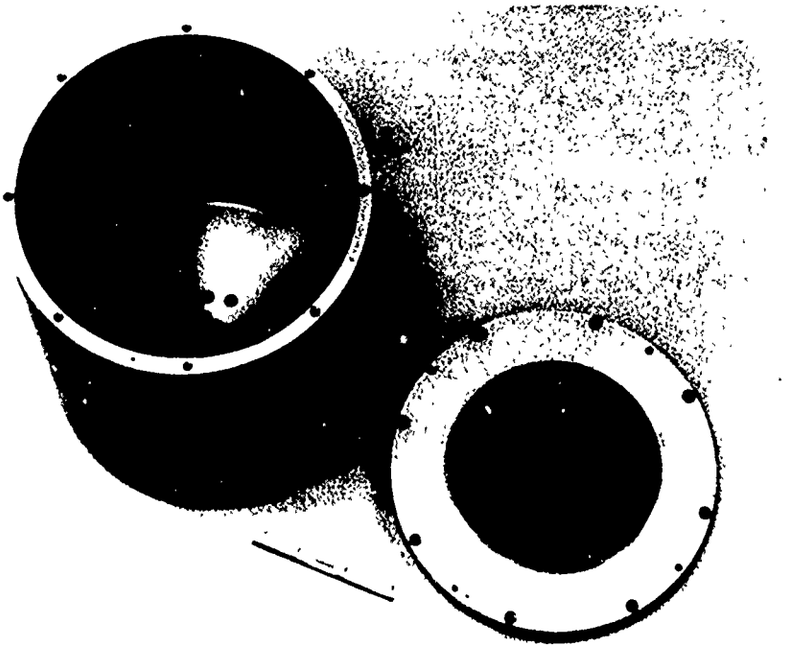

Figure 2-14. Outer rotor of RGG-2.

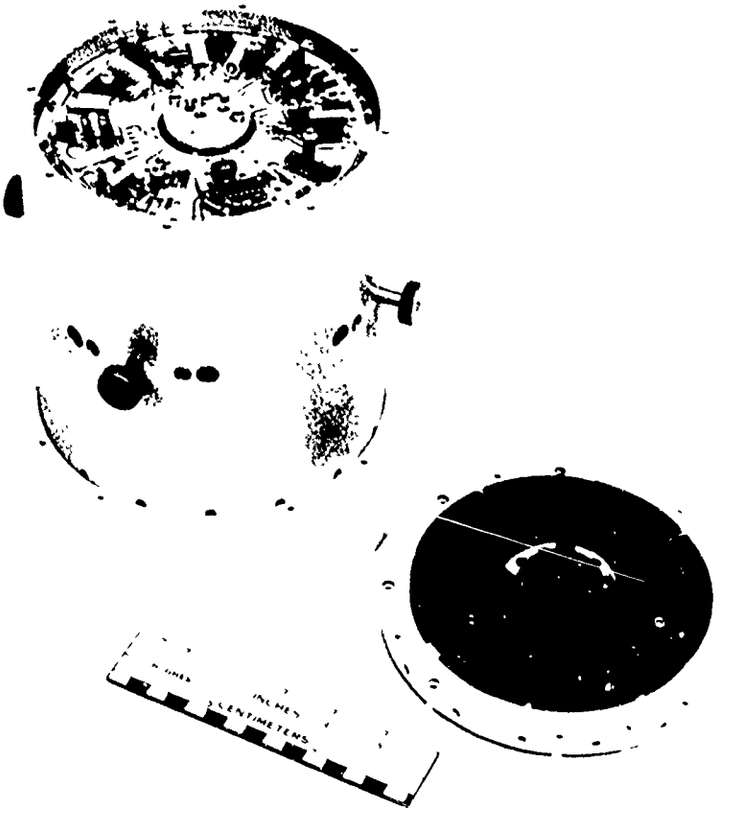

Figure 2-15. Rotor assembly of RGG-2 with initial alignment pins in place and with lid removed.

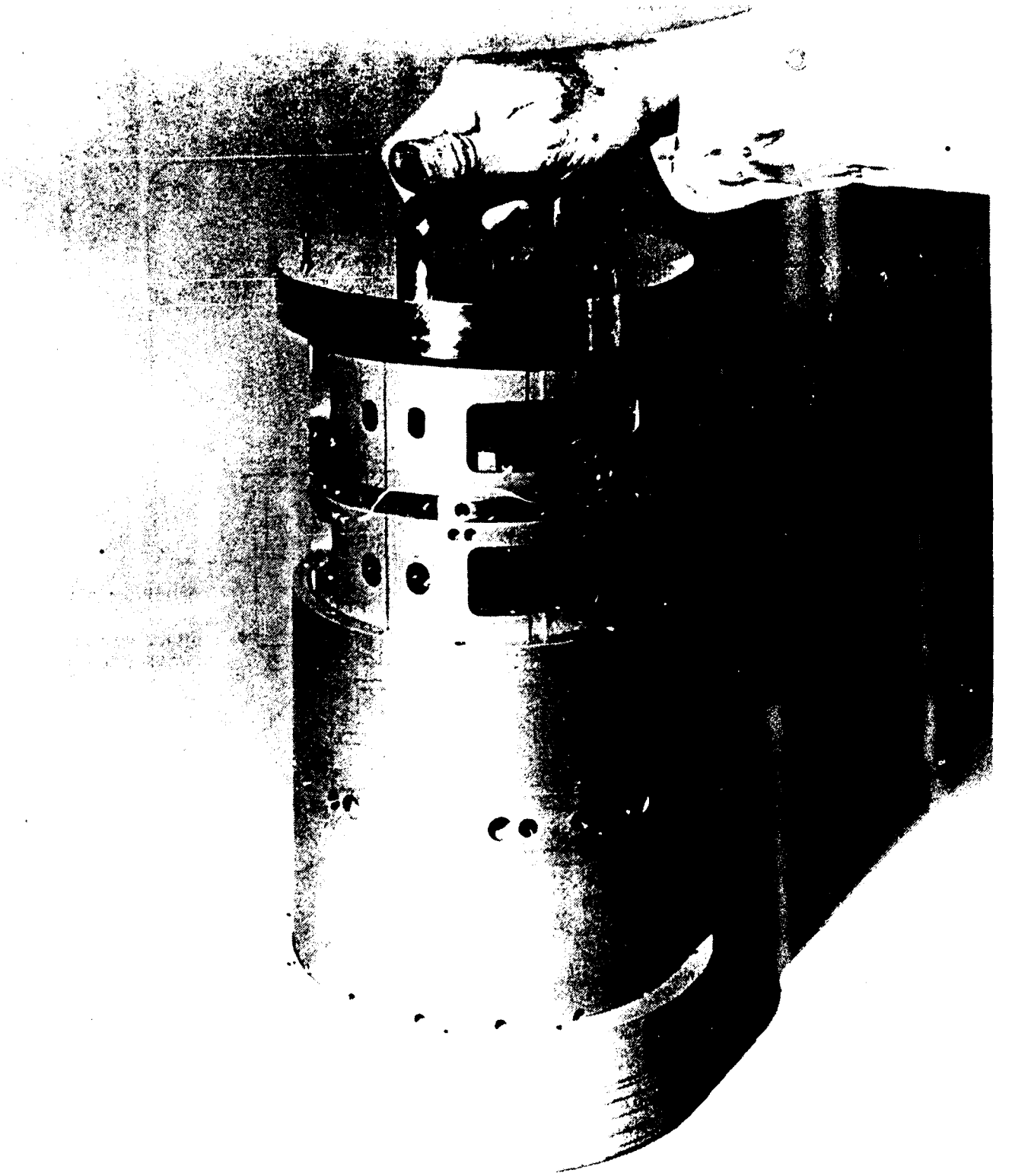

Figure 2-16. Inner rotor assembly being lowered into outer rotor.

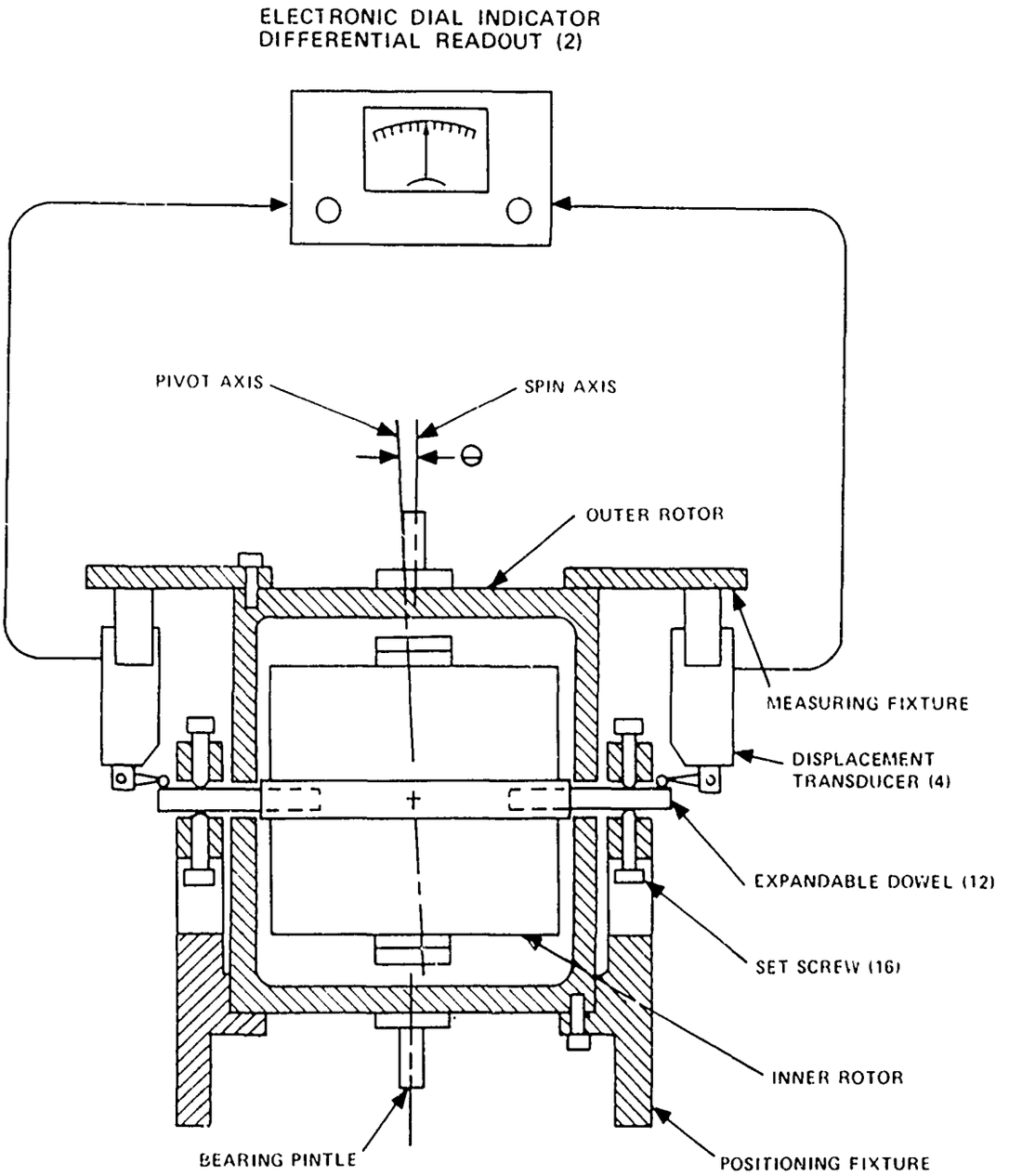

NOTES 1 (X) INDICATES QUANTITY

2 THE SET SCREWS OPERATE ON SEPARATE DOWELS FROM THE TRANSDUCERS

Figure 2-17. Skew axis alignment fixture.

g. Mass Properties

The mass of each rotor part was measured after fabrication and the estimates of mass properties were updated. The figures in Table 2-5 are accurate within one percent. Refer to Figure 2-18 for axes.

Table 2-5. Mass Properties of the RGG-2 Rotor

Description	Mass grams	Moment-of-Inertia gm-cm^2
Sensing Arms, per arm	1701	
about axis X		13, 129
about axis Y		51, 023
about axis Z		44, 694
Rotor Assembly, including arms	8312	
about axis Z		301, 356

T2142

3. RGG Assembly

The remainder of the RGG-2 design has few basic configuration changes compared to RGG-1 but there are many refinements. A cross section of the RGG-2 is given in Figure 2-19.

a. Mod C Bearings

The rotor of the RGG is suspended within the stator by oil-lubricated hydrodynamic bearings. The torque required by the bearings must be extremely constant to minimize the effect of variations on the RGG output. The bearings are made of aluminum with a thick layer of hard anodize. The hard anodize is ground to a finish better than 4 microinches rms on the bearing operating surfaces. Bearing operating clearances are 180 microinches nominal radially, and 100 microinches at each end, axially. Neoprene lip seals rubbing against the pintles prevent the oil from escaping. Figure 2-20 shows the assembled bearing stators and the pintles that attach to the rotors.

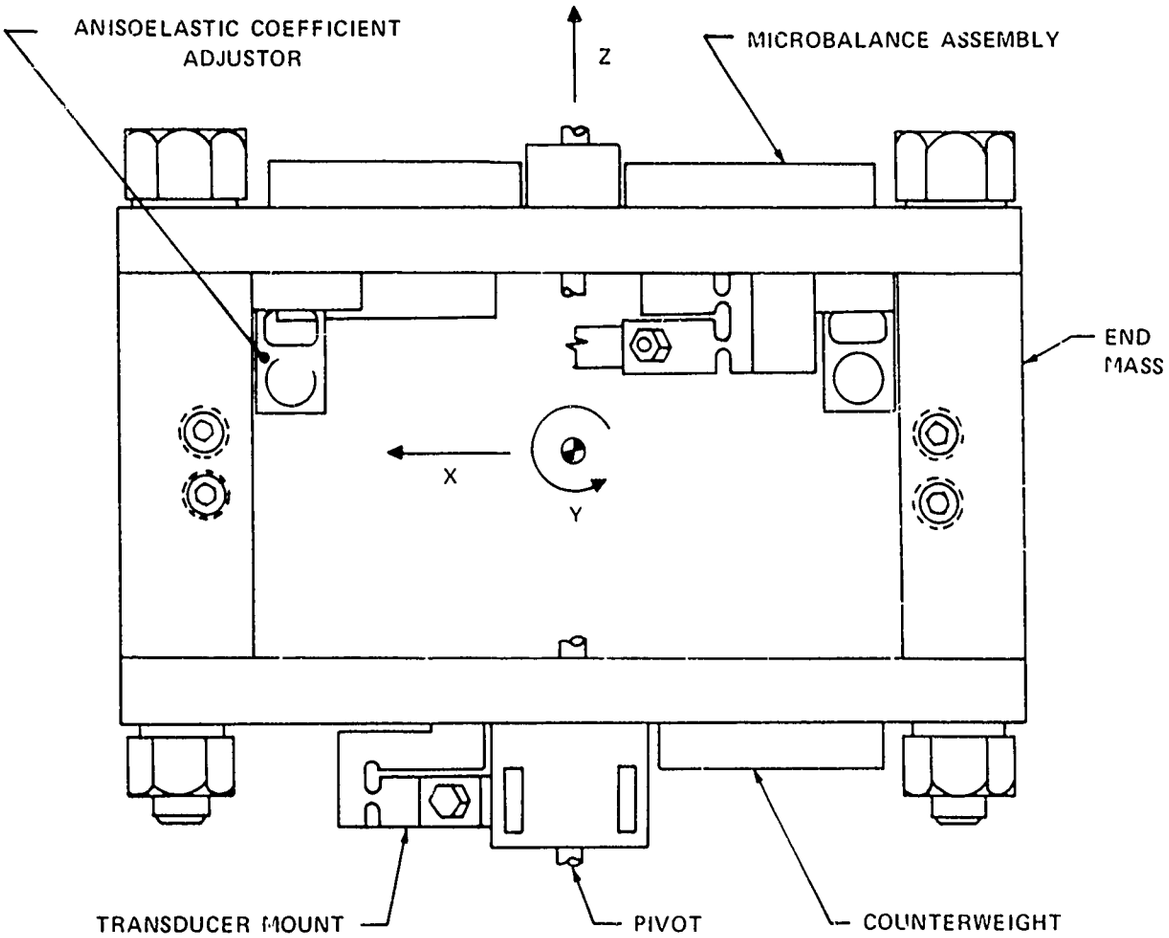

Figure 2-18. Sensing arm coordinates for mass properties.

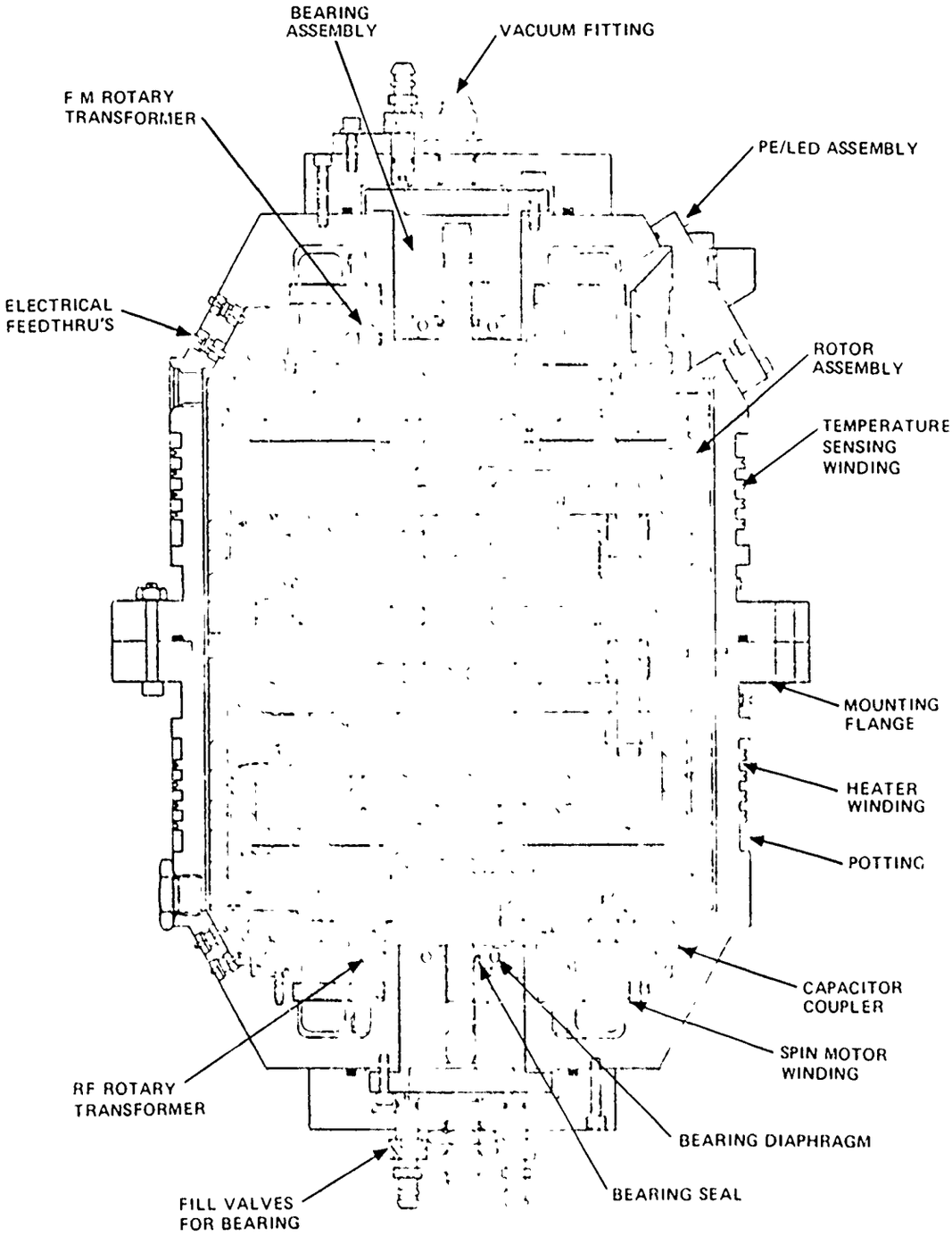

Figure 2-19. Sectional view of RGG-2.

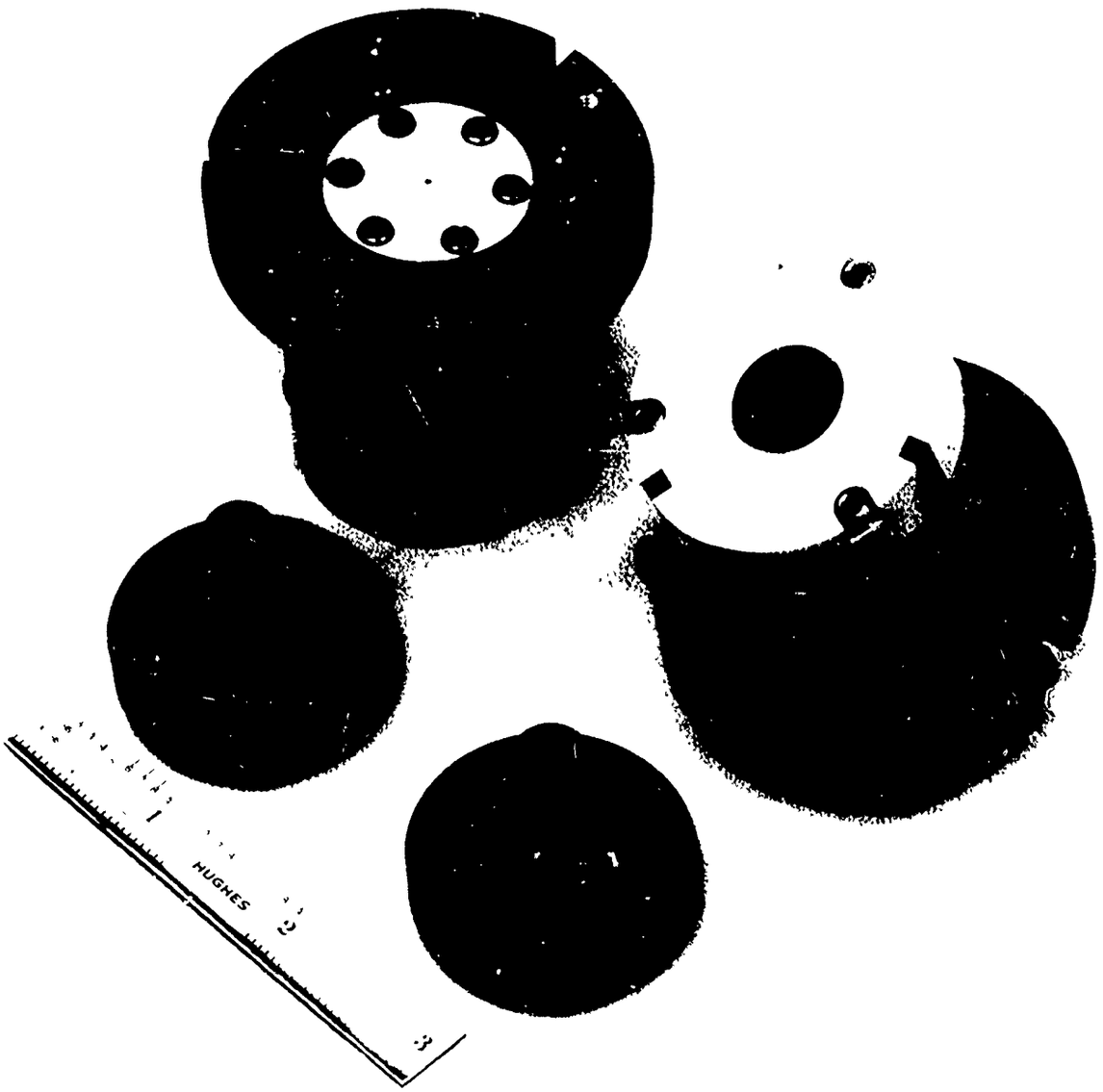

Figure 2-20. Spin bearing assemblies, Mod C.

The Mod B bearings that have given very reliable service on the RGG-1 have some drawbacks. Their means for recirculating oil is via a felt wick. The wick is a source of initial particulate contamination of the oil after the bearing has been disassembled. However, in a few hours of operation the wick appears to provide a self-filtering action. Each Mod B bearing has a vent to the inside of the RGG to permit operation in a vacuum. The oil must be introduced into the wick in careful stages, allowing the air in the oil to dissipate through the vent (called "degassing" of the oil). If the vacuum is established too rapidly, or the increment of oil added is too large, the oil foams and is carried off through the vent. After an adequate surplus of oil has been added and degassed to assure a re-circulating oil supply, it is necessary to keep the vent hole above the mid-point of the bearing. This limits the attitudes into which the RGG-1 can be placed.

The Mod C bearing was designed to operate in all attitudes by removing the wick and flooding the inside of the bearing with oil. In order to avoid a one-atmosphere pressure differential across the shaft seal, and to provide for temperature expansion of the oil, a soft diaphragm in the form of a tubular rubber bladder was placed in the oil reservoir to form the interface between the oil and the residual gases in the RGG. Figure 2-21 shows the relationship of parts in the Mod C bearing stators and Figure 2-22 shows the operation of the bladder. The inside of the bladder is vented to the inside of the RGG.

The Mod C bearing is filled with oil like a floated gyro, using a procedure to be described in a later section. The two valves that control degassing and oil flow can be seen at the top in Figure 2-20 and towards the right in Figure 2-21.

Summarizing the benefits of the Mod C bearing design, it retains these features of the Mod B:

- Successful geometry, clearances and grooving
- Performance
- Size - the bearings are interchangeable

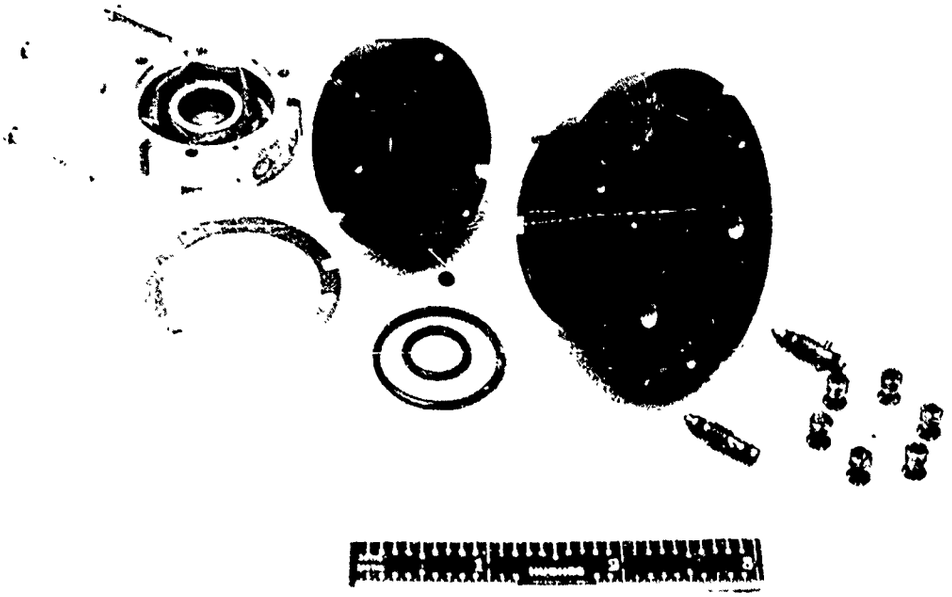

Figure 2-21. Mod C bearing stator disassembled.

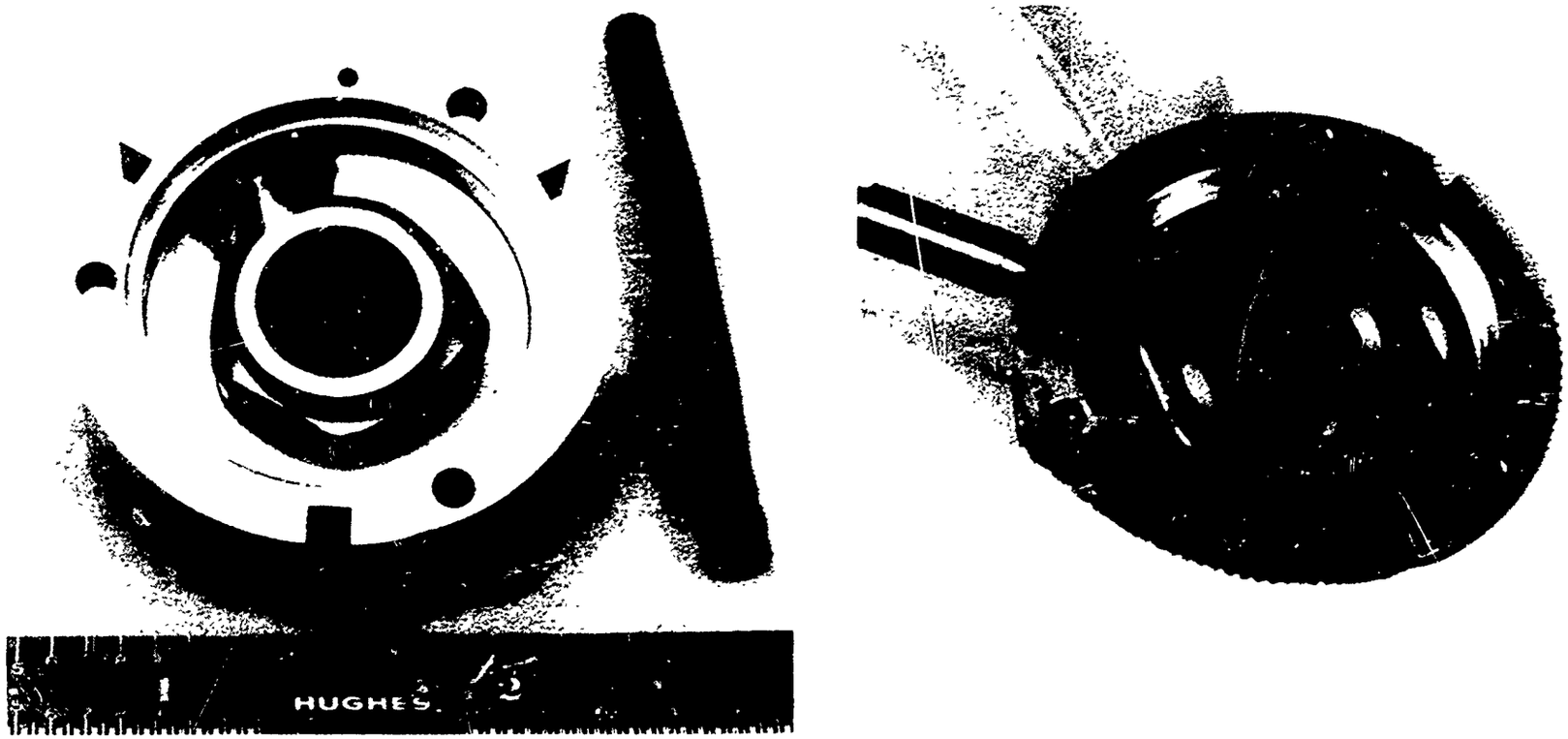

(a) Bladder at minimum volume

(b) Bladder at maximum volume

Figure 2-22. Oil reservoir and bladder of Mod C bearing.

The Mod C bearing has these improvements:

- Wicks eliminated
- Bearing flooded
- Soft diaphragm between oil and gas provides:
  - no oil loss in any attitude
  - large reserve for oil loss
  - compensation for changes in oil volume with temperature
  - pressurizes oil when RGG is at atmospheric pressure without an oil-to-air interface
- Purge time reduced, oil degassed separately.

b. Bearing Grooving

Hydrodynamic pumping in the Mod A, Mod B, and Mod C bearings is accomplished by shallow grooving in the pintle:

- Helical grooves 140 microinches deep on the cylindrical journal surface
- Spiral grooves 237 microinches deep on the thrust surface

These grooves were made by sputter-etching. The vendor did not hold the drawing tolerances on the depth, outline, or placement of the grooves. In addition, the sputter-etching left a thin nickel coating on the thrust surfaces which had to be removed manually.

Journal grooves with tolerances of 130 to 150 microinches run from 100 to 250 microinches deep. Most grooves were deeper on one side than the other due to the shadowing effect of the pintle flange during the sputter-etching. Thrust grooves with tolerances of 225 to 250 microinches run from 130 to 300 microinches deep. Thrust grooves vary in width by ±33%. Spare pintles purchased for RGG-1 have the thrust groove pattern 0.0015 inch off center for one and 0.003 inch for the other versus a drawing tolerance of 0.0005 inch.

Shaker Research Corporation was responsible for the Mod A and Mod B bearing designs and for the fabrication of the Mod A, Mod B and Mod C bearings. Shaker calculated that the bearings would still provide bearing stiffnesses above the original design goals and that the tolerances on the grooving could be relaxed to approximately ±10% and still provide stiffness within 4% of optimum.

It was concluded that the four Mod C pintles purchased for RGG-2 were superior to the Mod B pintles that were providing adequate service in RGG-1, except for one that had blockages in the grooves. It was replaced. The bearings and pintles have proven to be satisfactory. It should be noted that roundness on the pintles and bearings is typically 5 microinches versus a specification of 20 microinches. It was further concluded that sputter-etching is not the best way to form the grooves. Vapor blasting and other processes are capable of more uniform results and should be utilized in any further procurement.

c. Drag Cup Motors

Drag cup type motors provide torque that is relatively constant and free of ripple compared to other types of motors. The drag cup motors used in RGG-2 were unchanged from those used in RGG-1 except for the use of black anodize on the drag cups. See Figure 2-23. The anodize provides a more durable surface than bare aluminum and avoids galling at the close fits. It also reduces reflections on the speed control slotted disc with less concern for outgassing compared to the black paint used on RGG-1. The motor stator parts are seen assembled in the upper stator half in Figure 2-24.

d. Rotary Transformers

The rotary transformers seen in Figure 2-25 couple the RF power into the rotor and the FM signal out of the rotor without the friction drag of slip rings. The transformer coils of RGG-2 were bonded with an epoxy chosen for low-outgassing.

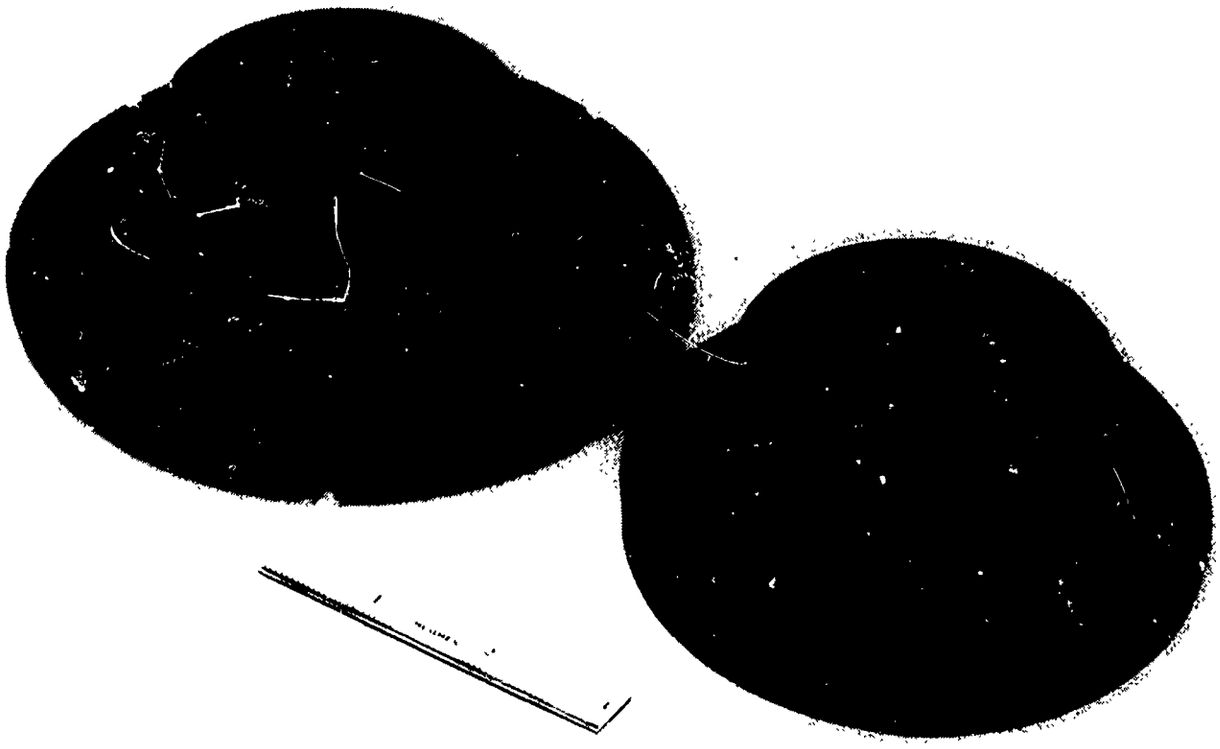

Figure 2-23. RGG drag cups, one with speed control slotted disc.

e. Coupling Capacitor

The ring capacitor seen in Figure 2-26 provides a means to transmit to the rotor the pulses used to turn the differential torque generator (DTG) off and on. One plate is attached to the lower drag cup on the rotor and the other to the lower stator half. The assembled clearance is 0.005 inch.

f. Stator Assembly

The stator provides support for the stationary parts of the bearings, motors, rotary transformers, coupling capacitor and speed control. It also provides a vacuum chamber so that windage and thermal conductivity between the rotor and stator are reduced.

The stator halves for RGG-2 are seen in Figure 2-27. The heater and temperature sensing wires have been wound in spiral grooves on the periphery and were later potted in place with a heat-conducting epoxy formulation called Delta-Bond.

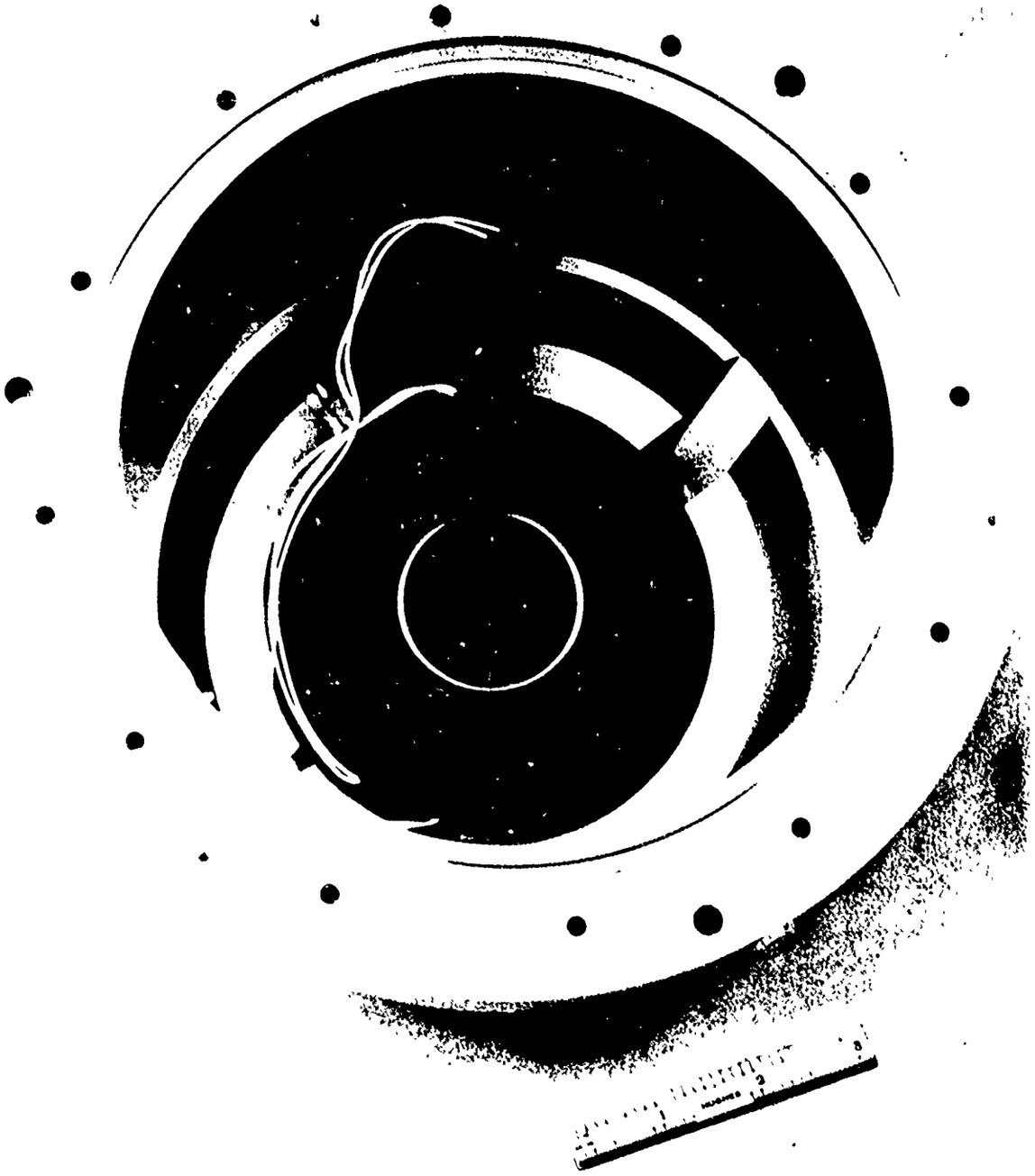

Figure 2-24. Lower stator half with spin motor and rotary transformer stator in place.

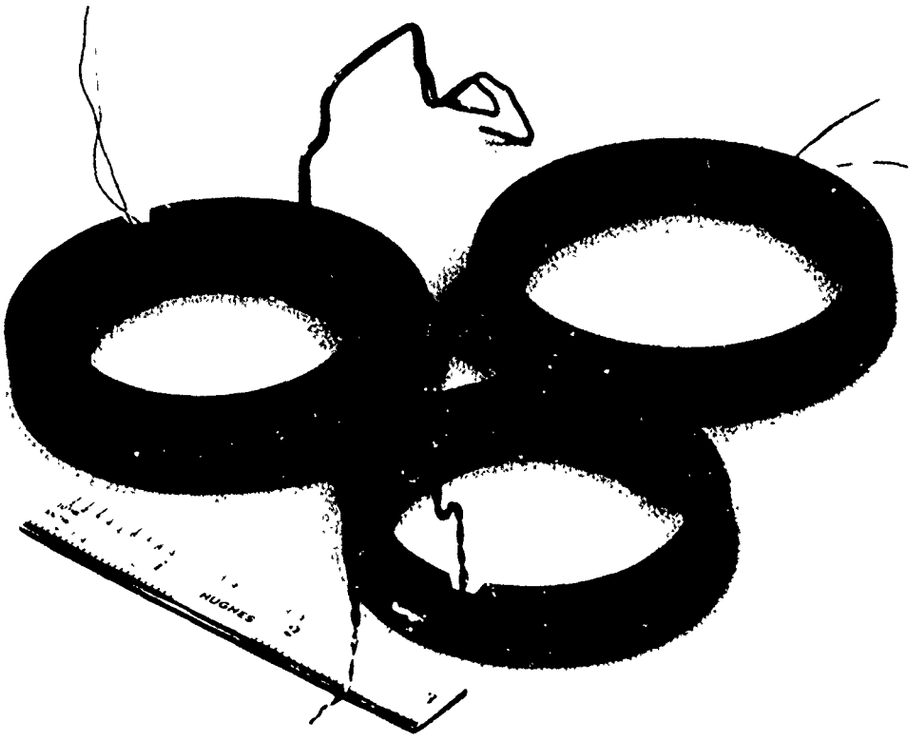

Figure 2-25. Rotary transformers.

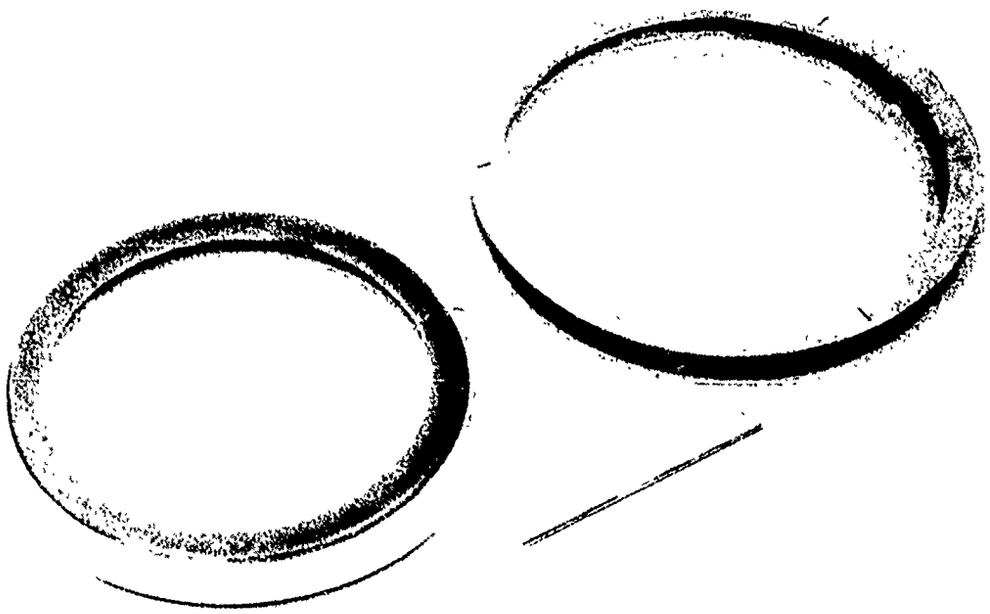

Figure 2-26. Coupling capacitor for DTG.

The RGG-2 stators are anodized to reduce galling and provide a more durable finish. Military standard (MS) fittings with o-ring seals are used at all vacuum connections in place of the pipe taps that used Teflon ribbon dope for sealing used in RGG-1. The o-ring seals provide more convenient assembly and disassembly and reduce contamination. Also seen in Figure 2-27 are the revised end caps that have the outer valves required for filling the Mod C bearings.

The stators for RGG-2 have tighter tolerances on the perpendicularity of the bearings. This fact, and the improved alignment of the rotor, have resulted in RGG-2 having less bearing friction than RGG-1 (as shown by longer spin-down times, and less variation in motor control voltage as the stator is placed in different attitudes with respect to gravity). The pintle bending in the bearings is about 30 microinches and will couple with misalignment of the bearing stators to cause differences in torque corresponding to differences in attitude. For the RGG-2, these differences are less than ±2.4%.

g. PE/LED Repackaged

The photo-electric/light emitting diode (LED) assembly seen in Figure 2-28 works in combination with the slotted disc seen in Figure 2-23 to form the rotor speed sensor. The LED is mounted on the bracket to the lower right in Figure 2-28. Its light is routed through prisms and lenses into the vacuum and focused on the slot edge. The light is then collected on the photo-electric sensor and preamplifier at the top right in Figure 2-28. The general arrangement of the optical path is seen in Figure 2-19.

For RGG-2, the PE/LED assembly was redesigned for ease of fabrication, reduced outgassing, and reduced volume to accommodate a magnetic shield over the RGG. The proven optical design and circuitry from RGG-1 were retained.

h. Final Assembly of RGG-2

The completed assembly of RGG-2 shown in Figure 2-29 has the external wiring and connectors added. The temperature sensing

Figure 2-27. Stator of RGG-2.

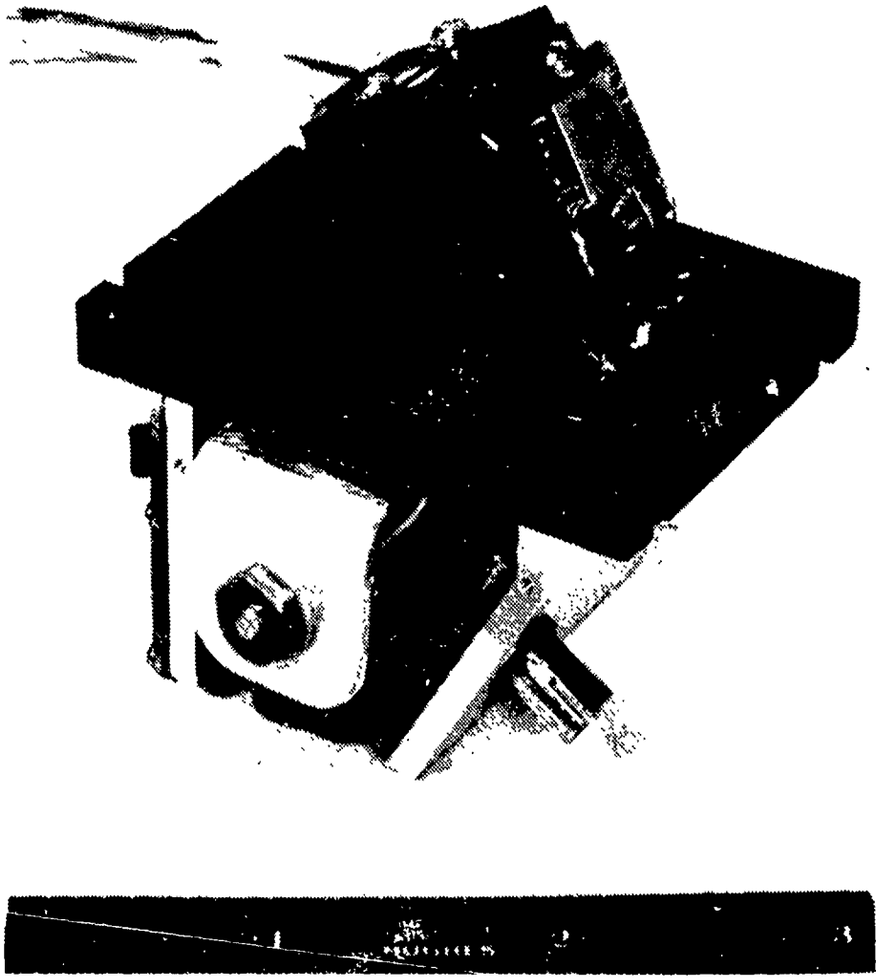

Figure 2-28. PE/LED rotor speed sensor.

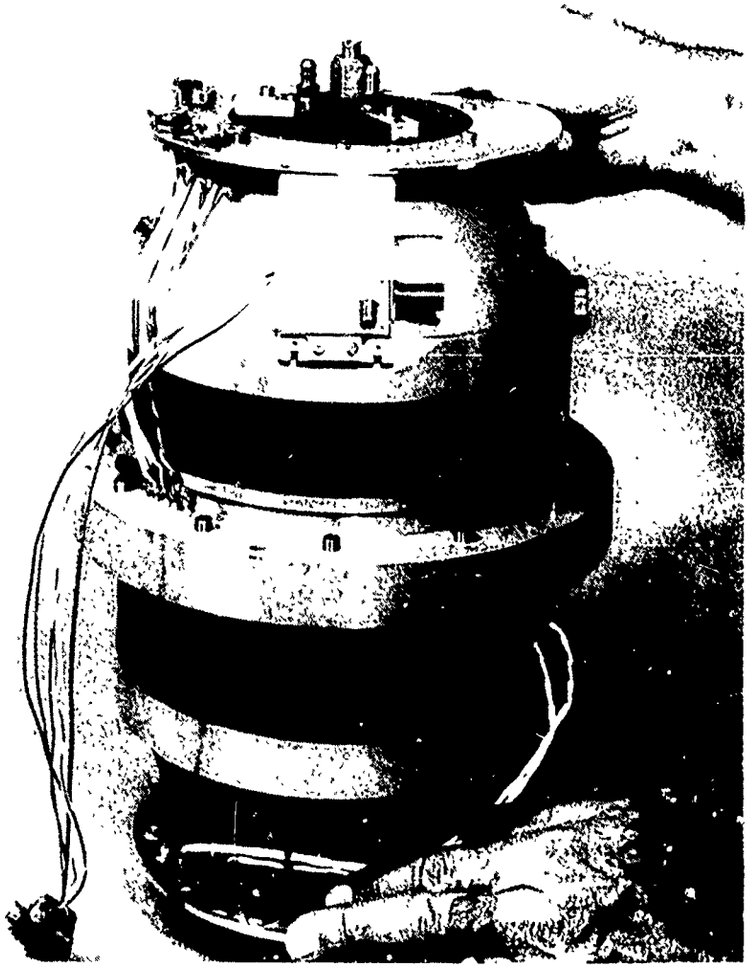

Figure 2-29. The completed RGG-2.

and heater wires have been potted and thermostats installed at each end to protect against over-heating. The thermostats are set to open the heaters at 130 F. The flanges that hold the connectors at each end have been strengthened to aid in handling the unit. As shown, the RGG-2 weighs 38 pounds.

The mounting flanges and electrical connectors of RGG-2 are the same as those of RGG-1 so that the units are interchangeable.

RGG-2 was first completed and ready for static error coefficient measurements on 24 November 1976. The first spinning operations with oil-filled bearings and closed-loop speed control were performed on 23 December 1976.

B. ASSEMBLY TECHNIQUES

1. General Considerations

Great care must be exercised in the fabrication of an instrument that is intended to resolve differences in specific force of 5×10^{-6} dynes between end masses that weight 5×10^{5} dynes, each, in earth's gravity (an enormous force ratio of one part in 10^{11}). The precautions taken in the fabrication, assembly and grooming of the RGG-2 sensor included:

- Every drawing was checked by the responsible engineer.
- Vendors were selected by proven performance, typically on RGG-1 parts.
- Spares were procured on all critical parts.
- Special procedures were implemented to obtain dimensional stability.
- Non-magnetic materials and tools were used.
- Engineering personnel witnessed inspection of critical parts.
- All parts were weighed.

- Preliminary assembly of all parts was performed to assure fit.

- All parts were cleaned thoroughly.

- The sensor was assembled in filtered-air bench, using gloves.

- Thorough washdown was performed before the sensor was disassembled for grooming in the filtered air bench.

2. Cleanliness

The concern for cleanliness has the following objectives:

- To avoid contamination of the bearings by particles and volatiles so that torques from the bearings and oil seals will be constant

- To obtain good adhesion for bonding

- To minimize volatiles within the instrument so that a good vacuum is obtained and windage torques reduced

- To minimize uncertainties due to mass transfer on the sensing arms.

Final cleaning and assembly was accomplished in the flow bench seen in Figure 2-30. The bench is equipped with 0.5 micron HEPA (high efficiency particle absorbtion) air filters. Parts were enclosed in clean plastic bags if they were to be removed from the flow bench or left overnight in the flow bench. The flow bench is cleared and cleaned after each operation.

The general procedures employed during final assembly included:

- All parts and tools ultrasonically cleaned in Freon PCA except pivot arm and stator halves. These large parts were wiped with MEK and rinsed with Freon.

- Bonding was performed with a space-proven low-outgassing epoxy.

- Screw fasteners were torqued tightly and uniformly.

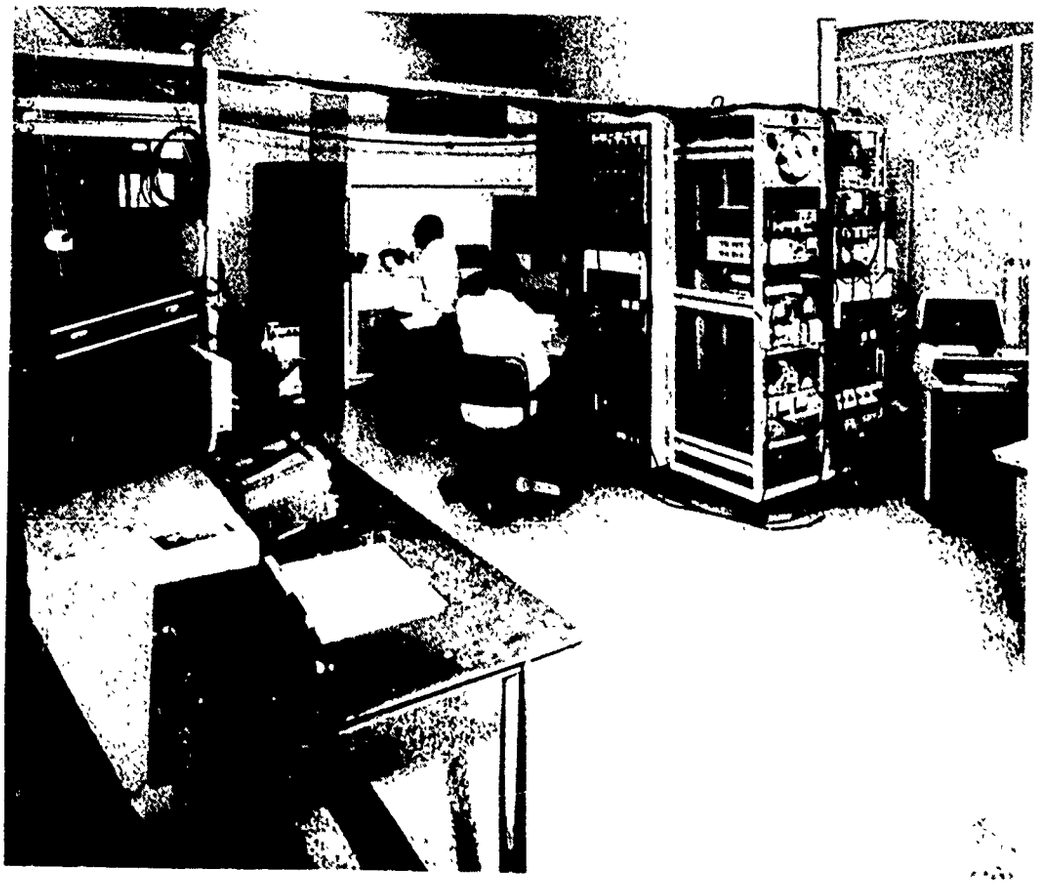

Figure 2-30. Flow bench used for cleaning and assembly.

- Lubricants used to prevent galling are low-vapor-pressure and are used sparingly.
- No use of bare hands was permitted.
- Tools were non-magnetic or were plated with non-magnetic material.

One of the problem areas encountered was lint from the Nylon knit gloves. The lint was rinsed off with a spray of Freon. Later work, particularly on the bearings, has been done using latex gloves. The latex swells in contact with Freon but the assembler learns to accommodate the resulting loose fit. The Nylon knit gloves are more rugged and are preferred for disassembly.

The extra care given to the RGG-2 in the area of cleanliness is believed to contribute significantly to the greatly reduced uncertainties of its performance data compared to RGG-1.

3. Rotor Assembly

a. Preloading the End Mass Bolts

The beginning step in the assembly of RGG-2 was to bolt the end masses into the pivot-arm to form the assembly shown in Figure 2-1. This was done as early as possible because the pivots are much less vulnerable to damage when the end masses are in place.

The operation starts with the measurement to the nearest 0.0001 inch of the spaces between the arm plates for each of the end masses. This was done with the lapped aluminum spacers (used during machining) in place between the arms. The aluminum bushings in the end masses were then trimmed so that the end masses were just 0.0086 inch shorter than the actual spaces. The 0.0086 accounts for two 0.0053 thick mica insulators and a compression of 0.0020 to be applied by tightening the bolt.

The end masses were then trimmed to be equal in mass within a total spread of 0.4 gram. The end masses and bolts were ultrasonically cleaned and the pivot-arm was swabbed and rinsed with solvent to remove grease.

A fixture was used to spread the arms so that the end masses and insulators could be inserted and the insulated bolts slipped in place. Before tightening the nuts on the bolts, the length of each bolt and the measurements across the arms adjacent to each bolt were recorded. Each bolt was then tightened incrementally using a wrench on the bolt head versus a wrench on the nut, while the pivot-arm rested on a "lazy susan" so that it did not take the torque. As previously calculated, each bolt stretched 0.0040 to 0.0042 in. while the end masses were compressed 0.00200 ±0.00005 inch.

The objectives of this procedure were to obtain a 1700-pound preload on the bolts and to avoid a compression of the pivots when the bolts were tightened. The 1700-pound preload assures a high unit loading at the interfaces so that the joints are not likely to slip. The 0.002-inch compression caused by the preload would have caused the pivots of RGG-1 to yield, except that bending of the arm plates relieved it. The procedure was first used on RGG-1S when the spare pivot-arm was assembled into the rotor. The much stiffer arm plates of RGG-2 would have put higher compression loads in the pivots if this procedure had not been used.

b. Match-boring the Rotor

Initial alignment of the pivot axis with the bearing axis was obtained by aligning the pivot-arm and end mass assembly inside the outer rotor and match-boring 12 holes through the central belt of the outer rotor and into the center flange of the pivot-arm. These holes are seen in Figure 2-16. Specially matched beryllium-copper alignment pins are used thereafter to obtain a close match to this initial alignment.

The set-up for the match-boring is seen in Figure 2-31. The alignment dowels at top and bottom were specially fitted in both diameter and length to position the pivot arm properly within the outer rotor. The eight large screws around the belt were then tightened to hold the parts in exact alignment during the match-boring of the 12 precision holes. The holes in the outer rotor are larger than the holes in the flange due to later requirements for skew axis alignment.

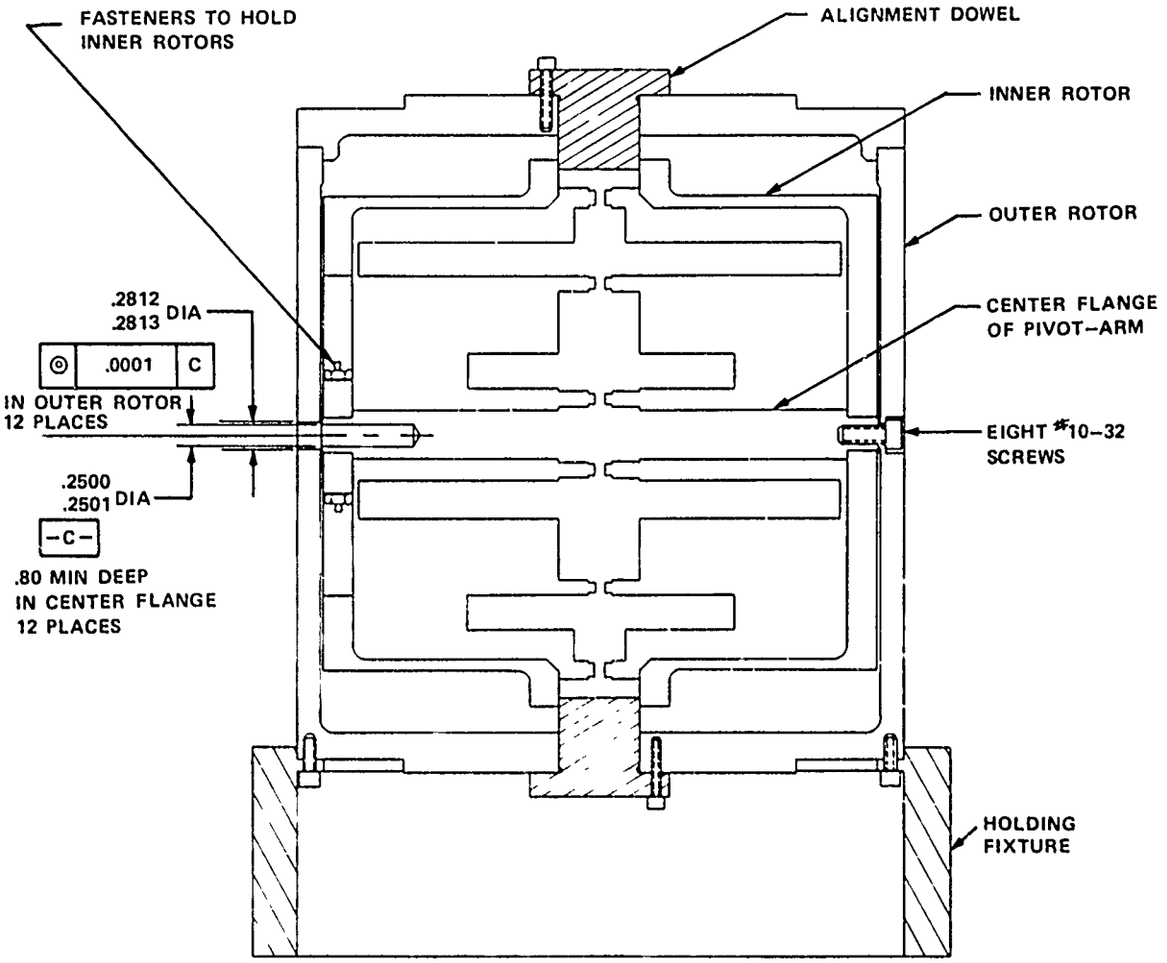

Figure 2-31. Rotor match-boring.

The use of the match-bored holes is illustrated in Figure 2-15. After the inner rotor assembly is positioned approximately within the outer rotor, the specially-fitted alignment pins are used to bring the torsion and spin axes into alignment within 200 microradians. The later operation of skew axis alignment is expected to align the axes within a few microradians as explained on page 61 of the March 1976 R&D Design Evaluation Report.

c. Preloading the Pivots

An axial tension of 10 pounds was desired in the pivots. The end pivots were put in tension by measuring the axial compliance of the pivots and using this information to trim the step in the plate that connects the pivot end flange to the inner rotor (see Figure 2-9). As the screws that hold the pivot flange to this plate are tightened, the gap between them is closed by dishing the inner rotor and stretching the pivots a very small amount.

The axial compliance of each inner rotor was measured as 67.5 microinches per pound and the stretch in the three pivots on one side of the center flange was calculated as 4.5 microinches per pound. The gap needed to provide the 10-pound preload was thus 0.00072 inches at each end.

The preload is not expected to be a uniform 10 pounds on all six pivots because of the influence of the arms in bending. The stiffness of the arms for this type of bending is estimated to be 1.3×10^5 pounds per inch so that a residual difference in length between the pivots and the end masses of only 80 microinches could cancel or double the preload in the pivots. The 3.76-pound weight of a sensing arm could then put a pivot in compression.

Tension in the pivots is considered desirable to help keep all six pivots in precision alignment. Ten pounds was chosen because it puts a stress of only 1273 psi in the smallest pivot. The yield stress for the 6061-T6 aluminum alloy is 40,000 psi. Clearly a higher preload should be used if it is desired to maintain all the pivots in tension. This subject should be re-evaluated before another sensor is made.

A related subject is the axial vibration sensitivity. These subjects deserve further study.

d. Installation of Transducers, ACA's and DTG

A specific sequence of events must be followed to install the piezoelectric transducers in order to have them unstressed when the sensing arms are at rest. The sequence is constrained by mechanical clearances when working through the access holes in the inner rotors and between the arm plates. The recommended sequence is:

(1) Start with the inner rotors installed on the pivot-arm/end mass assembly and the pivot spacers secured. The support pivots are thus tied to the rotor in their final location. A necessary previous step is to install the microbalance assemblies on the sensing arms because they are inaccessible with the inner rotors in place. The inner rotors must have all wiring bonded in place before installation.

(2) Install the anisoelastic coefficient adjusters (ACA's). They cannot be installed after the counterweights for the transducers are installed.

(3) Install the transducer mounts; leave the screws with the free play removed but not tight. The transducers cannot be put in place after the counterweights are installed.

(4) Install the counterweights.

(5) Put the stainless steel dummy transducers in place complete with mica insulators, clamps, and special screws. Torque both ends to 10 inch-pounds, then tighten the screws that hold the transducer mounts. The transducer mounts are now positioned and the dummy transducers can be removed.

(6) Install the transducers and torque their special screws to 10 inch-pounds. The transducers must have lead wires attached prior to installation.

(7) Install the stops and carefully set them for 0.005 inch clearance on each side of the end masses, using shims. Connect the lead wires to the stops to form the differential torque generator.

(8) Connect the electrical leads and the one-mil-diameter gold flexure wires to the transducers. The gold wires must be the last items installed as they are very hard to see and are very easily broken.

A consequence of this assembly sequence is that the counterbalances must be removed to change the ACA's and the gold wires must be replaced after each such operation. Another consequence is that rotation of the inner rotors relative to the center flange of the pivot-arm (in order to preload the pivots in torsion and thus adjust the axial vibration sensitivity) will put a bending bias in the transducers. It may therefore be worthwhile to remove the transducers and reposition their mounts (using the stainless steel dummy transducers) if a large pivot twist is needed. The stops may also need to be repositioned.

e. Installation of Electronics

The rotating electronics circuit boards are placed on top of their respective inner rotors with 0.080-inch spacers to separate the copper clad thermal shields of the circuit boards from the end bells of the inner rotors. The wires that must connect the transducers, the DTG, and one board to the other, are connected by a small loop of wire to standoff terminals on the inner rotors. The loops can be seen in Figure 2-3. The spacers are then removed and the electronics are suspended by the 18 wire loops.

A thermistor is bonded into an aluminum disc that fastens to the pivot spacers. The thermistors on either end of the sensing structure give a good indication of the temperature of the pivots and sensing arms.

The leads that connect the transducers, DTG, and electronics boards are magnet wire; they are bonded into slots in the inner rotors. See Figure 2-3. A problem that was difficult to diagnose developed where a wire was bent sharply over an edge of the anodized inner rotor. The insulation on the wire flaked away on the inside of the bend and made intermittent contact with the structure. Rounded edges and wire bonds with more generous radii will be used henceforth.

The completed electronics boards were ultrasonically cleaned in Freon PCA before installation. The few necessary reworks were accomplished through as small a hole as possible in a clean plastic sheet placed over the board. The object was to prevent flux and solder from splattering into hard-to-clean places. The flux was removed with MEK solvent on cotton applicators and then the whole inner rotor assembly was given a shower in clean Freon PCA. This care has paid off in the low outgassing of the RGG-2.

Another measure to reduce outgassing can be seen in Figure 2-3. The small holes in the inner rotor near each standoff terminal are vent holes for the air that would otherwise be trapped under the screw-in terminals.

The major outgassing sources in the electronic boards are the components themselves and the epoxy-glass fiber laminated boards. In the future, the use of ceramic printed circuit boards must be considered.

f. Assembly of Inner Rotor Into Outer Rotor

The ability to extract the sensing structure from the rotor quickly, make precise revisions in the balance screws, then expeditiously reassemble the rotor and put the RGG into operation on the test stand was a goal of the RGG-2 redesign. The grooming time for an RGG is presently a few months because a minimum of 15 disassemblies are necessary to accomplish coarse balance, anisoelastic coefficient adjustment, fine balance, and skew axis alignment.

It has become routine for a two-man team to disassemble the rotor, make balance screw adjustments, clean the subassemblies, and reassemble the rotor in approximately four hours. The following assembly sequence will help to illustrate the procedure. The procedure takes place in the flowbench, by personnel wearing gloves.

(1) Remove two of the four screws that hold the top pivot spacer and attach the inner rotor holder seen in Figure 2-16.

(2) Lubricate the periphery of the center flange then lift the inner rotor assembly and slide it carefully into the outer rotor as seen in Figure 2-16. The I axis of the two subassemblies must be kept in approximate alignment.

(3) As the match-bored holes in the center flange become visible through their counterparts in the outer rotor, there will be significant drag because the diametral clearance between the center flange and the outer rotor is less than 0.0003 inch on the 6-inch diameter. Move the parts to attempt to engage the four beryllium-copper support posts of the bottom electronics board in their sockets so that the inner rotor can continue to the centered position. It may be necessary to lay the nearly mated assembly on its side and guide the posts into the sockets with a conical tool.

(4) Line up the match-bored holes as well as possible by eye, using three jack screws in the holder to adjust the height of the inner rotor in the outer rotor.

(5) Insert at least one alignment pin in each quadrant to achieve precision alignment of the inner rotor in the outer rotor. This must be done carefully and with the pins lubricated because the clearance of the pins with each part is less than 0.0001 inch.

(6) Insert the eight No. 10-32 screws in the periphery of the rotor and tighten them incrementally to 32 inch-pounds. Check that the alignment pins are free to rotate, then remove them. The pivot arm center flange, and thus the entire inner rotor assembly, is firmly attached to the inside of the outer rotor.

(7) Remove the inner rotor holder and replace the two screws that hold the pivot spacer, torquing them to 12 inch-pounds.

(8) Install the lid on the outer rotor, being careful that the support posts for the upper electronics are engaged in their sockets. This lid has a pin so that axis alignment with the cup of the outer rotor is assured. Torque the eight No. 6-32 screws that hold the lid to 12 inch-pounds, using an alternating progressive pattern. The bearings, rotary transformers, drag cups, slotted disc, and DTG coupler are permanently mounted to the ends of the rotor so they are now properly aligned and secure.

(9) Install and torque the four screws in each end that secure the electronics boards.

(10) Slip onto the pins from the electronics boards that project through the vent holes in the outer rotor, the two connectors at each end from the rotary transformer windings. Do the same for the lead to the DTG coupler.

The rotor is now fully assembled and resting on its supporting fixture, ready for assembly into the RGG stator.

4. Stator Assembly

a. Permanent Installation of Motors

The spin motor and rotary transformer stators were bonded into the RGG stator halves. Before the bonding took place, the wires to the rotary transformers had to be in place in grooves cut under the shoulders where the motor inner and outer stator rings were to mount. In the upper left of Figure 2-24 the twisted magnet-wire leads of the rotary transformer stator can be seen attached to their feed-through terminals. The transformer is the centermost dark grey ring. The motor leads are Teflon insulated. They were held by small aluminum clips that were bonded in.

Prior to bonding, the motors were checked by actual operation. The lid of the outer rotor was fitted with a drag cup and a pintle and was spun up on a bearing in each stator half. One motor stator winding was found to have incorrect identification of leads so that the motor at first ran in reverse. Reversing the leads corrected the problem.

A fixture was used to center the motor and transformer stators, leaving a generous glue line. The adhesive used was Epiphen 825A. This epoxy formulation was used for most bonding operations in the RGG and proved to be very strong and to make a good seal if an adequate glue line was provided.

An example of the strength of the bond occurred when the fixture was not properly engaged and the rotary transformer and inner motor stators were bonded eccentrically into the lower stator half. They had to be removed. A special wheel puller was constructed to try to save the parts. After 6 hours in the oven at 280°F the force necessary to pull the parts out was such that the motor laminations were dished and delaminated and the rotary transformer ferrite had multiple fractures. It was difficult to remove the remaining epoxy.

The alignment fixture was then reworked to permit visual inspection of its engagement. The removed parts had to be scrapped and replaced. The second bond was successful.

b. Heater and Temperature Sensing Windings

The heater windings seen in Figure 2-27 consist of a 22.1-foot length of Chromel "A" 0.015-inch diameter-wound bifilar in the deep grooves (see Figure 2-19) of each stator half. The temperature sensing wire is Balco 7066 cut to 460 ohms at 75 F (about 19 feet) and wound bifilar in the shallow grooves. The grooves were later filled with Wakefield Delta Bond heat conducting epoxy to protect the wires and provide better thermal contact. Trimming resistors for the temperature-sensing wire were mounted from the standoff terminals seen at the left in Figure 2-27. The stator halves were then complete and ready for final assembly.

c. Adjustments for Axial Clearances

Adjustments were needed to set the total axial clearance of the bearings to 0.0002 to 0.0003 inch with the RGG operating at temperature equilibrium. The coupling capacitor to the DTG needed an axial gap of 0.003 to 0.005 inch and both rotary transformers needed their ferrite cores axially aligned within 0.005 inch. To accomplish this, many measurements were taken of the rotor and stator parts and spacers were made to fit under the flanges of the bearing stators. The spacers can be seen in Figure 2-19.

The procedure followed for the RGG-2 was to make the top and bottom spacers the same so that a mix-up would not affect the axial locations. The value selected, 0.0340 ±0.0001 inch, results in 0.0005-inch nominal axial interference in the bearing, this to be accounted for by thinning of the thrust washer in the top bearing. The various parts were axially symmetrical such that the calculated mismatch of the rotary transformer cores was only 0.0020 inch at the upper core and 0.0005 inch at the lower core, assuming a 0.0001 inch operating clearance in the bottom bearing. There is no means for observing this mismatch directly.

The brass surfaces of both the rotor and the stator of the coupling capacitor were machined after bonding to their insulators so that the runout of each was less than 0.001 inch total. The height of the stator insulator was reduced by 0.0479 inch to provide a maximum clearance of 0.0050 inch between the plates.

At final assembly the thrust runner of the lower bearing was in final position. The thrust runner of the top bearing was backed off by several mils. Tightening the six screws in the thrust plate (the light colored disc seen in Figure 2-20) pushed the thrust runner forward until the total end play of the rotor in the stator was the desired value.

The value of end play needed is dependent on the difference in operating temperature of the rotor and the stator. A figure of 5 F was chosen based on measurements of RGG-1. The overall rotor length is 8.900 inches across the pintles and the expansion of aluminum is 13.1×10^6 (in/in)/deg. F so the temperature correction is 0.00058 inch. Adding the operating clearance of 0.00020 to 0.00030 inch the desired end play was 0.00078 to 0.00088 inch.

The measurement of end play was made with the spin axis horizontal. With no force applied, the difference reading on the dial indicator was 0.00065 inch, but with a few pounds of hand force maintained at each end of the rotor axial travel, the reading was 0.00078 inch. This was considered satisfactory so the thrust washer between the thrust runner and thrust plate, see Figure 2-19, was lapped to suit and

was installed. The final measurement at that time was 0.00068 inch with no force applied, and 0.00080 inch with several pounds force applied.

The clearance in the coupling capacitor was checked by loosening the lower bearing with the RGG axis vertical and measuring the axial motion of the rotor until it came to rest on the capacitor plates. This value was 0.0045 inch versus the specification of 0.003 to 0.005 inch. It is thus considered that all axial positioning requirements were met.

Recently, the axial clearance in the bearings was remeasured as 0.00105 inch with the spin axis horizontal. A new thrust washer, 0.0002 inch longer than the one removed, was installed. The end play was then measured with the spin axis vertical, using a Bently proximity probe and inverting the RGG. This measurement indicated an end play of 0.00165 inch with the RGG near operating temperature. Some conclusions are drawn from this finding:

- The axial clearance is larger when operating with spin axis vertical than with spin axis horizontal because of the compliance of the rotor and stator end bells.

- The additional clearance is only about half of the indicated 0.0008 inch. This is because the 18-pound weight of the rotor is primarily reacted on the bottom. The axial force in the top bearing will be small with the larger clearance. The measurement was obtained with the 18 pounds reacting on each end in its turn as the instrument was inverted.

- The clearance cannot be reduced to accommodate vertical operation or else the horizontal operation would be jeopardized. Example: if the heat to the RGG is turned off during horizontal operation, so that the stator cools rapidly with respect to the rotor, the required spin motor excitation voltage soon increases significantly. This indicates the axial clearance is becoming too small.

- The increased clearance for vertical operation causes no problem. The operating clearance for the bottom bearing is near 50 microinches, whether the top clearance is 150 microinches or 1200 microinches (0.00165 -0.0004 -0.00005).

5. Final Assembly

The Final assembly procedure for RGG-2 is outlined in Figure 2-32. The AF numbers designate assembly fixtures. Steps 6 and 7 are associated with setting the bearing end play and are normally bypassed during grooming operations. The procedure has been accomplished in one hour and 45 minutes with a two man crew, eliminating steps 6 and 7, including mounting the RGG-2 on the test stand with electrical connections made and ready for excitation.

6. Filling the Mod C Bearings With Oil

The bearings that support the rotor run immersed in a highly refined instrument oil that is confined by rotating seals around the pintles. The interior of the RGG is evacuated to reduce windage torques and thermal conductivity. The pressure in the oil must also be reduced to a very low value or it will increase the friction of the rotating seals and it will leak past the seals. However, when the pressure of the oil is reduced, the air dissolved in it forms bubbles and the oil foams to a volume many times its original volume.

a. Equipment

The solution of this problem in the Mod C bearings is to de-gas the oil separately from the bearing, evacuate the interior of the bearing, then introduce the oil into the bearing starting at the bottom and filling upward so that residual air will be pushed out of a port at the top of the bearing. When the bearing is free of bubbles, valves in the ports are closed and the bearing is ready for operation. The complete operation is carried out with vacuum in the RGG, in the bearings, and in the chambers and tubes containing the oil.

To prevent any leak in an oil valve from pressurizing a bearing and causing oil to leak past the seal, the valves were made in pairs. An inner valve closes off the oil from the vacuum in the interior of the RGG; an outer valve closes the passage through the RGG end cap. The two valves can be connected to pass oil from outside the RGG into the

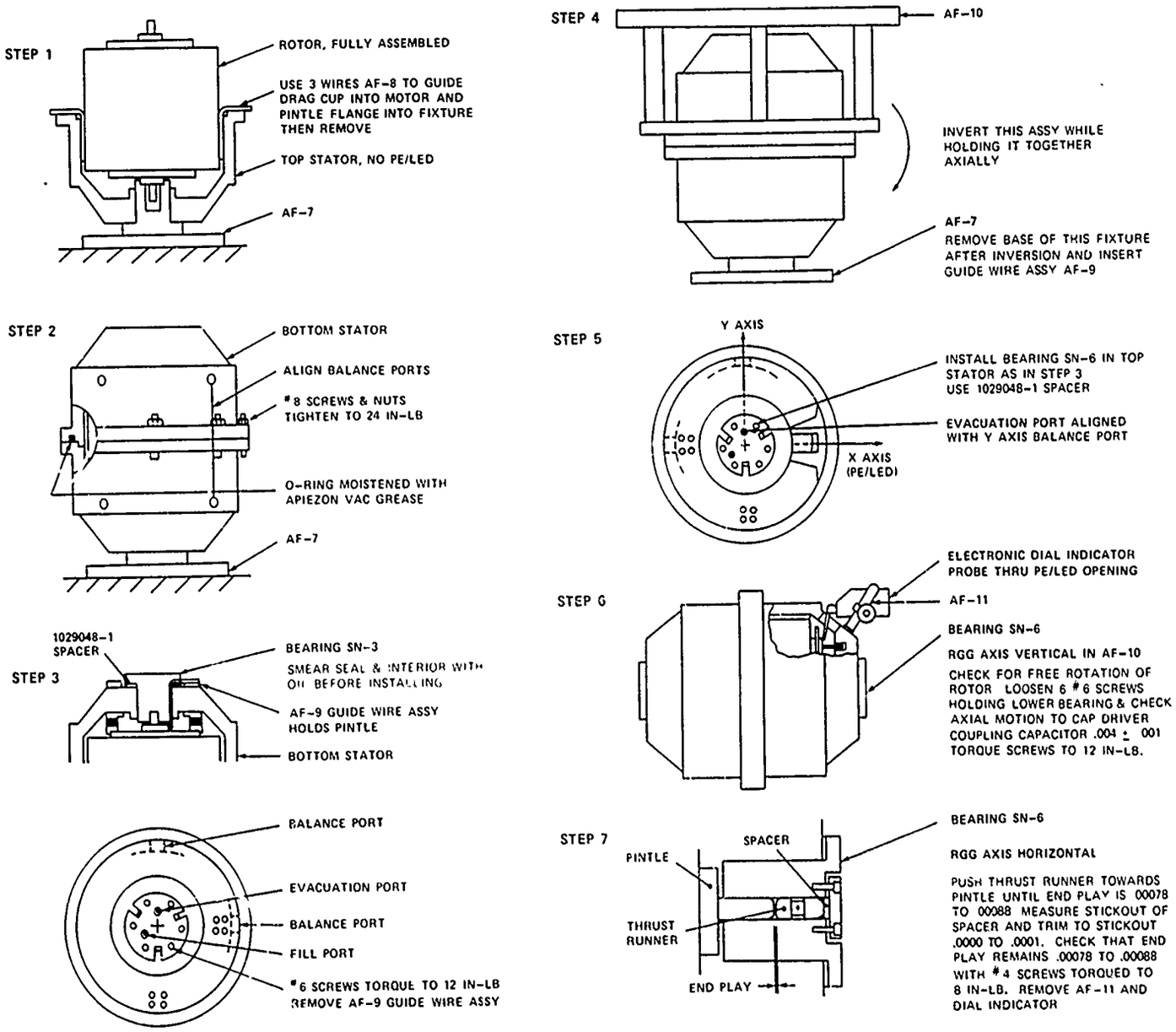

Figure 2-32. Final assembly procedure RGG-2.

bearing, or they can be separated so that each connects into the interior of the RGG. This arrangement is shown in Figure 2-33.

Normal operation of the bearing is with all valves closed and disengaged, as illustrated at the bottom in Figure 2-33. For this condition a leak in an outer valve will not pressurize the bearing but will simply represent a larger load for the vacuum pump used on the RGG. A leak from the inner valve will allow oil into the space under the end cap. Significant leakage from an inner valve is unlikely because the pressure in the oil is kept very low by the soft diaphragm.

b. Procedure

For the bearing-filling operation the apparatus shown in Figure 2-34 is connected to the RGG. The filling operation is conducted as follows:

(1) All fill and evacuation valves are opened and disengaged. The two separatory funnels are charged with 50 to 100 milliliters of oil each. The oil is Nye SRG-40 oil with a viscosity of 15 to 19 centistokes at 120F. The stopcocks on the separatory funnels are kept closed while the RGG and filling apparatus are evacuated and leaks are detected and corrected. The apparatus is allowed to de-gas overnight.

(2) When a pressure less than 100μ (100 micrometers of mercury, 10^{-1} Torr) is maintained in the filling fixture and less than 50μ in the RGG, the stopcocks can be opened slightly to permit oil to foam into the stainless steel pots. The foaming is controlled so that the pressure in the filling apparatus does not exceed 100μ. De-gassing normally requires less than four hours. The stopcocks are then closed and the vacuum in the fill fixture improves to less than 50μ.

(3) The 0.8-micron particle filters at the bottoms of the pots restrict the flow of oil so that it is hours after the start of de-gassing before a significant amount of oil begins to collect in the transparent Tygon tubing that leads to the fill ports. When this happens, the outer valves of the fill ports are closed. The tubing is filled with oil by closing the vacuum valve to the pot and permitting dry, filtered air to enter the pot and force the accumulated de-gassed oil through the filter and into the evacuated tube. The air valve

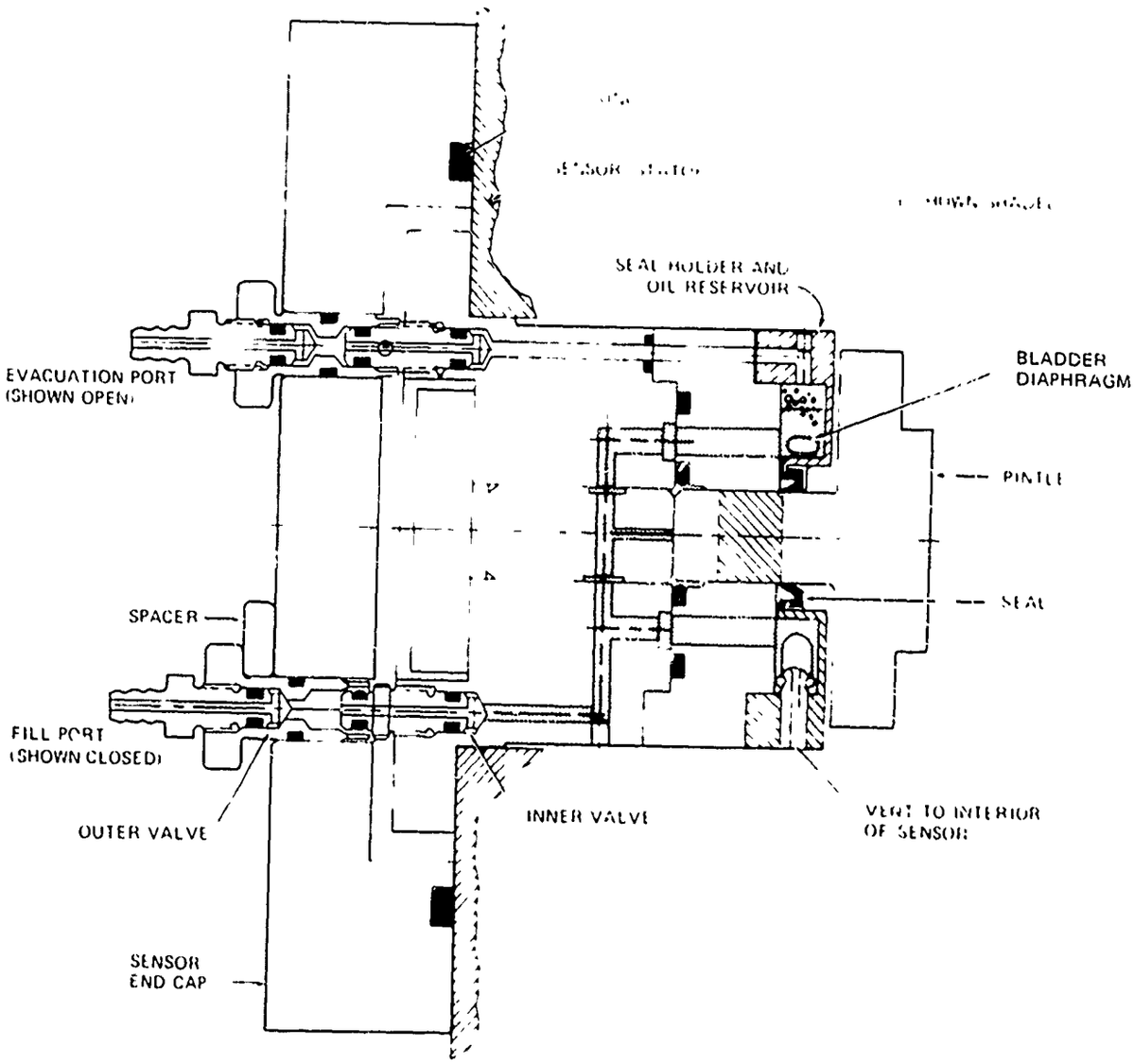

Figure 2-33. Mod C bearing with evacuation and fill ports.

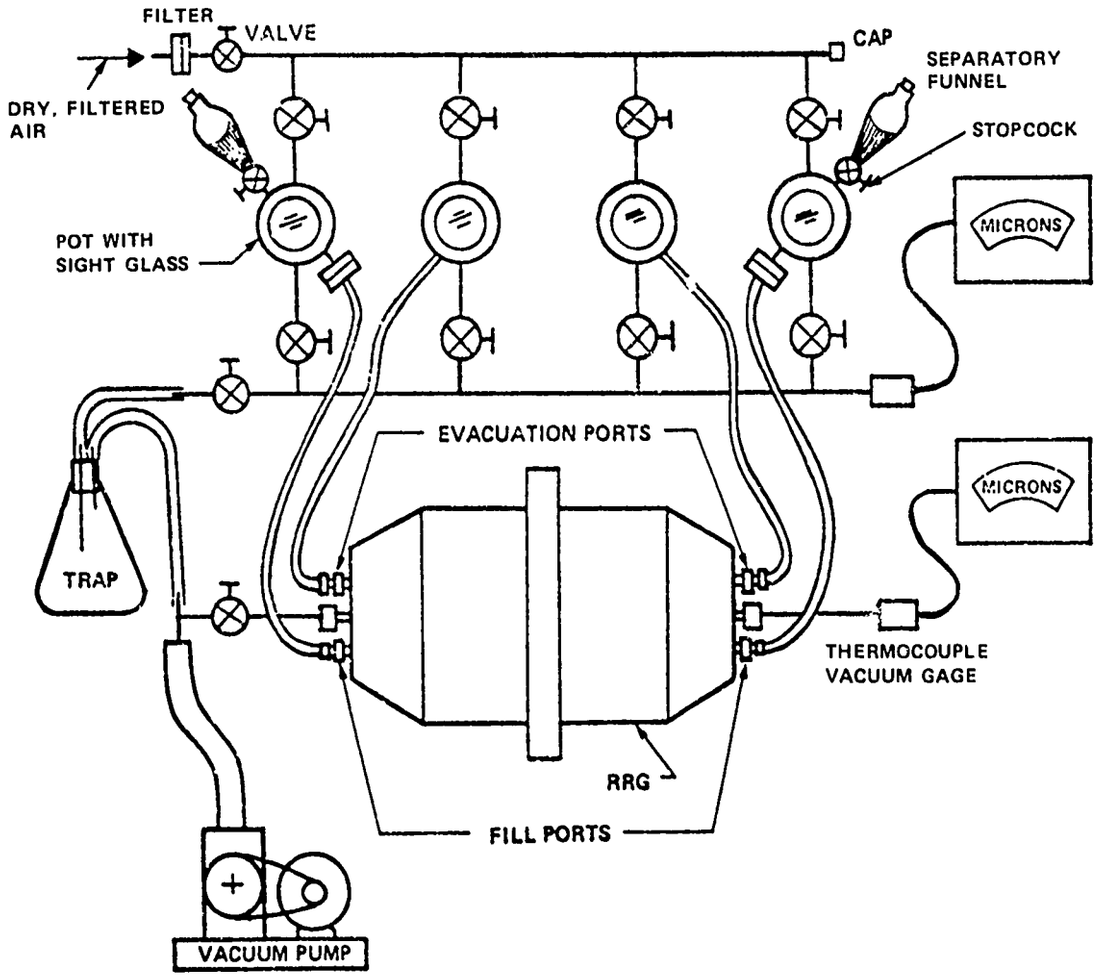

Figure 2-34. Oil degassing and bearing filling apparatus.

is then closed and the pot is re-evacuated. Very few bubbles form on the undisturbed surface of the de-gassed oil when vacuum is re-established in the pot. This shows that the oil does not absorb air readily.

(4) The inner and outer valves of the fill and evacuation ports are then engaged and opened. The interiors of the bearings are thus connected to vacuum through the fill apparatus instead of venting into the RGG. Oil now moves slowly into the low parts of the bearings and rises in the bearing under the influence of gravity on the column of oil in the fill tube. After several minutes, the oil emerges from the evacuation port at the top of the bearing. There are a few bubbles and then the oil becomes clear.

(5) The transparent tubing of the evacuation line is arranged to be almost horizontal for several inches as it leads away from the evacuation port. After oil moves into this line for about two inches the fill valve is closed. The low pressure head in the horizontal evacuation line allows bubbles that may form in the bearing to work their way up and out of the bearing. If the tube is not horizontal, bubbles are inhibited by the pressure under the column of oil.

(6) The spin motors are now energized and the rotor is brought up to speed, approximately 17.5 rps, and left running. This circulates the oil through the bearing and flushes the gas pockets so that any trapped air or volatiles are brought out into the reservoir where they can work their way to the evacuation port, the highest point in the bearing. The RGG stator temperature is set to 130F. Several hours are allowed to elapse, typically overnight, while the bearings are pumped via the evacuation lines. Bubbles are encouraged to escape via the evacuation ports by tipping the RGG spin axis 30° or 60° from horizontal with one end up and then the other. Several minutes are spent in each such attitude. Usually, very few bubbles are noted except those known to be due to slow leakage in the tubing attachments.

(7) When bubbles no longer come from the bearings, the inner and outer fill and evacuation valves are closed tightly and separated. The separation is maintained by spacers as seen in Figure 2-33. At this time the pressure in the fill fixture is typically 30 microns and in the RGG 20 microns. The tubings and fill fixture are removed, the RGG temperature control is reduced from 130F to 110F, and the fill is complete. The reduction in temperature reduces the oil volume and allows the bladder diaphragm to expand.

c. Results

Several problems have been encountered during the filling procedures. The largest problem was leakage in the bearing: o-rings, cemented joints, one bladder, and three lip seals leaked. The motor excitation voltage was unusually high following two fill operations because oil had leaked into the gaps of the rotary transformers and spin motors.

The exhaustion of oil from a bearing is typically preceded by low and very irregular torque required from the spin motors to maintain constant speed. When the torque begins to climb again it signals that the bearing is in the boundary lubrication regime and the spin motor must then be stopped to avoid damage to the bearing surfaces.

Many variations in the fill procedure were tried. The major improvements were observed after testing was instituted to insure that the bearing and its oil connections were leak-tight before assembly. The complete bearing with a substitute pintle is pressurized to 5 psig with air and immersed in Freon. If it does not show bubbles after 5 minutes it is qualified for assembly.

The filling of the bearings with oil has many pitfalls because the interior of the RGG and the bearings cannot be observed. The only indicator of bearing health is the excitation to the spin motors. At the present writing the bearings have been running for over a month on fill number six. The spin motor excitation remains high, indicating adequate oil. Fluctuations in the motor excitation, the sources of which can only be hypothesized, keep the staff nervous. It is generally felt that investigation of the bearing design and filling techniques is

urgently needed to assure good bearing performance over extended time periods.

C. ELECTRICAL

RGG-2 incorporates several improvements in the sensor internal electronics. These were straightforward in concept and implementation so that they had a low risk of failure, but the improved operation and versatility are significant. These improvements have all been operating for several months and are considered to be proven features.

1. Differential Torque Generator

Electrically charged capacitor plates are pulled together by electrostatic forces. This electrical property has been utilized in RGG-2 to introduce a precise differential arm torque that can be turned on or off by external commands or signals. One of the pair of capacitor plates is mounted on, and is a part of, the arm motion limit stops as discussed earlier. The arm end mass forms the other - the ground-side of the capacitor plate pair. The four active capacitor plates are arranged as shown schematically in Figure 2-35.

The attractive force pulling charged capacitor plates together is

$$F = \frac{V^2 C}{2g} \text{ newtons}$$

where:

V = voltage across the plates in volts

C = capacity between the plates in farads

g = gap between the plates in meters

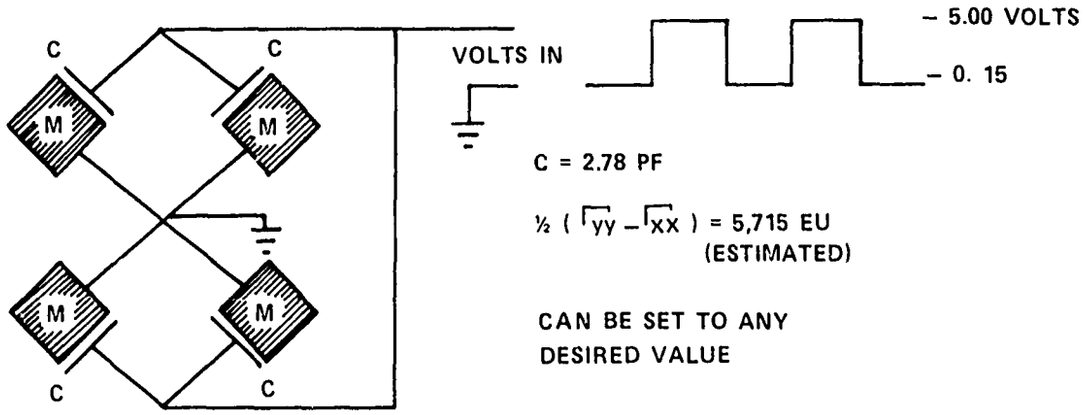

Figure 2-35. Differential torque generator (DTG) schematic.

The capacity of one plate to one end mass is

$$C = \frac{KA\ 10^{-12}}{0.1130g} \text{ farads}$$

where:

K = relative dielectric constant of air or vacuum = 1.000

A = effective area of one isolated plate to an "infinite" area end mass = 4×10^{-5} meters squared

g = capacitor plate gap 1.27×10^{-4}m (0.005 in)

C = 2.78×10^{-12}f

The total differential torque (DT) between the two arms is four times the force (F) of one capacitor acting on a lever arm length which is the distance from the pivot to center of plate, $\ell = 0.0628$ m. For an applied differential voltage of 5.00 V, the total differential torque is:

$$DT = 4Fl = 4 \times \frac{V^2\ Cl}{2g} \text{ N.m}$$

$$= 6.87 \times 10^{-8} \text{ nt m}$$

$$= 0.687 \text{ dcm}$$

The voltage applied to the capacitor plates is a 2ω square wave, 0 to +5.00 V dc. The peak value of the 2ω fundamental component of the torque wave is then

$$DT_{peak} = \frac{0.687}{2} \times \frac{4}{\pi} = 0.437 \text{ dcm.}$$

Assuming the difference of the transverse arm inert inertias to be 38,270 $gmcm^2$, the previously calculated DTG torque of 0.437 dcm ideally will produce a principal channel output gradient of 5715 EU.

$$\Delta Gp = \frac{1}{2} \times \frac{0.437 \times 10^9}{3.827 \times 10^4} = 5715 \text{ EU}$$

This estimate is subject to several errors, the largest of which are

- Vibration calibration errors
- Arm mass capacitive voltage divider
- Capacitor plate spacing
- Applied capacitor voltages

Vibration calibration enters because the gradiometer scale factor is set by measured balance screw change effects. That is, we vibrate the gradiometer at a certain vibration level that is accurate to about ±5%, and then calculate the gradiometer acceleration sensitivity coefficient. Screw turns required to reduce this sensitivity to zero are then calculated and the adjustments made. The gradiometer is again vibrated and the sensitivity coefficient again calculated. If the vibration sensitivity coefficient has not been reduced to zero, the computer scale factor is changed to account for the "known" mass balance change that was made. Since the screw turns can not be made exactly, and since the masses of the screws are not known exactly, and since the vibration level also is somewhat uncertain, the absolute scale factor may be in error by as much as ±10%.

As discussed in a previous section, the original arm-current-loop was opened by insulating the masses from the clamping bolts and the clamping bolts from the arms. These insulating sections form a capacity voltage divider and thus the actual voltage applied to the capacitor is reduced by about 6%. Since the differential torque is proportional to the square of applied voltage, the actual torque reduction due to this effect is about 12%.

The capacitor plate spacing is also quite critical. The capacitor force equation was written above using the symbol C for the capacity. However, if we replace C by its own equation, the force equation becomes

$$F = \frac{V^2 \, KA \, 10^{-12}}{0.226 \, g^2}$$

Since the nominal gap is only 0.005 inch, an error of ±200 microinches (4%) produces a torque error of ±8%.

The voltage applied to the torquing capacitors is derived from a regulated supply, coupled by an FET logic gate to a resistor voltage divider. The divider voltage is then chopped by a saturating transistor. The absolute accuracy of this combination is estimated to be about ±5% in voltage, resulting in a torque uncertainty of about ±10%.

Although the absolute accuracy of the calculated torque is not high, the stability of the generated torque should be excellent. The application of the DTG will be discussed in a subsequent section of this report and it will be shown that generated torque stability is by far the most important feature of the DTG.

The delta printout due to the application of the DTG is 4702 EU. This is equal to 82% of the previously calculated estimate of 5715 EU. In view of the possible error sources discussed above this is considered to be a good check on theory.

The DTG is excited by applying a 2-ω, 0- to 5-volt square wave to the capacitor plates. This square wave is produced by triggering a very-high-speed bistable flip-flop. The flip-flop is triggered by spikes coupled into the sensor rotor through a small rotary capacitor at one end of the rotor. The spikes are generated by differentiating a square-wave TTL logic signal which is generated by the slot-corrected photocell pulses from the encoder disc. Thus, the DTG is driven by a precisely regulated voltage that is precisely phase-locked to the RGG rotor. The phasing is such that all of the signal appears in the GP channel at 0 phase.

2. Extra Signal Channels and Monitor Capability

RGG-2 provides three separate signal channels and one spare. Their designations are

- Normal gain - 2ω filtered
- Low gain - 2ω filtered
- Low gain - unfiltered

The gradiometer also allows an accurately known test signal to be injected at the signal channel input to test the channel gain and phase shift. In addition, the differential torque generator (DTG) can be excited selectively and independently.

The internal sensor power supply unregulated and regulated dc voltages can be monitored, and the resistance of a pair of precision thermistors can be measured. These thermistors are embedded in the end-pivot termination structures and thus allow an accurate estimation of sensor end-pivot temperature to be made.

These extra signal and monitor capabilities of RGG-2 have already proven to be very useful.

3. Sensor Electronics Mounted on Outer Rotor

The internal sensor electronics printed circuit boards (PCB's) for RGG-2 are similar to those of RGG-1 except that they are flat and they have one extra layer of copper cladding on the boards. This extra layer of copper provides a relatively low thermal resistance path for the individual electronic components and also connects to the mounting studs which provide the final heat sink path to the outer rotor.

One of the electronics boards can be seen in Figure 2-3 temporarily mounted on the inner rotor. The four large studs standing up from the top surface of the board provide the final mount.

Mounting of the PCB's on the outer rotor has removed all heat sources from the inner rotor. Thus, heat can be conducted to or from the arm and pivot structure only through relatively high thermal resistance paths to large, high-capacity masses, and this results in a long thermal time constant for the tuned-rotor frequency shift with temperature. This is exactly what is needed for the temperature compensation concept discussed in a subsequent section.

SECTION 3

RGG ENVIRONMENTAL OPERATIONAL COMPENSATION CONCEPTS

Practical airborne environments could generate gravity gradiometer output errors unless the environmental effects are measured and compensated. It is shown in a subsequent section that modern, high-quality inertial platforms have a small residual angular jitter about one or more of their axes unless the platform is especially designed and constructed to reduce the residual jitter. This angular platform jitter can generate gradiometer output errors. Such special platforms are well within the state-of-the-art, but they are large and expensive compared to conventional platforms. A concept of compensating for the angular jitter of a conventional inertial platform is discussed.

Another operational problem relates to the precise control of the gradiometer internal (arm-pivots) temperature. It is shown elsewhere in this report that the gradiometer stator temperature can be controlled to the required accuracy. However, in a practical airborne environment the internal temperature may vary slightly over long periods of time. A method of detecting and compensating for these internal temperature variations is described.

A. ANGULAR RATE COMPENSATION

Transverse angular velocities of the RGG stator produce rotational-field specific force gradients whose average values (low-frequency components) appear directly as part of the gravity gradient output of the sensor. In moving-base applications, rotational field gradients are minimized by mounting the gravity gradiometers on a stable platform, but the residual rotational field gradients may still require real-time compensation to produce acceptable performance.

In theory the compensation of rotational field gradients is quite simple, i.e., the filtered squares and products of the appropriate angular velocities are subtracted from the gravity gradiometer output

signals. In practice, the rotational field compensation problem is a little more complex. First, a suitable measurement of each angular velocity must be made, i.e., with sufficient accuracy over a large band of frequencies. Second, the squares and products of these measurements must be formed with sufficient accuracy, bandwidth, and dynamic range. Finally, the resultant squares and products must be smoothed by a filter which simulates the gravity gradient signal filter process, and the resultant smoothed functions must be subtracted from the gravity gradient measurements.

In anticipation that available gyros may not have all of the required characteristics for rotation field gradient compensation, consideration is being given to an instrument with the functional characteristics of an angular differentiating accelerometer. This device has a second-order transfer function between input inertial angular velocity (ω_i) and its output signal (ω_m) as shown by (1).

$$\omega_m = \left[\frac{S^2}{S^2 + 2\alpha S + \beta_o^{\,2}}\right] \omega_i \qquad (1)$$

More specifically, the device provides a passive "high pass" measure of inertial angular velocity.

It has been determined that when the output of this sensor is squared, filtered and subtracted from the squared and filtered input function, the result is equivalent to a second-order low-pass filter acting on the input rate insofar as the resultant rotational field gradient is concerned. This can be demonstrated as follows: For illustrative purposes, let the input rate be a periodic function of arbitrary amplitude and frequency as in (2).

$$\omega_i\,(t) \triangleq W \operatorname{Sin}(\omega t) \qquad (2)$$

The resultant output function (ω_m) is also periodic with amplitude and phase modified by the measurement transfer function as in (3), where K and ϕ represent the amplitude and phase of the transfer function at the input frequency.

$$\omega_m (t) = KW \operatorname{Sin} [\omega t + \phi] \tag{3}$$

The difference of the average values of the squares of the input and measured rates is given by (4).

$$\langle \omega_i^2 - \omega_m^2 \rangle = 1/2\ W^2 [1 - K^2] \tag{4}$$

The square of the amplitude function of (1) is given by (5), and its difference from unity is given by (6).

$$K^2 = \frac{\omega^4}{(\beta_o^2 - \omega^2)^2 + 4\alpha^2\omega^2} \tag{5}$$

$$(1 - K^2) = \frac{\beta_o^4 + (4\alpha^2 - 2\beta_o^2)\,\omega^2}{(\beta_o^2 - \omega^2)^2 + 4\alpha^2\omega^2} \tag{6}$$

When the measurement transfer function damping is set to $\sqrt{2}/2$, the second term in the numerator of (6) vanishes to yield (7).

$$(1 - K^2)\Big|_{a = \beta_o/\sqrt{2}} = \left[\frac{\beta_o^4}{\beta_o^4 + \omega^4}\right] \tag{7}$$

Thus, from (4) and (7) the difference of the average values of the squares is given by (8).

$$<\omega_i^2 - \omega_m^2> = 1/2\ W^2 \left[\frac{\beta_o^4}{\beta_o^4 + \omega^4}\right] \tag{8}$$

Now, let's filter the input rate (ω_i) by a second order low-pass filter to form a new output rate defined by (9).

$$\omega_o \triangleq \left[\frac{\beta_o^2}{S^2 + 2\ \beta_o^2 J + \beta_o^2}\right]\omega_i \tag{9}$$

From the input rate definition of (2), the average value of the square of (9) is given by (10).

$$<\omega_o^2> = 1/2\ W^2 \left[\frac{\beta_o^4}{\beta_o^4 + \omega^2}\right] \tag{10}$$

Observe that (10) is identical to (8) and that the process which produced (10) is therefore equivalent to the process which produced (8). Each of these processes is illustrated in the block diagrams of Figures 3-1 and 3-2.

Performance evaluation of the rotation field compensation process is simplified considerably with the aid of the equivalent process of Figure 3-2. For example, consider that the gravity gradiometer stable platform has a 15-Hz stabilization bandwidth and that it has a 2-arc-second jitter amplitude at this frequency. This represents a rate amplitude of about one milliradian per second with an uncompensated output gradient of about 250 EU, i.e., ($1/4\ W^2$). If the corner frequency of the filter ($\beta_o/2\pi$) is set at 1 Hz, the attenuation of the equivalent filter at 15 Hz is 225. Thus, the equivalent rate after filtering is approximately 5 microradians per second with a residual output of approximately 0.005 EU. This represents a reduction ratio of 50,000:1.

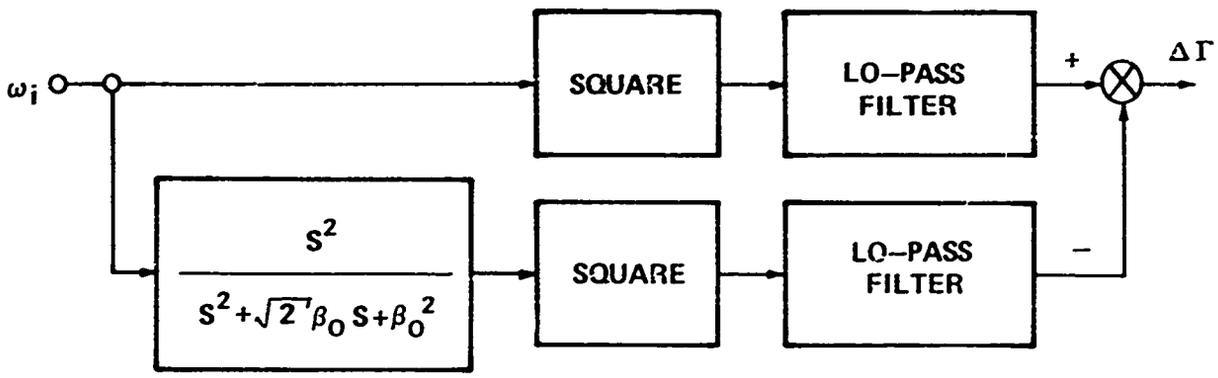

Figure 3-1. Rotation field compensation process.

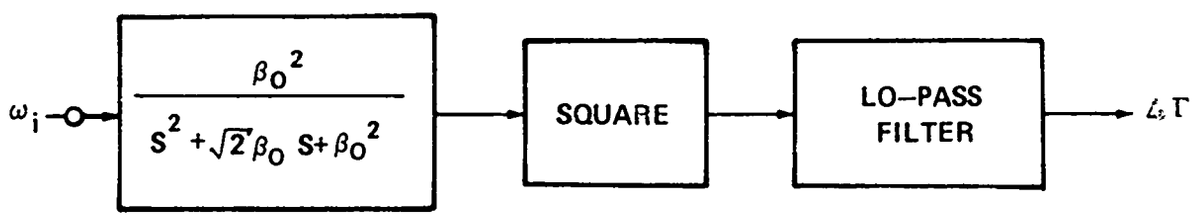

Figure 3-2. Equivalent process.

The attenuation of rotation field errors will be less spectacular at lower frequencies, but it is expected that this techniqu · of rotation field compensation will prove to be a very practical method of achieving the performance objectives of operational moving-base gravity gradient measurement systems in the future.

B. DTG AUTOMATIC TEMPERATURE COMPENSATION CONCEPT

The resonance frequency of the RGG differential mode is a function of the temperature of the internal pivot-arm structure. As a result, internal temperature changes cause changes in the gain and phase of the RGG signal process which result in output signal changes. These output signal changes can be kept within acceptable bounds by stabilizing the gain and phase of the RGG signal process. This can be accomplished by one of three methods: (1) direct internal temperature control, (2) correlated rotor speed control, and (3) closed-loop signal process control. This latter method is the basis of the DTG Automatic Temperature Compensation Concept.

The DTG is a powerful new feature of RGG-2 which can alleviate the necessity for either super-precision temperature control of the pivot-arm structure or the necessity for speed changes to compensate for minor temperature changes. Either alternative would be difficult to implement, the first for obvious reasons and the second because speed changes in themselves cause minor variations of temperature.

Simply stated, the DTG compensation scheme requires the measured DTG output to be compared with a fixed value; any deviation from the norm can be used to cause the computer to correct the phase and magnitude of the measured gradient signal. Thus, the gradiometer output signal remains unaffected by the changed temperature condition. This DTG compensation scheme is made possible because the RGG system is linear over the small temperature changes which can be expected at the pivot-arm structure.

In Section 2.C.1, the Differential Torque Generator (DTG) is discussed in detail. It was stated for stabilized temperature-speed conditions, that the delta DTG output signal appears as a plus (+) signal in the GP channel with zero phase shift. (The "delta" DTG signal is defined as that change in the gradient output signal which is attributed to the added differential torque supplied during the DTG "on" periods).

It is important to note that the DTG introduces a precisely reproducible signal magnitude at zero phase when the sensor is at its reference temperature. Second, the DTG can be turned on and off at precisely controlled intervals. More specifically, the DTG can be energized in the following sequence continuously: 35 rev ON/35 rev OFF/35 rev ON/etc., where 35 revolutions = 2 sec. The time versus delta-output-response of the sensor under this condition will be approximately as shown in Figure 3-3. A special computer subroutine can be used to take a continuous one-half-hour moving window average of the delta signal difference between the DTG ON and OFF periods, in both the GP and GC channels. Although the magnitude of the difference can be calculated, it will be much easier to measure it. This delta signal is expected to be of constant magnitude and zero phase angle for a constant temperature sensor. Of course, this constant delta torquing signal will be subtracted from the printed output values so that the measured gradients are not changed by the DTG signals.

If the temperature of the RGG sensor should change slowly—it has a thermal time constant of hours as previously discussed—the phase and magnitude of the output will then be adjusted accordingly and the correct values will be printed. In essence we are saying that:

- The gradiometer has a linear, predictable, stable response to temperature changes.
- The DTG will induce a constant-magnitude, constant-phase arm torque that can be demodulated at a relatively high frequency with respect to the system averaging times.

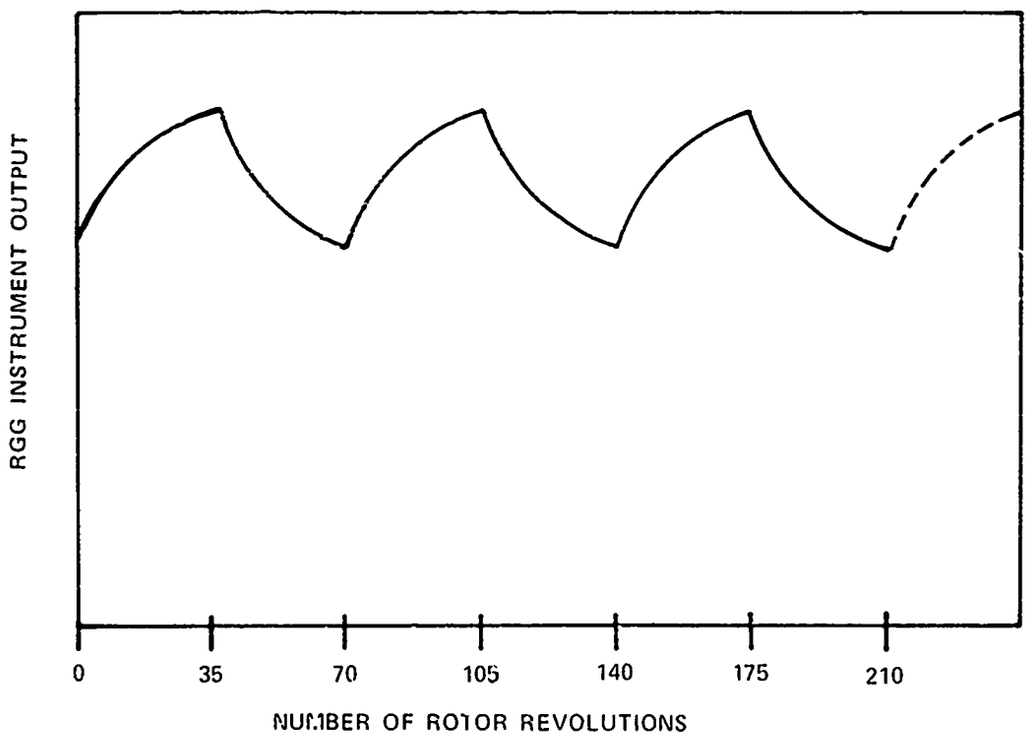

Figure 3-3. Gradiometer sensor output for 50% ON-OFF duty cycle.

- That by demodulating the delta DTG component signals, we can detect and correct for signal phase and magnitude changes due to sensor temperature changes, so precisely, that the errors in the true signal remain within the error budget even though the sensor resonant frequency shifts by a significant amount.

We realize that the ultimate signal detection process will probably be more exotic than a simple moving window filter and that the ON-OFF cycle timing may differ from the two-second example just described. However, this simple concept is easy to visualize and fundamentally sound. Because of the DTG tests which have been performed to date on RGG-2, we have a very high expectation that the DTG compensation scheme will operate exactly as hypothesized.

SECTION 4

RGG-2 SYSTEM OUTPUT DATA FORMAT

Since the RGG-2 has additional signal channels, monitor capabilities, and sensor logic states, formats and operating details vary considerably from those of RGG-1. Therefore a detailed description of the RGG-2 data printout and logic state settings is provided in Appendix B.

PRECEDING PAGE BLANK-NOT FILMED

SECTION 5

NEW EXTERNAL ELECTRONICS

Since a new set of external electronics was required for independent operation of RGG-2 some improvements were made in the circuits and all of the packages were condensed. Numerous convenience features were added. Figure 5-1 shows all of the new external electronics mounted in a single rack with some room to spare. The more important elements of the system are discussed in the following paragraphs.

A. TEMPERATURE CONTROL

The new temperature control and its power supply are the two units at the top of the rack. The controller uses the original concept of bifilar heater wires wound between lands on the RGG sensor stator. On top of the lands are bifilar wound Balco temperature sensing elements that form a four-arm bridge, along with two precision high-stability resistors. This bridge is excited by a 1-KHz, 10-V rms stable oscillator. The bridge output unbalance is amplified by high-gain tuned filters and then phase-sensitive demodulated to dc. The dc gain of the controller is very high, approximately 18 kilowatts/deg F, but feedback limits the gain to 1/100 this at anything over a few 1/100 Hz. Due to the long thermal time constant of the RGG, this factor provides the extremely well regulated average temperature that is required.

In addition to the closed-loop control circuit, an open-loop monitor channel displays the temperature control bridge unbalance directly on a panel meter. The least readable division on this meter is 0.0002 F (0.01 F full scale). As might be expected this monitor fluctuates continuously about an average hang-off of 0.002°F. The absolute accuracy of the monitor is probably not better than a few tenths of one degree F, but since we are interested only in a stable temperature, not an accurate one, the absolute accuracy of the monitor is of little importance.

PRECEDING PAGE BLANK-NOT FILMED

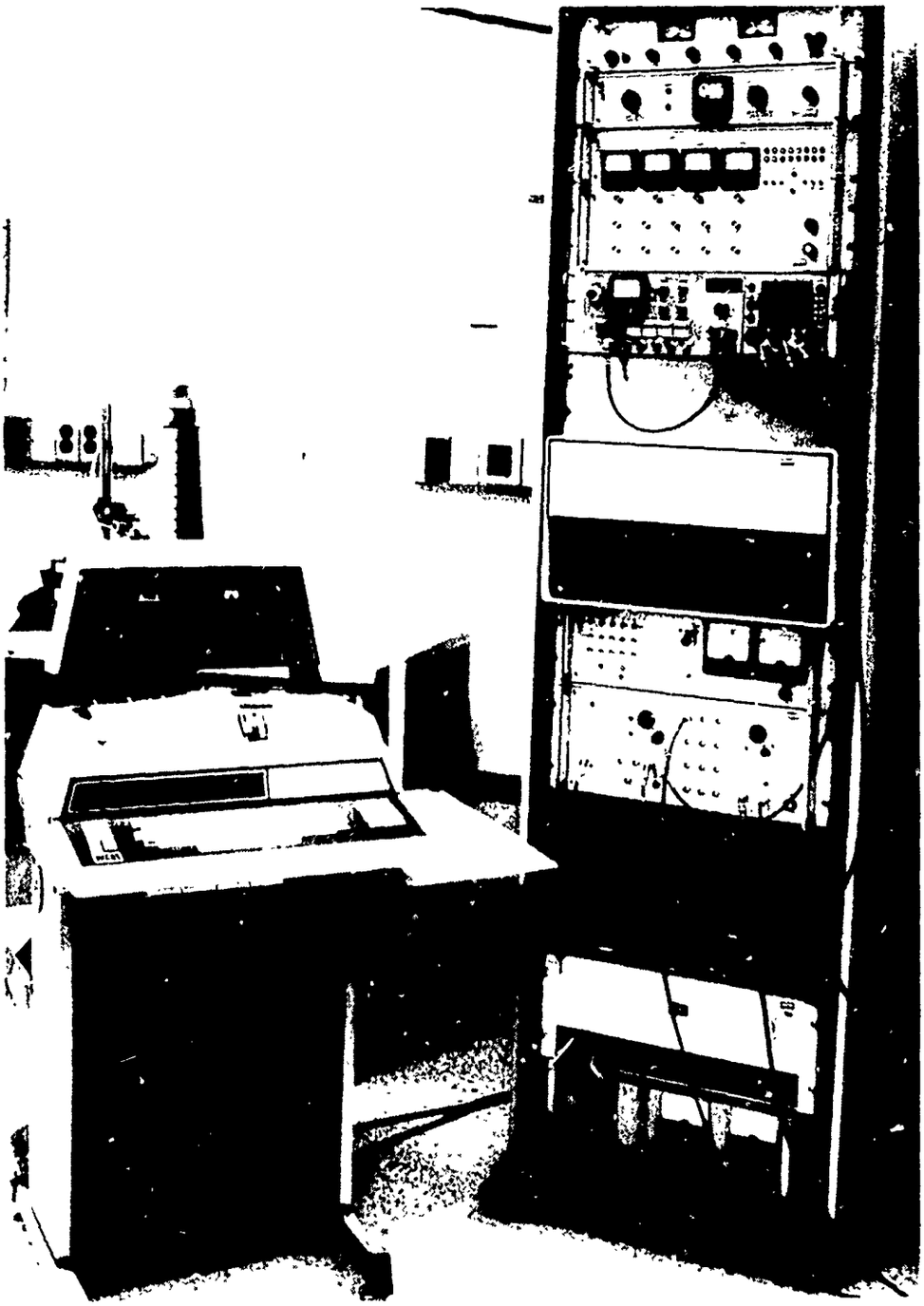

Figure 5-1. GGI electronics built for rotating gravity gradiometer serial No. 2.

B. NEW ANALOG ROTOR SPEED CONTROL SERVO

The analog section of the speed control servo was redesigned for two reasons. First, it was physically much larger than necessary, and second, the amplitude of the voltage for the spin motor reference phase was not as stable as was desired. The importance of the reference phase amplitude stability arises for the following reason. The servo motors are normally operated with nearly equal reference and control phase amplitudes, for example, 15.00 and 11.30 V rms, respectively.

These voltages generate a specific rotor torque level and a specific watt loss level in the rotor drag cups. The loss in the drag cups causes a specific temperature rise of the rotor and thus a definite sensor resonance operating speed. The control field voltage varies slightly, but the variations are small and the average nearly constant. Thus the rotor temperature rise is nearly constant and the sensor remains tuned to resonance. However, if the reference phase voltage varies, the control field must change to compensate and the average rotor drag cup loss changes and hence the rotor temperature.

We monitor the control phase voltage of the servo motors almost continuously during normal operation as an overall evaluation of probable system performance. This is discussed in more detail in a subsequent section.

C. SIGNAL CONDITIONER IMPROVEMENTS

The concept of the signal conditioner has been discussed in depth in previous reports. Briefly, for test purposes we generate 1-, 2-, 3-, and 4-ω square-wave and sine-wave reference signals of various fixed and adjustable amplitudes. These test signals must be precisely phase locked to the photocell pulses for the spinning sensor rotor.

The signal conditioner for RGG-1 did not have a 3-ω signal capability and if the sensor rotor speed was changed, the sine wave filters had to be readjusted to get the proper output phase. The new signal conditioner panel corrects both of these problems.

D. BUILT-IN MONITORS

In Figure 5-1 on the right hand, near the center of the top half of the rack, a small oscilloscope and a digital multimeter are visible. These two monitor elements allow almost all of the system electrical signals to be measured, checked, and evaluated simply and rapidly. They have proven to be great time savers.

E. PRINTING TERMINAL

A General Electric Co. Terminet 30 was selected for the new printing terminal. It is a relatively quiet, rugged, continuous-duty device. It has a cartridge ribbon that lasts for weeks of continuous operation and a fan-fold sprocket feed paper supply that is also adequate for several weeks of continuous operation. This terminal is a significant improvement over a conventional teletype.

SECTION 6

RGG-1 BALANCE TUBE INSPECTION

During the month of June 1976, RGG-1 was completely disassembled for the first time since February 1975, when transducers, balance tubes, and components on the sensing structure were installed. It is true that RGG-1 was partially diassembled many times during the grooming cycles from April 1975 through May 1976, but RGG-1 was never disassembled to the extent that the balance tubes could be examined visually. It had been known for many months that the balance tubes were not electrically functional, but this fact had presented no problems since none of the experimental activities involved ultra precision balancing of the sensor. In fact, the type of laboratory activities up to June 1976 did not even require adjustment of the small balance screws. Thus, the malfunctioning balance tubes were considered to be a very low priority problem.

During the June 1976 disassembly, the balance tubes were examined under high magnification, and all of the fused quartz tubes exhibited one or more modes of failure. In most cases, the quartz was fractured at the tube ends near the epoxy seals which both bond the electrodes to the quartz tube and seal the tube ends to prevent leakage. The fractures in the quartz permitted small amounts of mercury and electrolyte to escape from the capillaries, thereby rendering the tubes inoperable.

Our shelf stock of spare balance tubes was then examined and to our surprise, most of these tubes had also failed, and in a similar manner. Thus, the high-g, vacuum environment of the RGG-1 sensor was exonerated as a contributing factor in these failures. Liaison with the vendor, Curtis Instruments, soon revealed, to his surprise, that his shelf stock also exhibited the same problems.

The fundamental problem apparently concerns the use of epoxy in direct contact with fused quartz, a material which is described as a "super cooled liquid." As the epoxy cured, it simply fractured the quartz at or near the margin line of the epoxy on the quartz surface.

The use of quartz had been chosen by the vendor, in lieu of glass, to avoid electrolyte contamination, a problem which had been known to be caused by leaching of sodium from the glass. Thus, one problem was avoided but another created. Unfortunately, the general fracturing phenomenon caused by epoxy in contact with quartz is rather well known and should have been foreseen.

Thus, the tube parameters should have been considered in more detail before selecting the particular epoxy-quartz combination used in the manufacture of the balance tubes. Our prior purchase of balance tubes on an earlier contract yielded no similar problems simply because the standard commercial glass tubes were purchased. Such tubes were not considered useful for the final RGG configuration for several reasons, including the fact that the electrical leads were made of a magnetic material.

Subsequent to the discoveries of the failed tubes, discussions were held with the vendor which produced a proposed plan of action to evaluate combinations of tube materials and cements. It is believed if such a plan had been implemented that the balance tube requirements would have been satisfied. However, further work in this area was terminated due to a careful evaluation of program priorities which considered the factors of test objectives, problem solving priorities and funds availability. In brief, the problem with the balance tubes was neither a serious one nor one which required further effort at the time.

As of February 1977, the laboratory work with RGG-1 and RGG-2 has yet to produce levels of sensitivity which either confirm or deny the need for a super-precision balance capability. However, RGG-2 was assembled with the balance tube mounting brackets and the necessary electrical components in anticipation of a retrofit program.

Our general experience with inertial instruments indicates the probability that minor mass shifts will occur with time. Thus, it will be highly desirable to counteract such unbalances without disassembly of the sensor. Two alternative candidate solutions, the use of balance

tubes or the use of piezoelectric inchworms, appear to offer viable solutions, if and when such a need is established.

SECTION 7

STATIC BALANCE ADJUSTMENTS OF RGG-2

During the adjustment cycles of RGG-1 and RGG-1S it was learned that the first screw change from "as manufactured" to some reasonable balance level required large movements of large screws. These large changes frequently used all of the screw travel capability; even when some travel remained, fine balance changes could be made only by using fractional turns on heavy screws. To alleviate these problems a tare weight concept was instituted and an attempt was made to optimize the remaining adjustments. These operations are discussed in the following paragraphs.

A. THE TARE WEIGHT CONCEPT

As mentioned above, relatively large mass changes are required to bring the gradiometer from the "as manufactured" condition to some semblance of practical balance. Instead of turning all available screws many turns to bring about these large changes, it was decided to leave all of the screws alone except those in the center plane of the arm masses. Then, instead of turning these screws many turns, their mass was changed by turning off the ends of the screws or replacing them with a different size. This method is quite effective. The required large first moment and second moment changes are accomplished without moving the majority of the screws from their initial center position. After the tare weight changes are made, the trim adjustments can then be made using relatively large numbers of turns on small screws without running out of travel range. The tare weight concept requires a special calculation that is discussed in detail in Appendix D.

B. BALANCE SCREW ADJUSTMENT COMPUTATION

After the RGG vibration sensitivities of the gradiometer have been measured on the vibration stand, the balance changes required are

PRECEDING PAGE BLANK-NOT FILMED

overdetermined. That is, the net balance change required can be made by a number of different screws or combination of screws. If a poor combination is selected it is possible to run out of screw travel before the best possible balance is attained. A special computation method has been devised to overcome this problem and it is discussed in detail in Appendix C.

C. ADJUSTMENT TRIAL RESULTS

When the gradiometer is in the "as manufactured" condition the estimated scale factor may be in error by quite a large factor. Therefore the first measurement of the sensor vibration sensitivities and subsequent adjustment is actually a scale factor calibration. Table 7-1 shows the balance sequence trials for RGG-2. It can be seen in this table that for the first adjustment the assumed scale factor was in error by a factor of almost exactly 2. The adjustment was in the right direction to reduce the sensitivity coefficient to zero but we overshot by 100%. (This was due to an engineering error since the scale factor is actually known to far better than 100%.) The next step amounted to another tare weight calculation and it was quite successful. In this (12/17/76) column, most attention should be paid to T6, the "sum-mode missmatch". The correction of this coefficient requires large inertia changes of the arms, and small percentage errors in these changes may show up as T1, T2, T3 and T4 errors.

The results of the first real trim of the error coefficients, based on static (non-rotating) vibration tests, are shown in the 12/29/76 column; the results are quite satisfactory. Since time on the contract was running out, and since the coefficients may change when the sensor is rotating, the static balance tests were terminated after the second trim. (Time did not permit dynamic (rotating sensor) error coefficient estimates on RGG-2 under this contract.)

Table 7-1 is given in terms of T1, T2, etc., instead of K1, K2, etc., that are actually used by Hughes for screw turn calculations. The "T's" refer to tensor element value and the goals are shown in

Table 7-1. RGG-2 Static Balance Adjustment Sequence

	As Fab. 12/9/76	S. F. Adj 12/15	Tare Adj. 12/17	1st "Real" Trim 12/29	2nd Trim 1/5/77	AFGL Goal *	Factor To Go
T1 EU/G x 10^6	-12	+12	- 5	- 0.05	- 0.0	0.0025	100
T2 EU/G x 10^6	+10	- 8	- 5	- 0.5	+ 0.22		
T3 EU/G x 10^6	-13	-13	-13	-13	-13	0.005	2640
T4 EU-SEC^2 x 10^5	+ 0.25	- 0.4	- 0.02	+ 0.04	+ 0.025	0.00025	100
T5 EU-SEC^2 x 10^5	- 0.95	+ 0.7	- 0.21	+ 0.05	- 0.0075		
T6 EU-SEC^2 x 10^5	+22	-20	- 0.24	+ 0.08	+ 0.0003	0.0005	0

*AFGL Goal: 1 EU - 10 sec integration time environment as stated in Hughes Jan 1975 Report

T2143

terms of the requirements for the hypothesized AFGL environment. Also, the T1 and T2 and T4 and T5 coefficients are grouped, since in a random environment they would not be separately identifiable. It is believed that this terminology will be more useful to the reader than our usual K values.

Table 7-1 lists numbers in a column entitled "factor-to-go" for the T1 through T6 error coefficients. These numbers are based on the coefficient estimates made using the 5 January 1977 test data (after the second trim of the balance screws). With the exception of T3, the coefficient factors-to-go offer promise that our original AFGL coefficient goals can be met. By contrast, however, the T3 error coefficient, often referred to as the "Yankee Screwdriver Effect", stands out because it is so large. This is not surprising since no attempt had been made on RGG-2 to adjust this error source. We know that 2-ω coaxial vibrations excite this error source and we hypothesize its cause to be a slight twist in the arm support structure. Two possible corrective (adjustment) methods are contemplated. As discussed earlier, we have provided a method of introducing a controlled amount of twist into the pivot structure. Early tests on RGG-1 demonstrated that such a twist can change the magnitude of T3. The second method of control involves an adjuster which becomes an integral component of the sensor. The adjuster concept is known but has yet to be designed. Time was not available under this contract to investigate and demonstrate the effectiveness of either of these solutions.

SECTION 8

DYNAMIC BALANCING OF THE RGG-2 ROTOR

Rotating reaction forces are present at the RGG spin bearings if the rotor is not perfectly balanced. These reaction forces shake the test platform of the laboratory VIALS, are detrimental to bearing performance, and results in motion of the RGG stator that may contaminate test data.

The rotor of the RGG-2 was dynamically balanced on 25 and 26 January 1977 using techniques developed on RGG-1. Each RGG has 16 radial tapped holes in a plane at each end of the rotor as seen at the lower left in Figure 2-9. Beryllium-copper screws in these holes are adjusted to correct unbalance.

The setup for dynamic balance is to suspend the RGG on four long rods so that the only significant resistance to horizontal motion of the RGG stator is the inertia of RGG and the suspension brackets. The RGG is suspended with its spin axis horizontal. Two geophones are mounted on the brackets at nodes such that each geophone is sensitive only to the reaction forces introduced into the plane of the balance screws nearest to that geophone. The RGG-2 was mounted so that both balance ports faced 45 degrees down from horizontal and a slight overpressure of dry, filtered air was maintained in the stator to prevent debris from entering the stator when a balance port was removed to make screw adjustments. The rotor is spun at synchronous speeds by the spin motor to obtain unbalance readings on the geophones. The geophone output voltages are demodulated with respect to the master pulse from the PE/LED to provide the angular location of the needed balance correction.

The first measurement on RGG-2 indicated the need for about 7 gram-centimeters of correction in each balance plane, assuming a scale factor of 0.578 gm-cm/millivolt based on experience with RGG-1. The angular orientation found on RGG-1 was assumed and found to be correct within one degree. The correction made was to remove a

No. 8-32 beryllium cooper set screw 0.375 in. long from each balancing plane and to bottom the 0.25 in. long screws that were previously used to lock the 0.375 in. screws in mid travel.

The sequence of corrections is indicated in Table 2-6. Test results from the first correction provided revised scale factors for the geophones. The first correction provided balance improvement by a factor of better than six. The second correction utilizing the new scale factors, improved the top balancing plane by a factor of eight and the bottom by a factor of 32. The bottom plane was then out of balance by only 0.04 gm/cm and was into the noise level of the instrumentation such that the phasing (angular location of the unbalance) could not be determined.

One last correction was attempted in the top balancing plane. It involved 1.00 turn of one screw and 0.38 turn of another. This correction could not be verified because the bearings were low on oil as indicated by the spin motor excitation. Operation of the RGG-2 on the Laboratory VIALS subsequent to refilling the bearings showed that table motion due to rotor unbalance was undetectable.

Table 8-1. [illegible] Balance Corrections on RGG-2

First Iteration	Top (+Z) Plane	Bottom (-Z) Plane
Initial:		
Geophone output, millivolts	12.68	12.35
angle	-75°	-92°
Scale factor used, gm cm/mv	0.578	0.578
Indicated unbalance, gm cm	7.33	7.14
After correction:		
Geophone output, millivolts	1.99	1.91
angle	-74°	-35°
<u>Second Iteration</u>		
Initial (Geophone as above)		
Scale factor used, gm cm/mv	0.679	0.639
Indicated unbalance, gm cm	1.351	1.220
After correction:		
Geophone output, millivolts	0.24	0.06
angle	-25°	$\pm 1^{\circ}$
Indicated unbalance, gm cm	0.163	0.038

T2144

SECTION 9

RGG-2 TEST DATA SUMMARY

A. RGG-2 ORIENTATION TEST

1. Test Description

Orientation testing of the RGG is used to determine stator-fixed bias and to estimate g and g^2 sensitivities of the instrument. The tests are conducted by positioning the RGG stator at various angular orientations relative to an axis fixed in the earth's gravity field. After each orientation change, the instrument is allowed to stabilize, and the total signal output of each RGG channel is recorded as a function of orientation angle. The data samples are taken at equal and integral orientation angle increments for a complete spatial revolution of the stator, and the resulting samples are processed to determine the spatial fourier coefficients of the output function. The significance of these coefficients depends on the specific test conditions, and the preliminary tests on RGG-2 were restricted to the following three specific conditions:

- Spin axis vertical (SAV) with stator orientation increments of 45° about the spin axis.
- Spin axis horizontal (SAH) with stator orientation increments of 45° about the spin axis.
- Spin axis tumble (SAT) at 15° orientation increments in a fixed vertical plane normal to the RGG stator transverse reference axis ($\bar{x}$).

The first two tests were used to estimate case-fixed biases, and the last test was used to estimate g and g^2 sensitivities.

2. Test Results

The data for all tests was fitted to a five-parameter Fourier function of the following form:

$$G = a_o + a_1 \cos \gamma + b_1 \sin \gamma + a_2 \cos 2\gamma + b_2 \sin 2\gamma \qquad (1)$$

PRECEDING PAGE BLANK-NOT FILMED

In each case, the quality of the function fit is evaluated by the bias and standard deviation of the fitting error. The quality of the data is judged on the basis of its standard deviation, and the significance of each coefficient estimate is determined by its size relative to the curve fitting and data error measures.

The standard deviation of the data from the spin axis vertical orientation test is negligible (1.2 EU), and the principal gradient channel fitting errors are +1.7 EU Bias and 5.3 EU STD DEV. The cross-gradient channel fitting errors are +0.03 EU Bias and 16.7 EU STD. DEV. The significant coefficient estimates from this test are as follows:

Principal Gradient Channel Bias	+27 EU
Second Harmonic Amplitude	750 EU

The second harmonic amplitude is due to the local gravity field and to the magnetic field sensitivity of the sensor. These influences have not been separated.

The standard deviation of the data from the Spin Axis Horizontal Orientation test is approximately 44 EU, and the curve fitting errors have less than 0.1 EU Bias. The standard deviation of the curve fitting errors are 287 EU and 172 EU for the principal and cross-gradient channels, respectively. The bias coefficient estimates for both channels are within the curve fitting errors, i.e., less than 150 EU. The second harmonic amplitude was approximately 36,000 EU. This amplitude is the result of the g^2- sensitivity of RGG-2, its magnetic sensitivity, and the local gravity gradient field. It is estimated that the uncompensated g^2 sensitivity is contributing approximately 33,000 EU, that the magnetic sensitivity is contributing approximately 750 EU and that the local gravity field is contributing approximately 2250 EU.

3. Summary and Conclusions

The preliminary orientation tests on RGG-2 met the objectives of providing stator-fixed bias estimates and of providing estimates of the g^2 sensitivity of the instrument. The stator-fixed bias estimates

for each RGG channel in both spin axis orientations are presented in Table 9-1.

Table 9-1. Stator-Fixed Bias Estimates

RGG Spin Axis Orientation	Principal Gradient Bias	Cross Gradient Bias
Vertical	+ 26.9 EU	- 2.2 EU
Horizontal	-154.0 EU	-130.7 EU

T2145

Estimates of g^2 sensitivity were made from both the SAH orientation test and from the spin-axis tumble test (SAT). In both cases, the sensor output data was corrected on the basis of an assumed local gravity field. The g^2 sensitivity estimates are in close agreement as indicated by Table 9-2.

No significant "g" sensitivity could be observed from these tests.

Table 9-2. g^2 Sensitivity Estimates

RGG-Test	g^2 Sensitivity
SAH	+33,284 EU/g^2
SAT	+33,387 EU/g^2

T2146

Although a few preliminary test runs had been made on RGG-2 in December, the first significant tests were started on Monday, 10 Jan 1977. At that time, the spin bearings had been filled and run in, the sensor temperature had stabilized, and a good internal vacuum had been attained. The sensor was mounted on the vibration isolation test stand for all of the tests discussed in the following paragraphs. The

arms of the sensor had been balanced by the static balance procedures discussed in a previous section, but no rotating balance adjustments had been made. In addition, the sensor rotor, as a whole, had not been dynamically balanced; this unbalance was sufficiently large that it caused the whole test mount to vibrate at a significant level.

In this poorly trimmed and unadjusted condition the test results discussed in the following paragraphs were obtained during the week of 10 Jan 1977.

B. SPIN AXIS VERTICAL: TRANSIENT RESPONSE AND 5 HOUR RUN

One of the most impressive gradiometer demonstrations is to show its time response to a proximate mass. Figure 9-1 shows the transient response of RGG-2 to a 35-kg, short, stubby, lead mass cylinder. A highly simplified estimate of the gradient due to this mass at 0.3 meters is

$$GP = \frac{(GYY - GXX)}{2} = \frac{3}{2}\frac{GM}{R^3}$$

$$= 151 \text{ EU}$$

This calculation neglects the size effect of both the mass and the gradiometer. It assumes that the gradiometer is a point and the mass is a point; both assumptions are obviously untrue. Nevertheless, the computer printout indicates a delta gravity gradient change of 130 EU for this particular test. The computer evaluated the sensor signal noise as being approximately 1.0 EU during the nontransient periods of this test. Since the sensor was quite stable during this demonstration it was also possible to record the presence of personnel standing in the vicinity of the gradiometer. Although these latter records are impressive, they have no technical value and are not reproduced.

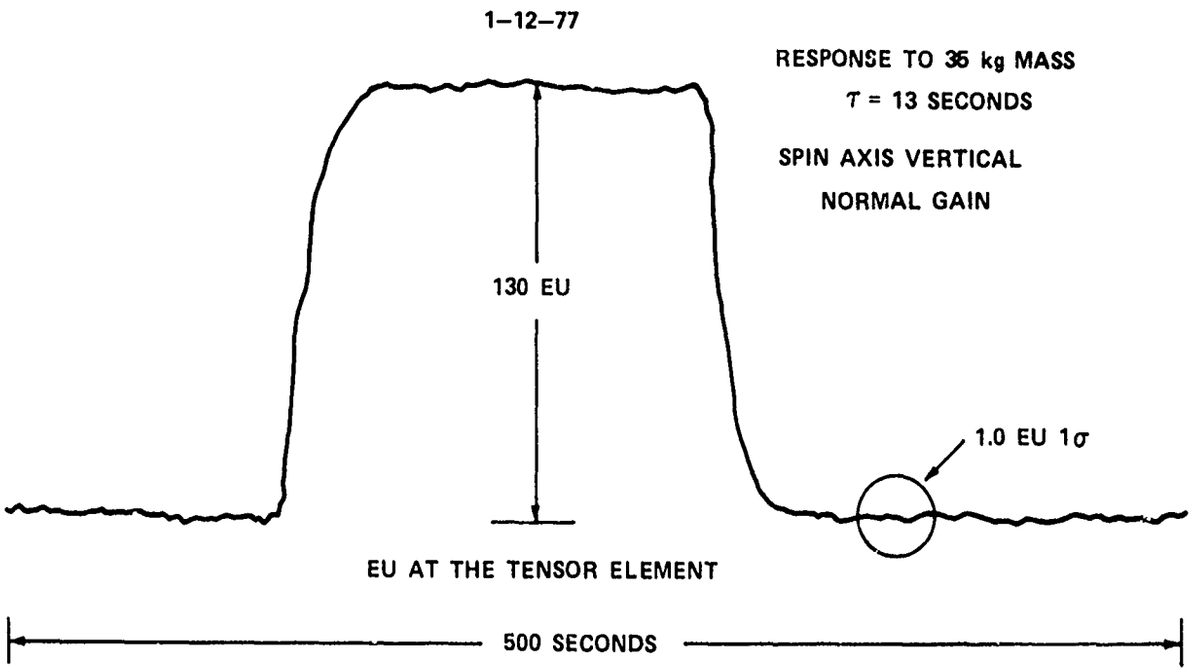

Figure 9-1. RGG-2 transient response plot to a 35 kG mass at 0.3 m. Spin axis vertical.

It should be noted that the analog channel used to generate these time response curves is a monitor and display channel only. It is not an instrumentation grade channel and is not used for data taking purposes. All RGG data is derived from the computer printout.

While RGG-2 was in the spin axis vertical attitude and mounted on the vibration isolation system, a 5-hour run was made. In addition to the conventional printout, a paper tape was punched with the same data. This tape was then loaded into an off-line computer and each data point plotted on a graph as shown in Figure 9-2 for the principal gradient tensor term and in Figure 9-3 for the cross gradient tensor term. The ordinates for these two plots are in EU and the abscissa is the count of the data points - one every 10 seconds.

Considering the trim and adjustment level of RGG-2 at that time, the goal of 1.0 EU is shown to be near at hand.

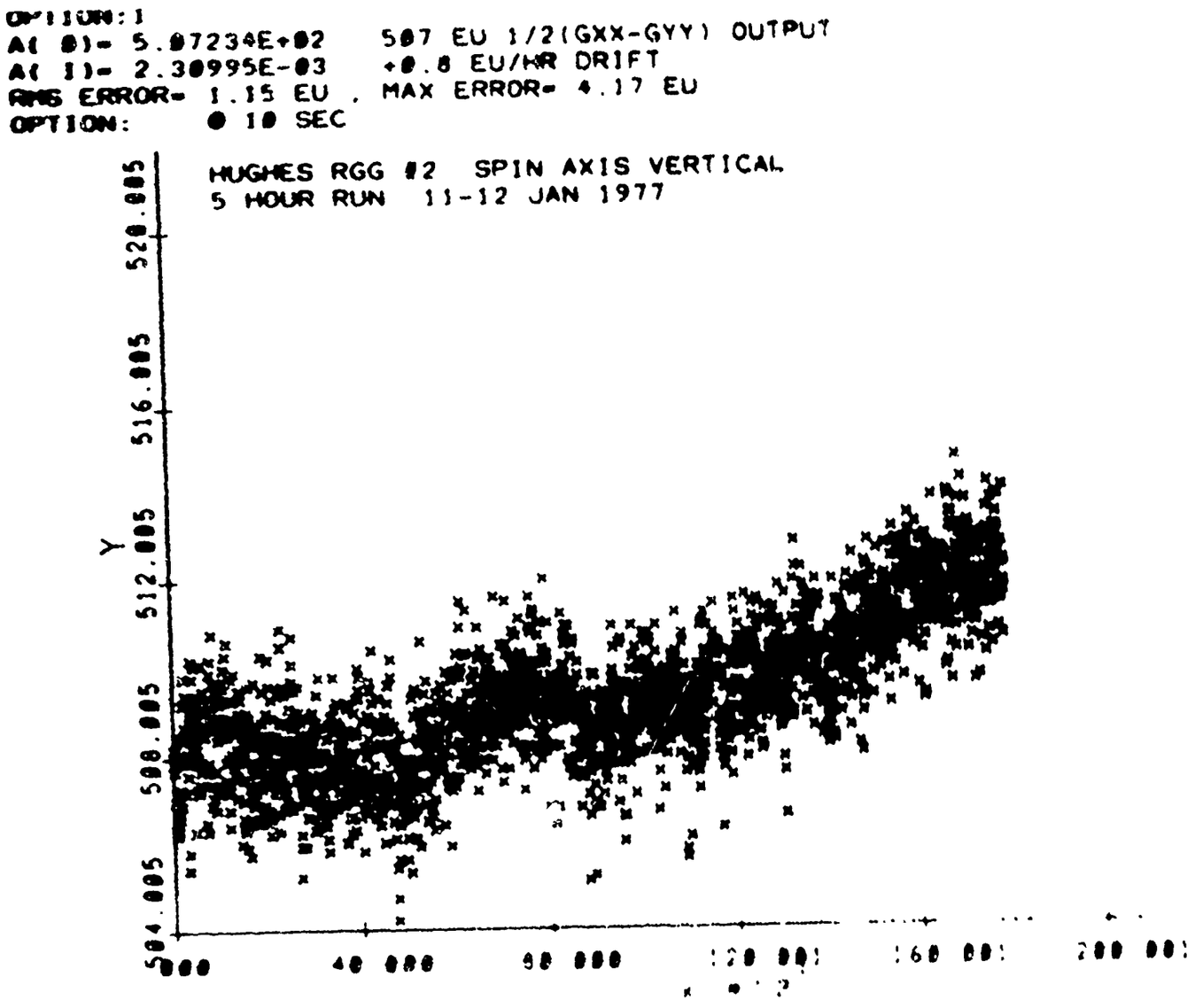

Figure 9-2. Principal gradient noise and trend-spin axis vertical.

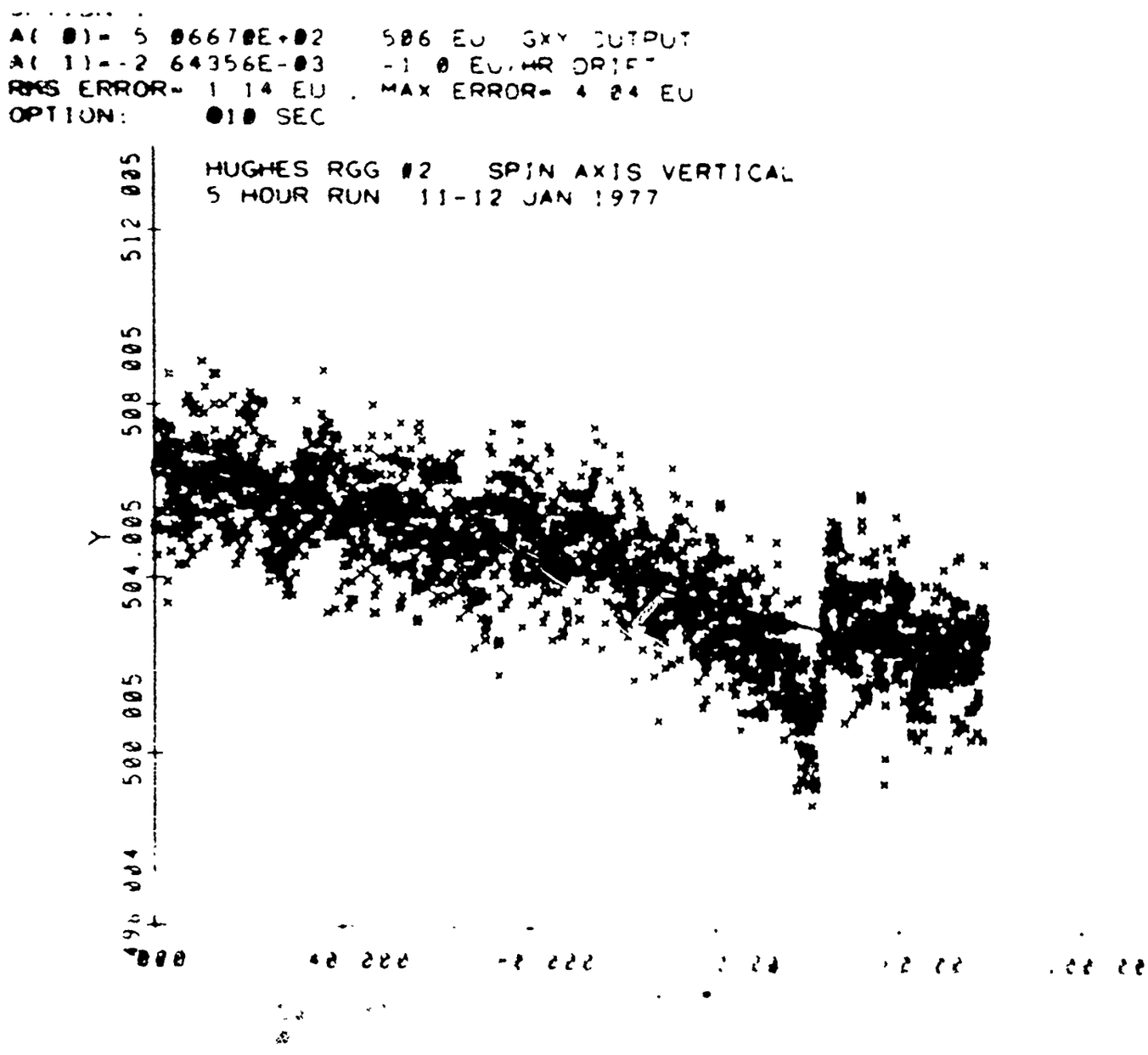

Figure 9-3. Cross gradient noise and trend plot-spin axis vertical.

C. SPIN AXIS HORIZONTAL: TRANSIENT RESPONSE AND 3 HOUR RUN

After the spin axis vertical tests described in the paragraphs above, the sensor was rotated to the spin axis horizontal attitude and allowed to stabilize. The transient response test was then repeated and the resulting graph is shown in Figure 9-4. This figure represents a landmark for the Hughes gravity gradiometer program. It is the first transient response graph with the spin axis horizontal that demonstrates a worthwhile gradiometer capability. This relatively small delta mass signal (119 EU) was detected in the correct channel, riding on top of the 35,590 EU unadjusted anisoelastic bias signal.

In addition to the transient response proximate mass tests, 5-hour and 3-hour stability runs were made (spin axis horizontal). The 5-hour test produced an acceptable drift run. However, a change in the computer speed control servo gain significantly reduced the noise in the signal so a second run was made. The second test was run under computer control from 11:00 PM to 2:00 AM and was limited to 3 hours (due to an operator oversight). The 3-hour run is shown in Figures 9-5 and 9-6.

It will be noted that the drift and noise figures of merit are approximately an order of magnitude larger than similar figures obtained for the vertical spin axis orientation. These results, although short of the goal are surprisingly good considering the state of sensor grooming at the time the tests were made. It is expected that superior results will be obtained with RGG-2 where: 1) the anisoelastic coefficient is adjusted; 2) the arms are balanced to the proper level; 3) the sum mode coupling coefficient is minimized for horizontal spin axis operation, and 4) the rotor has been dynamically balanced.

D. ANGULAR RATE SCALE FACTOR TESTS

As has been stated many times, no gravity gradiometer can distinguish between a gravity gradient and the square of an angular rate input. After RGG-2 had demonstrated a long-time stability and a noise

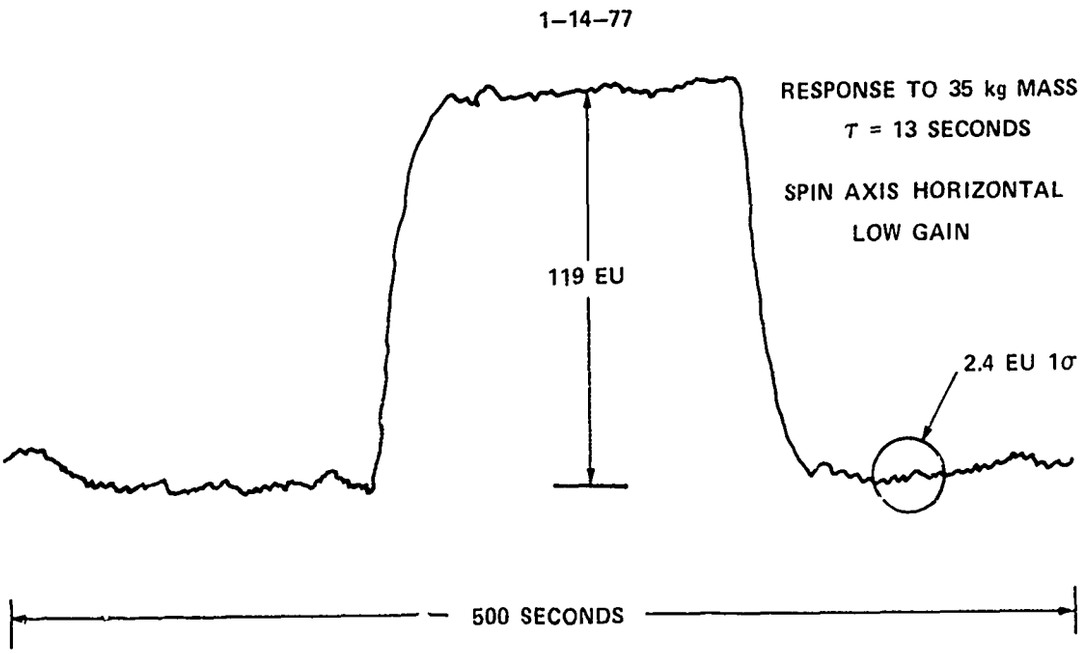

Figure 9-4. RGG No. 2 transient response to moving mass plot—spin axis horizontal.

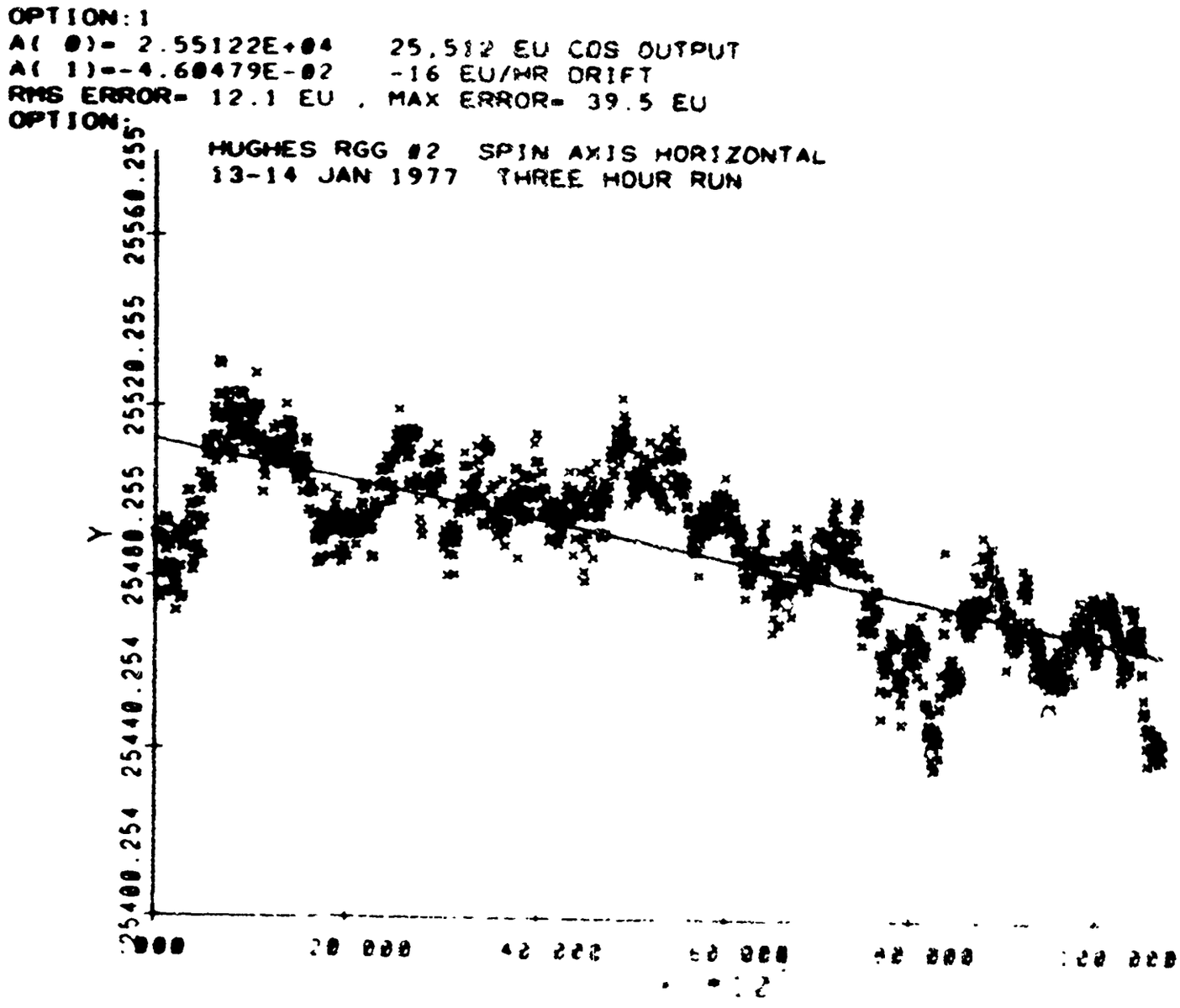

Figure 9-5. RGG-principal gradient noise and trend plot spin axis horizontal.

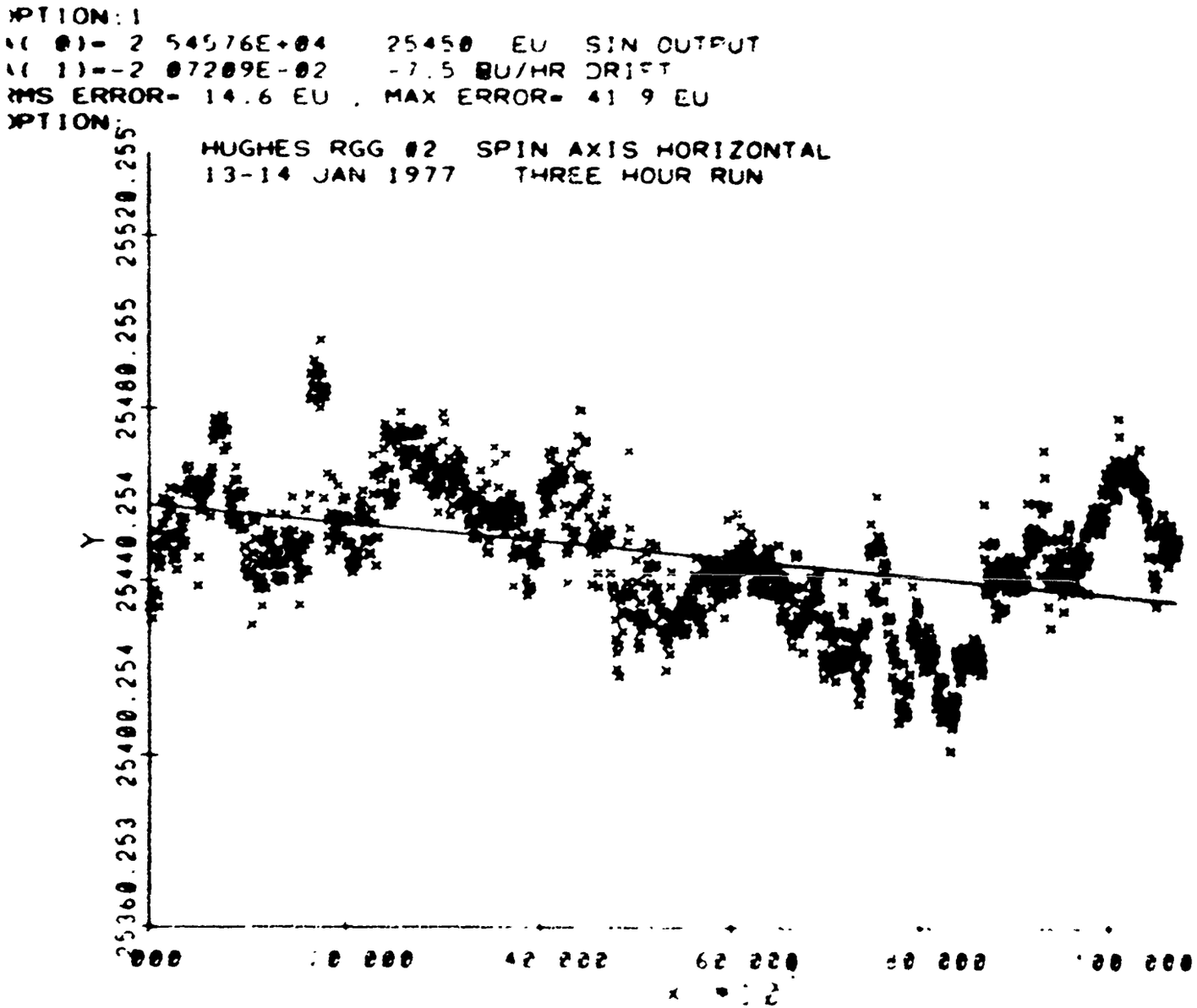

Figure 9-6. RGG No. 2 cross gradient noise and trend plot spin axis horizontal.

of less than 10 EU per channel with the spin axis horizontal, a test was made on 1/14/77 to measure this angular rate sensitivity.

With the gradiometer spin axis horizontal, the vibration test stand was oscillated about its vertical axis at a peak rate of 7.88 x 10^{-4} rad/sec squared at 20 Hz, a frequency not harmonically related to the spin speed. The data were taken in the following sequence:

- Apply angular rate
- Allow 2-minute stabilization time
- Take 1-minute data average
- Remove angular rate
- Allow 2-minute stabilization time
- Take 1-minute data average
- Repeat above 12 times

The delta outputs were averaged (with due regard for sign changes) and the average output signal was

$$GP = 176.15 \text{ EU} ; GC = 0.3 \text{ EU}$$

The theoretical output signal for our scaling is

$$GP = \frac{\omega^2}{4} \times 10^9 = 155.3 \text{ EU}$$

This 13.4% scale factor discrepancy remains to be investigated.

E. WINDAGE TESTS

Due to the open rotor structure of RGG-1 and RGG-1S, whenever the pressure in the sensor changed a few tens of microns, the arms windmilling in this new atmosphere caused a significant change in the

output signal. RGG-2 was designed so that the outer rotor is nearly enclosed, except for a few small holes at the ends, to reduce this windage effect.

At the time that we attempted to make windage effect measurements on RGG-2, the spin bearings were operating erratically and critical tests were impossible. However, it was possible to determine that the windage effect for RGG-2 was less than 1/20 that of RGG-1 or RGG-1S and is probably even better than that. In fact, RGG-2 was operated with the internal pressure equal to one-half atmospheric pressure and the signal changed by only 1000 EU. This is a dramatic change from RGG-1 which changed by tens of thousands of EU when the internal pressure was allowed to increase to one thousand microns. Thus, we conclude that the excessive internal pressure sensitivity problem of RGG-1 has been corrected in RGG-2.

APPENDIX A

WINDAGE EFFECTS ON ROTATING GRAVITY GRADIOMETER AT LOW PRESSURE

SUMMARY

Calculations have been made of the windage torque on the rotor of the rotating gravity gradiometer at 17.76 rps in air at approximately 120F at pressures of 10^{-1} and 10^{-5} torr. Neglecting end and cutout effects the torques are 4.3×10^{-3} and 1.03×10^{-6} in.-lbf at the higher and lower pressures, respectively. Heat transfer between air and rotor or stator surfaces is 3.6×10^{-3} Btu/ft^2 sec and less. Flow and geometric parameters indicate no torque fluctuations from Taylor vortex instabilities.

CONDITIONS

Calculations of windage effects on the rotor of the rotating gravity gradiometer (RGG) have been extended to the following conditions in air:

Pressures	10^{-1} to 10^{-5} torr (0.2785 to 2.785×10^{-5} psf)
Temperatures	110F to 130 F (570° to 590°R)

Referring to the cylindrical flow geometry shown in Figure A-1, $\omega = 17.76$ rps, $d_1 = 2r = 6.562$ in., $d_2 = 2r_2 = 6.687$ in., $L = 6.574$ in. Effects of cylinder ends and surface cutouts have been omitted.

WINDAGE TORQUE

The degree of gas rarefaction is measured by the Knudsen number

$$K_n = \frac{\lambda}{r_2 - r_1} \quad . \tag{1}$$

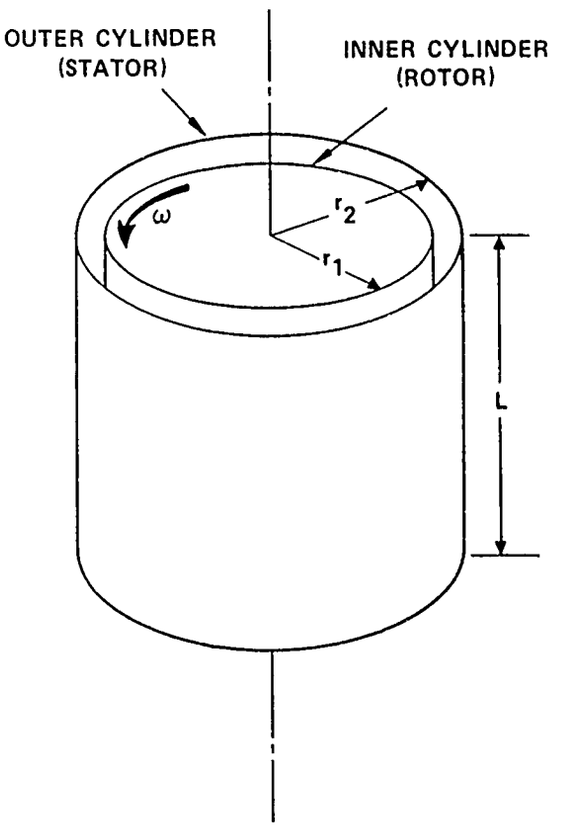

Figure A-1. Cylindrical flow geometry

where the mean free path λ is computed from the kinetic theory relation

$$\lambda, \text{cm} = 5.09 \times 10^{-2} \left[\frac{T, K}{298}\right] \left[\frac{10^{-1}}{p, \text{torr}}\right] \tag{2}$$

Under the above conditions, eqs. (1) and (2) and the following table

	λ, cm//K_n	
p, torr	110 F	130 F
10^{-1}	0.054//0.34	0.056//0.352
10^{-5}	540//3400	560//3520

show that the flow between cylinders is free-molecular ($K_n \geq 10$ approximately) at the lower pressure and transitional (between slip flow and free-molecular) at the higher pressure. Variation due to temperature is negligible, so an average temperature T = 120F can be used hereafter within the accuracy of these estimates. Thus, the Mach number M at the rotor periphery is

$$M = \frac{\omega r_1}{\sqrt{\gamma R T}} = \frac{17.76 \frac{\text{rev}}{\text{sec}} \times 2\pi \frac{\text{rad}}{\text{rev}} \times \frac{3.281 \text{ in}}{12 \text{ in/ft}}}{\sqrt{1.4 \times 1716 \frac{\text{ft}^2}{\text{sec}^2 \text{ R}} \times 580 \text{ R}}} = 0.0258 \tag{3}$$

A number of studies (References 1 through 6, for example) consider this rarefied Couette flow problem. The essential requirement for solution in the region between slip and free molecular flow is that approximations to the collision integral or velocity distribution function be made in the governing Boltzmann equation, which replaces the Navier-Stokes equation for continuum flows. It is usually assumed (as guided by experiments) that molecules reflect diffusely after

impingement on typical smooth metallic surfaces, and that tangential and normal momentum accommodation coefficients are near unity. It was assumed in using the equations of References 1 and 3 that the (constant) surface temperatures of rotor and stator were equal. Furthermore, in Reference 3 equations, Prandtl number = 0.715 was assumed. In all cases specific heat ratio γ of 1.4 for air was used.

The torque M_o on the rotor is obtained from surface shear stress τ by the relation

$$M_o = 2\pi r_1^2 L\tau \tag{4}$$

Some of the references present frictional drag coefficient C_d or C_f, from which the torque can be obtained using the definition

$$C_f = \frac{\tau}{q} = \frac{\tau}{\frac{1}{2}\rho[\omega r_1]^2} = \frac{\tau}{\frac{\gamma}{2} p M^2} \tag{5}$$

where ρ and p are density and pressure, respectively.

The solutions for rotor torque of References 1, 2, 3, 5, and 6 are plotted in Figure A-2 as a function of Knudsen number, with the two specified pressure levels marked. Although different series expansions in high or low K_n were used, all theories produce a reasonably consistent curve. In Reference 2 only graphical results are available, allowing the single point comparison. The second-order expansion equations of Reference 3 (for low K_n) are quite lengthy to compute, but the values shown at $K_n = 0.34$ would probably agree even better with the curve if higher-order terms were available. From Figure A-1 it appears that torques of about 4.3×10^{-3} in. lbf and 1.03×10^{-6} in. lbf correspond to pressures of 10^{-1} torr and 10^{-5} torr, respectively. Experiments indicate reasonable good agreement with a theoretical C_dM curve for air and argon.

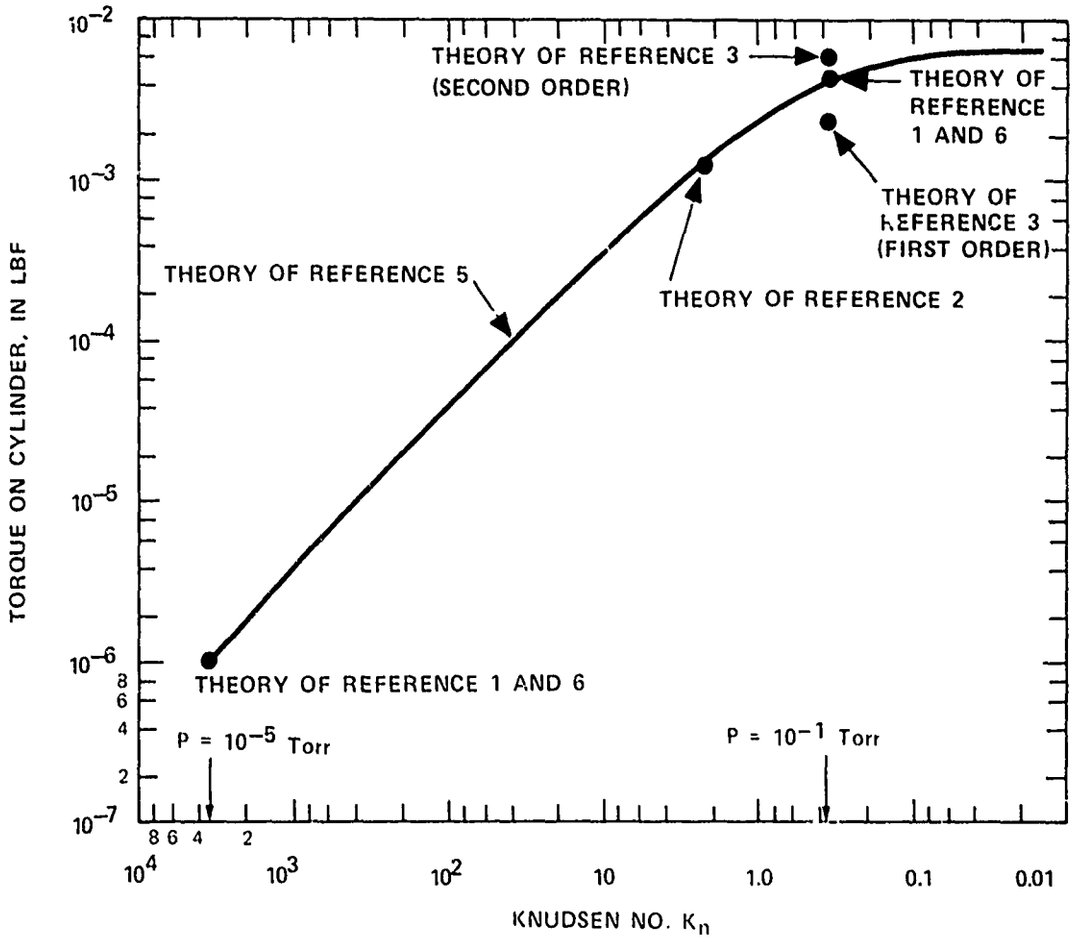

Figure A-2. Torque on rotor in air at low pressure.

The entire cylindrical surface area of the rotor was used in eq (4). A rough approximation to the effect of cutouts on torque would be to reduce the shear area by the amount of total cutout area. More rigorous analysis is not presently considered. It should be noted that for solid concentric cylinders, Taylor vortex instability and torque fluctuations have been found when the Taylor number

$$T = \frac{\rho \omega r_1 [r_2 - r_1]}{\mu} \sqrt{\frac{r_2 - r_1}{r_1}} \geq 41.3 \tag{6}$$

In the present case,

$$T = 0.0219 \frac{p}{\mu R T} \tag{7}$$

where μ = absolute viscosity = 4×10^{-7} slug/ft sec

$$R = \text{gas constant} = 1716 \frac{ft^2}{sec^2 \; R} \text{ for air}$$

Hence the Taylor number T = 0.0153 for p = 10^{-1} Torr (0.278 psf), is far below the instability level, and would be still lower at the lower pressure. Therefore, it can be concluded that such flow instability should not occur.

HEAT TRANSFER

It was found, from the heat transfer equations to first order in Reference 3, that heat transfer rates from the air to either rotor or stator were approximately 10^{-5} Btu/ft^{2}sec. For the case when the rotor was at 120F and the stator at 110F, the simplified flat-plate Couette flow model reported in Reference 6 was used to estimate heat transfer rate. Heat transfer rate versus Knudsen number thus computed

is shown in Figure A-3. The rate is proportional to the temperature difference (ΔT, R) between the surfaces in relative motion. At the higher specified pressure of 0.1 Torr, $q = 3.6 \times 10^{-3}$ Btu/ft^{2}sec. At the lower pressure of 10^{-5} Torr $9 = 5.7 \times 10^{-7}$ Btu/ft^{2}sec.

For future calculations of either torque or heat transfer variation with Knudsen number (i.e., pressure and temperature) it is suggested that the pertinent equations of Reference 3 be programmed to obviate lengthy, tedious hand calculations.

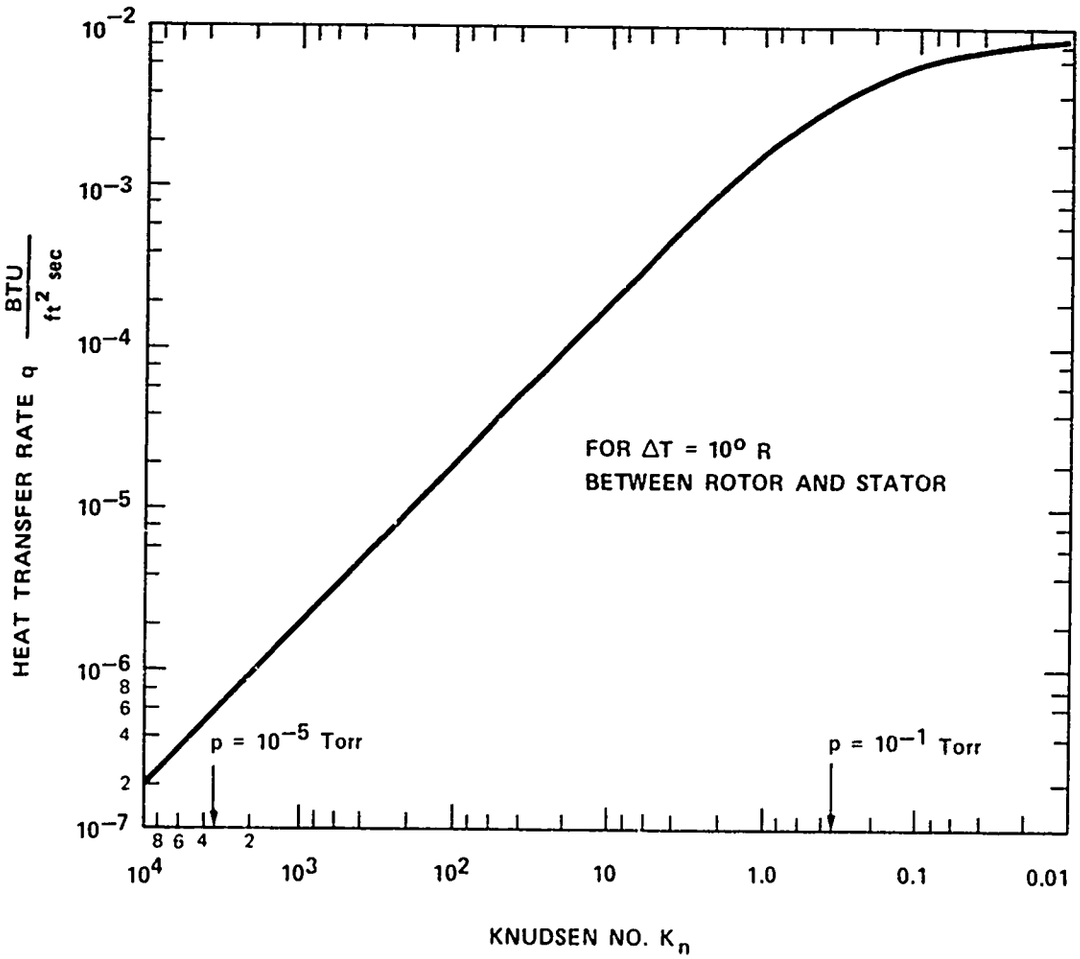

A-3. Heat transfer rate between rotor and air at low pressure.

REFERENCES

1. V. P. Shidlovskiy, Introduction to Dynamics of Rarefied Gases, (American Elsevier Publishing Co., N. Y., 1967).

2. S. F. Shen, "A General Transfer-Equation Approach for the Transition Regime of Rarefied-Gas Flows and Some of Its Applications." Rarefied-Gas Dynamics, Advances in Applied Mechanics, Suppl. 2, Vol. 2, Academic Press, pp. 112-131 (1963).

3. T. C. Lin, R. E. Street, "Effect of Variable Viscosity and Thermal Conductivity on High-Speed Slip Flow Between Concentric Cylinders," NACA Rept. 1175, (1954).

4. D. R. Willis, "Heat Transfer and Shear Between Coaxial Cylinders For Large Knudsen Numbers," Physics of Fluids, 8, pp. 1908-1910 (1965).

5. C. Cercignani, F. Sernagiotto, "Cylindrical Couette Flow of a Rarefied Gas," Physics of Fluids, Vol. 10. No. 6, pp. 1200-1204 (1967). (Comments on pages 1858-1860 by A. S. Berman and author's reply.)

6. S. A. Schaaf, P. L. Chambre, Flow of Rarefied Gases, (Princeton Aeronautical Paperbacks No. 8, Princeton University Press, 1961,) pp. 35-38.

PRECEDING PAGE BLANK-NOT FILMED

APPENDIX B

RGG-2 DATA PRINTOUT DESCRIPTION AND FORMAT

Figure B-1 shows an RGG-2 data heading printout and data record. The various features are discussed in the following paragraphs. The recorded environmental data will be interleaved with this data.

```
RGG-2
 1,14,77    9:36  TNO  1 BIAS  -70.2000      0.0      0.0     0.0000
M1-MS=  59.  59.  55.  65.  73.  76. 100.  67.
ARM1 0.5029 0.7368   ARM2 0.5208 0.5087   TU-FAC   13680.
LAST BAL  4,10,76   10:28.  SPEED  575792.00 0.01  2W =  34.7348
SERVO  0.004  0.800  GAIN    21.13439   FAC   0.0643500
S.L.  1000 0010 1000 0000  GP=0.5*(GYY-GXX)  GC=GXY

COND        GP         GC        MAG       PHA    FM-CAR     OCT.ERR

2W AVE

2W245   35592.1   -4780.3   35911.6   -7.65  219615.9       0
2W245   35595.6   -4779.3   35915.0   -7.65  219609.1       0
2W245   35599.6   -4778.6   35918.8   -7.65  219625.3      -1
2W245   35604.0   -4786.0   35924.2   -7.66  219624.5       0
2W245   35600.7   -4785.6   35920.9   -7.66  219615.3       0
2W245   35597.8   -4779.0   35917.2   -7.65  219616.3       0
2W245   35590.9   -4774.4   35909.7   -7.64  219625.8       0
2W245   35594.2   -4776.4   35913.3   -7.64  219632.3       0

 2W AVE   8=N    35596.9=P   -4780.0=C     4.19=SP    3.81=SC
                35916.3=MAG    5.66=SMAG          -7.6479=PHA

    DELTA FROM LAST AVERAGE
     126.0=P        9.2=C     126.3=MAG    4.1940=PHA
```

Figure B-1. RGG-2 Heading and Sample Data Printout

RGG-2 Identifies the sensor being tested.

1,14,77 9:36 Month, day, year, and time of test. This flag will also be printed every half hour during the data printout periods.

TNO 1 Test number

BIAS -70.200 0.0 0.0 0.0000

The first and fourth terms are data rotation angles in degrees. They are always added together arithmetically in the computer. During testing, the

PRECEDING PAGE BLANK-NOT FILMED

fourth term will be determined by the characteristics of the sensor itself and the internal electronics. It is not expected that it will be changed during the course of the test. The first term is used to correct for the phase of an excitation signal such as a vibration. The second and third terms can be used to remove constant components from the printout. In the example shown, if the operator types;

BIA -70.2 35596.9 -4780.0

only the differences between the sensor signals and these constant terms will be printed.

M1-M8 = 59. 59. 55. 65. 73. 76. 100. 67.

These are the encoder disc slot corrections. They are times in 1/10 microsecond increments and each unit count represents about 2.4 arcseconds.

ARM1 0.5029 0.7368 ARM2 0.5208 0.5087 TU-FAC 13680.
LAST BAL 4,10,76 10:28

These items applied to the use of the mercury micro-balance tubes (currently not being used).

SPEED 575792 0.01

The first number determines the 10 megahertz counts per revolution 10,000,000/575792 = 1 = 17.3674 RPS. The second determines the percent overspeed allowed before computer shut down.

SERVO 0.004 0.800

These are the computer multipliers for the digital Gravity Gradient Instrument (GGI) Sensor rotor speed control servo before digital to analog conversion.

GAIN 21.13439

This is the ratio of the sensor normal gain amplifier to the low gain amplifier.

FAC 0.0643500

This is the factor that relates the delta FM signal plus zero crossing per octant of the encoder disc to the EU printed out in the GP and GC columns.

S. L. 1000 0010 1000 0000.

This shows the state of the GGI Sensor and computer logic at the time of printout. Table B-1 explains the functions of the various bits. The S. L. can be changed during the course of a text and the new states are always printed out when a change is made.

GP = 0.5*(GYY - GXX) GC = GXY

This heading item merely defines the gravity gradient tensor terms that Hughes will be printing in the data columns. The data print-outs are in EU units (10^{-9} sec^{-2}). X and Y refer to the GGI Sensor stator coordinates.

COND GP GC MAG PHA MG-CAR OCT. ERR

These are the column headings for the GGI data printouts.

COND shows that the 2W signal is being printed and the 245 shows that the data is being averaged in a 245 revolution (14 sec) moving window.

GP and GC columns are the principal and cross terms of the gradient tensor as shown above.

MAG is the root-sum-square of GP and GC. This is printed merely as a convenience.

PHA is the phase of the MAG term in degrees calculated from arctan (GC/GP).

FM-CAR is the average carrier frequency in Hertz

of the frequency modulated GGI Sensor output signal. This is a monitor function only.

OCT. ERR is a sample-data print-out of the 10 megahertz count error in the zero octant at the instant of print-out. This is a speed control monitor function only.

2W AVE — Signals the operator that the computer sense switches have been set so that the computer will start accumulating the average of the GP and GC columns. Print outs occur every 10 seconds (175 sensor rotor revolutions) for AFGL data and every 20 seconds (350 sensor rotor revolutions) for SSM data. The print out period is selected by setting a computer sense switch.

2W AVE 8 = N

At the end of the data averaging period this print out shows the number of lines of data in the average.

35596.9 = P and -4780.0 = C

These are the N data point averages - in EU - of the GP and GC columns respectively. The computer is programmed to always store the last calculated averages of GP and GC.

4.19 = SP and 3.81 = SC

These are the biased estimates (use N instead of N-1 in the calculation) of the standard deviation about the averages (means) of GP and GC respectively.

35916.3 = MAG and 5.66 = SMAG

These are the root-sum-squares of the P and C, and SP and SC respectively.

-7.6479 = PHA

Is the average phase of MAG in degrees with 5 significant figures.

DELTA FROM LAST AVERAGE

This is a print out option that is selectable by the use of an S. L. switch as explained in Table B-1. This is saves time and possible errors when measuring the delta signal change caused by external influences such as magnetic fields, proximate mass or vibration.

Table B-1 lists the sensor logic (S. L.) states for the GGI Sensor (RGG-2) and the computer. Logic states are changed by setting the desired S. L. switches ON (or OFF) and pushing the SET button on the GGI Sensor RF power supply. Logic states can be set singly or in appropriate combinations.

Table B-1. GGI Logic States

S. L. STATE	
CLEAR	*Normal gain filtered sensor signal
10	*Low gain filtered sensor signal
9+10	*Unfiltered sensor signal
1+9+10+5+CD	Monitor unregulated DC supply for sensor internal electronics
2+9+10+5+CD	Monitor regulated DC supply for sensor internal electronics
1+2+9+10+5+CD	Monitor internal temperature of GGI Sensor
* 4+CD	Applies an internal differential torque to the GGI Sensor arms. Can be applied during any of the modes above.

T2147

Table B-1. GGI Logic States (Continued)

* 5+CD	Injects a square wave test signal to the input of the GGI Sensor internal electronics. Can be applied during any of the modes * above.
6	Calculates delta from the last average of any of the modes above
3	Start computer, any of above modes at TIM #3 in minutes based on a 24 hour clock. Stop computer at TIM #4 in minutes based on a 24 hour clock.

T2147

APPENDIX C

VIBRATION TESTING OF THE NON-SPINNING RGG FOR COEFFICIENT ESTIMATION AND COMPENSATION

INTRODUCTION

Non-spinning tests of the RGG inner-rotor were developed and implemented early in the construction and assembly processes of RGG-1. The purpose of these tests was to make preliminary error coefficient estimates in order to determine the initial arm mass balancing requirements. Because of the uncontrolled environment, these tests were relatively crude, and all of the more precise balancing adjustments had to be based on spinning tests.

During the past year, significant improvements have been made in non-spinning test technology. It is anticipated that all of the coarse balance screw adjustments can be made on the basis of non-spinning test data and that it may be possible to make the fine balance screw adjustments from the non-spinning data as well.

The improvement of the non-spinning test technology is the direct result of the ability to conduct these tests in the controlled environment of the stator. Under these conditions, the RGG arms are shielded from ambient air currents, temperature stability is maintained, and the rotor angular orientation can be set precisely for each test condition. As a result, significant improvements in test repeatability have been achieved, and error coefficient separation on the basis of the angular harmonics of rotor position has been made possible.

The purpose of this appendix is to describe the new non-spinning test concepts and to present the error coefficient estimation equations associated with these concepts. An additional purpose is to present a set of adjustment influence equations for RGG-2.

NON-SPINNING TEST CONCEPTS

The non-spinning test concepts of the RGG are based on the ability to estimate differential mode input torque changes from the observed output signal changes which result from linear or angular

vibration inputs to the RGG stator at the differential mode resonant frequency. This is achieved by employing the excitation frequency in the RGG signal detection process and by using a priori knowledge of the signal process transfer functions. Under these conditions, the linearized and normalized differential mode torque is related to the input vibration functions by (1).

$$\begin{aligned} \epsilon \triangleq & \left[K_1 - 2K_7C_{jg} + 2K_8C_{ig} + K_{10}C_{kg}\right]n_i \\ & + \left[K_2 - 2K_7C_{ig} - 2K_8C_{jg} - K_9C_{kg}\right]n_j \\ & + \left[K_3 - K_9C_{jg} + K_{10}C_{ig}\right]n_k \\ & + K_4\dot{\omega}_i + K_5\dot{\omega}_j + K_6\dot{\omega}_k \end{aligned} \tag{1}$$

The C_{ig}, C_{jg}, and C_{kg} are the direction cosines of the gravity vector in the rotor reference frame $(\overline{ijk})$.

To illustrate the concept of error coefficient separation on the basis of the angular harmonics of rotor position, it is convenient to expand (1) in stator coordinates $(\overline{xyz})$ as a function of the relative rotor angular position (α). A general form of the expansion of (1) is presented as (2), and the coefficients of (2) are defined by (3) through (7).

$$\epsilon \triangleq A_0 + A_1 \cos\alpha + B_1 \sin\alpha + A_2 \cos 2\alpha + B_2 \sin 2\alpha \tag{2}$$

$$A_0 \triangleq K_3n_z + K_6\dot{\omega}_z \tag{3}$$

$$\begin{aligned} A_1 = & K_1n_x + K_2n_y + K_4\dot{\omega}_x + K_5\dot{\omega}_y - K_9\left[C_{zg}n_y + C_{yg}n_z\right] \\ & + K_{10}\left[C_{zg}n_x + C_{xg}n_z\right] \end{aligned} \tag{4}$$

$$B_1 = K_1 n_y - K_2 n_x + K_4 \dot{\omega}_y - K_5 \dot{\omega}_x + K_9 \left[C_{zg} n_x + C_{xg} n_z \right]$$

$$+ K_{10} \left[C_{zg} n_y + C_{yg} n_z \right] \tag{5}$$

$$A_2 = -2K_7 \left[C_{xg} n_y + C_{yg} n_x \right] + 2K_8 \left[C_{xg} n_x - C_{yg} n_y \right] \tag{6}$$

$$B_2 = +2K_7 \left[C_{xg} n_x - C_{yg} n_y \right] + 2K_8 \left[C_{xg} n_y + C_{yg} n_x \right] \tag{7}$$

When the coefficients of (2) are constants, they can be estimated from the following one-cycle averages:

$$A_0 = \frac{1}{2\pi} \int_0^{2\pi} \epsilon \, d\alpha \tag{8}$$

$$A_n = \frac{1}{\pi} \int_0^{2\pi} \epsilon \cos n\alpha \, d\alpha \tag{9}$$

$$B_n = \frac{1}{\pi} \int_0^{2\pi} \epsilon \sin n\alpha \, d\alpha \tag{10}$$

The five coefficients in (2) can be estimated from a set of sampled values of (2) as well. For example, consider a set of eight samples, ϵ_n, taken at the uniform intervals of

$$\alpha_n \triangleq (n - 1) \left(\frac{\pi}{4}\right).$$

These eight samples can be combined to form the following coefficient estimates:

$$\hat{A}_0 = \frac{1}{4}\left[\epsilon_1 + \epsilon_3 + \epsilon_5 + \epsilon_7\right] \tag{11}$$

or

$$\hat{A}_0 = \frac{1}{4}\left[\epsilon_2 + \epsilon_4 + \epsilon_6 + \epsilon_8\right] \tag{12}$$

$$\hat{A}_1 = \frac{1}{2}\left[\epsilon_1 - \epsilon_5\right] \tag{13}$$

or

$$\hat{A}_1 = \frac{1}{2\sqrt{2}}\left[\epsilon_2 - \epsilon_4 - \epsilon_6 + \epsilon_8\right] \tag{14}$$

$$\hat{B}_1 = \frac{1}{2}\left[\epsilon_3 - \epsilon_7\right] \tag{14}$$

or

$$\hat{B}_1 = \frac{1}{2\sqrt{2}}\left[\epsilon_2 + \epsilon_4 - \epsilon_6 - \epsilon_8\right] \tag{16}$$

$$\hat{A}_2 = \frac{1}{4}\left[\epsilon_1 - \epsilon_3 + \epsilon_5 - \epsilon_7\right] \tag{17}$$

$$\hat{B}_2 = \frac{1}{4}\left[\epsilon_2 - \epsilon_4 + \epsilon_6 - \epsilon_8\right] \tag{18}$$

The foregoing algorithms can be employed to separate and estimate the various RGG error coefficients when these algorithms are applied to RGG output data samples obtained from selected excitation and orientation test conditions. For example, consider the special case where the stator $\overline{xz}$ plane is horizontal and the $\overline{y}$ axis is positive vertical. In this case, the gravity vector direction cosine on $\overline{y}$ (C_{yg}) is negative one, and the remaining two (C_{xg} and C_{zg}) are zero. The resultant coefficients of (4) through (7) are simplified to those given by (19) through (22).

$$A_1 = K_1 n_x + K_2 n_y + K_9 n_z + K_4 \dot{\omega}_x + K_5 \dot{\omega}_y \tag{19}$$

$$B_1 = K_1 n_y - K_2 n_x - K_{10} n_z + K_4 \dot{\omega}_y - K_5 \dot{\omega}_x \tag{20}$$

$$A_2 = 2K_7 n_x + 2K_6 n_y \tag{21}$$

$$B_2 = 2K_7 n_y - 2K_8 n_x \tag{22}$$

When a single excitation function is used for each data set, (19) through (22) may be employed to make estimates of each of the error coefficients in these equations.

LABORATORY TESTS AND COEFFICIENT ESTIMATION

Having discussed some of the non-spinning test concepts, it is appropriate to describe the laboratory tests that are being used to estimate error coefficients. These tests are constrained to two stator orientations ($\bar{z}$ - vertical and horizontal) and to three excitation forms (vertical vibration, horizontal vibration, and angular vibration about the vertical).

In the $\bar{z}$ axis vertical orientation with the $\bar{x}$ axis parallel to the direction of horizontal vibration, the three excitation forms are expressed in stator coordinates by (23), (24), and (25).

$$n_x = n_H \sin \left[\omega_e t + \phi_H\right] \tag{23}$$

$$n_z = n_V \sin \left[\omega_e t + \phi_V\right]$$

$$\dot{\omega}_z = \dot{\omega}_V \sin \left[\omega_e t + \theta_v\right] \tag{25}$$

Under these restricted conditions, the coefficients of (3) through (7) are specialized to (26) through (30).

$$A_0 = K_3 n_V + K_6 \dot{\omega}_V \tag{26}$$

$$A_1 = \left[K_1 \pm K_{10}\right] n_H \tag{27}$$

$$B_1 = \left[-K_2 \mp K_9\right] n_H \tag{28}$$

$$A_2 = 0 \tag{29}$$

$$B_2 = 0 \tag{30}$$

Data samples of RGG output signal changes are obtained for each excitation form, and the algorithms of (11) through (16) are employed to extimate the error coefficients in (26) through (28). Separation of the cross-anisoelastic coefficients is possible if data is obtained for the $\bar{z}$ axis in both the positive and negative vertical orientations. The estimation equations are given by (31) through (36).

$$\hat{K}_3 = \hat{A}_0(n_v)/n_v \tag{31}$$

$$\hat{K}_6 = \hat{A}_0(\dot{\omega}_v)/\dot{\omega}_v$$

$$\hat{K}_1 = \left[\hat{A}_1(n_H)\Big|_{+z} + \hat{A}_1(n_H)\Big|_{-z}\right]/2n_H \tag{33}$$

$$\hat{K}_{10} = \left[\hat{A}_1(n_H)\Big|_{+z} - \hat{A}_1(n_H)\Big|_{-z}\right]/2n_H \tag{34}$$

$$\hat{K}_2 = \left[-\hat{B}_1(n_H)\Big|_{+z} - \hat{B}_1(n_H)\Big|_{-z}\right]/2n_H \tag{35}$$

$$\hat{K}_9 = \left[\hat{B}_1(n_H)\Big|_{-z} - \hat{B}_1(n_H)\Big|_{+z}\right]/2n_H \tag{36}$$

When the z-axis is horizontal and the $\bar{y}$-axis is vertical, the three stator excitation forms are described by (37), (38), and (39).

$$n_x = n_H \sin\left[\omega_e t + \phi_H\right] \tag{37}$$

$$n_y = n_V \sin\left[\omega_e t + \phi_V\right] \tag{38}$$

$$\dot{\omega}_y = \dot{\omega}_V \sin\left[\omega_e t + \theta_V\right] \tag{39}$$

Under these conditions, the coefficients of (3) through (7) are specialized to (40) through (44).

$$A_0 = 0 \tag{40}$$

$$A_1 = K_1 n_H + K_2 n_V + K_5 \dot{\omega}_V \tag{41}$$

$$B_1 = K_1 n_V - K_2 n_H + K_4 \dot{\omega}_V \tag{42}$$

$$A_2 = 2K_7 n_H + 2K_8 n_V \tag{43}$$

$$B_2 = 2K_7 n_V - 2K_8 n_H \tag{44}$$

Data samples of RGG output signal changes are obtained for each excitation form, and the algorithms of (13) through (18) are employed to estimate the error coefficients in (41) through (44). These estimates are presented as (45) through (54).

$$\hat{K}_{1H} = \hat{A}_1(n_H)/n_H \tag{45}$$

$$\hat{K}_{1V} = \hat{B}_1(n_V)/n_V \quad . \tag{46}$$

$$\hat{K}_{2V} = \hat{A}_1(n_V)/n_V \tag{47}$$

$$\hat{K}_{2H} = -\hat{B}_1(n_H)/n_H \tag{48}$$

$$\hat{K}_4 = \hat{B}_1(\dot{\omega}_V)/\dot{\omega}_V \tag{49}$$

$$\hat{K}_5 = \hat{A}_1(\dot{\omega}_V)/\dot{\omega}_V \tag{50}$$

$$\hat{K}_{7H} = \hat{A}_2(n_H)/2n_H \tag{51}$$

$$\hat{K}_{7V} = \hat{B}_2(n_V)/2n_V \tag{52}$$

$$\hat{K}_{8V} = \hat{A}_2(n_V)/2n_V \tag{53}$$

$$\hat{K}_{8H} = -\hat{B}_2(n_H)/2n_H \tag{54}$$

SCALE FACTOR ESTIMATION

Earlier it was stated that the non-spinning test concepts are based on a priori knowledge of the RGG signal process transfer functions. In particular, the accuracy with which arm mass balance adjustments can be determined from the error coefficient estimates depends directly on the scale factor between differential torque inputs and RGG signal outputs. Fortunately, a method of estimating this scale factor from a test of the non-spinning RGG has been devised.

This scale factor estimation technique is based on the use of transverse angular velocities to produce, accurately, known rotational field gradient inputs. The rotational field input gradient to the RGG differential mode is defined by (35) in rotor coordinates.

$$\Delta\Gamma_{ij}\Big|_{\omega} = -\omega_i\omega_j \tag{55}$$

When the stator $\bar{z}$-axis is horizontal and the $\bar{y}$-axis is vertical, a periodic angular velocity about the vertical (ω_V) produces the rotor angular velocity components defined by (56) and (57) as a function of the relative rotor angle (α).

$$\omega_i = \omega_V \sin \alpha \tag{56}$$

$$\omega_j = \omega_V \cos \alpha \tag{57}$$

Substitution of (56) and (57) into (55) yields the input gradient function of (58).

$$\Delta\Gamma_{ij}\Big|_{\omega} = -\frac{1}{2}\omega_V^2 \sin 2\alpha \tag{58}$$

If the excitation frequency is set equal to one-half the differential mode resonant frequency ($\omega_0/2$), the input gradient function will contain a component at the difference mode resonant frequency which will propagate through the RGG signal process with the same scale factor as do the other non-spinning test signals. The input angular velocity and its square are shown in (59) and (60).

$$\omega_V \triangleq W \sin\left[\frac{\omega_0 t}{2} + \phi\right] \tag{59}$$

$$\omega_v^2 = \frac{1}{2} W^2 \left[1 - \cos\left[\omega_0 t + 2\phi\right]\right] \tag{60}$$

Substitution of the periodic component of (60) into (58) yields the input rotational field gradient of (60).

$$\Delta\Gamma_{ij}\Big|_{\omega} = \frac{1}{4} W^2 \sin 2\alpha \cos\left[\omega_0 t + 2\phi\right] \tag{61}$$

This input gradient function leads to the principal and cross-gradient output functions given by (62) and (63), respectively.

$$G_p = -\frac{1}{4} W^2 \sin 2\alpha \sin 2\phi \tag{62}$$

$$G_c = +\frac{1}{4} W^2 \sin 2\alpha \cos 2\phi \tag{63}$$

When the rotor angle (α) is set to odd multiples of $\pm 45^\circ$, the input rotational field gradient amplitude is maximized at $W^2/4$. This yields a very respectable input gradient amplitude for practical input rate levels. For example, a peak rate of one milliradian per second has an associated input gradient amplitude of 250 EU. It is anticipated that with this amplitude, the scale factor can be estimated to within a few percent without difficulty.

COEFFICIENT ESTIMATION SUMMARY

In practice, the transverse motion sensitivities (K_1, K_2, K_4, K_5, K_7, K_8) are estimated with the $\bar{z}$-axis horizontal, and the axial motion sensitivities (K_3 and K_6) are estimated with the $\bar{z}$ axis vertical. With the $\bar{z}$-axis horizontal and the $\bar{y}$-axis vertical, the rotor is locked to the stator such that their reference coordinates coincide. This position of the rotor defines the zero of the relative rotor angle (α). The stator is then subjected to the excitation functions of (37), (38), and (39) with the excitation frequency set equal to the differential mode resonant frequency of the RGG. The output signal changes for each excitation form are observed and recorded. The rotor position is indexed by 45°, and the process is repeated until eight data points for each of the three excitation forms are obtained. This data array is modeled by Table C-1 which lists the output signal changes (ϵ) for each excitation form and for each rotor orientation angle (α).

The coefficient estimates are obtained from (45) through (54) using the general algorithms of (13) through (18). The specific estimation equations using the data of Table C-1 are given by (64) through (73).

Table C-1. Output Signal Data Array

α	Outputs due to Indicated Excitation Form		
	n_H	$\dot{\omega}_V$	n_V
0	ϵ_{1H}	ϵ_{1W}	ϵ_{1V}
45	ϵ_{2H}	ϵ_{2W}	ϵ_{2V}
90	ϵ_{3H}	ϵ_{3W}	ϵ_{3V}
135	ϵ_{4H}	ϵ_{4W}	ϵ_{4V}
180	ϵ_{5H}	ϵ_{5W}	ϵ_{5V}
225	ϵ_{6H}	ϵ_{6W}	ϵ_{6V}
270	ϵ_{7H}	ϵ_{7W}	ϵ_{7V}
315	ϵ_{8H}	ϵ_{8W}	ϵ_{8V}

T2148

$$\hat{K}_{1H} = \left[\epsilon_{1H} - \epsilon_{5H}\right]/2n_H \tag{64}$$

$$\hat{K}_{1V} = \left[\epsilon_{3V} - \epsilon_{7V}\right]/2n_V \tag{65}$$

$$\hat{K}_{2V} = \left[\epsilon_{1V} - \epsilon_{5V}\right]/2n_V \tag{66}$$

$$\hat{K}_{2H} = \left[\epsilon_{7H} - \epsilon_{3H}\right]/2n_H \tag{67}$$

$$\hat{K}_{4} = \left[\epsilon_{3W} - \epsilon_{7W}\right]/2\dot{\omega}_V \tag{68}$$

$$\hat{K}_{5} = \left[\epsilon_{1W} - \epsilon_{5W}\right]/2\dot{\omega}_V \tag{69}$$

$$\hat{K}_{7H} = \left[\epsilon_{1H} - \epsilon_{3H} + \epsilon_{5H} - \epsilon_{7H}\right]/8n_H \tag{70}$$

$$\hat{K}_{7V} = \left[\epsilon_{2V} - \epsilon_{4V} + \epsilon_{6V} - \epsilon_{8V}\right]/8n_V \tag{71}$$

$$\hat{K}_{8V} = \left[\epsilon_{1V} - \epsilon_{3V} + \epsilon_{5V} - \epsilon_{7V}\right]/8n_V \tag{72}$$

$$\hat{K}_{8H} = \left[\epsilon_{4H} - \epsilon_{2H} + \epsilon_{8H} - \epsilon_{6H}\right]/8n_H \tag{73}$$

As stated previously, the axial motion sensitivities (K_3, K_6) are estimated from data taken with the $\bar{z}$-axis vertical. Only two excitation forms are used for this process (n_V, $\dot{\omega}_V$). Once again the rotor is indexed to eight uniformly spaced positions, and the RGG signal output changes for each excitation form in each of the eight positions is recorded.

The desired coefficient estimates are based on (31) and (32) using the average of (11) and (12). The specific estimation equations are given by (74) and (75).

$$\hat{K}_3 = \left[\epsilon_{1V} + \epsilon_{2V} + \epsilon_{3V} + \epsilon_{4V} + \epsilon_{5V} + \epsilon_{6V} + \epsilon_{7V} + \epsilon_{8V}\right]/8n_V \tag{74}$$

$$\hat{K}_6 = \left[\epsilon_{1W} + \epsilon_{2W} + \epsilon_{3W} + \epsilon_{4W} + \epsilon_{5W} + \epsilon_{6W} + \epsilon_{7W} + \epsilon_{8W}\right]/8\dot{\omega}_V \tag{75}$$

ADJUSTMENT INFLUENCE EQUATIONS

The RGG arm mass balance configuration constrains the available changes of mass distribution to planes normal to the RGG torsion axis. Each end mass has adjustment screws whose positions can be changed in one direction only (either radially or tangentially). The net results of changes in the adjustment screw positions are the first moment changes of each arm shown in (76) and (77) in terms of the net changes in the radial and tangential first moments.

$$\overline{\delta P}_1 = \bar{i}\delta P_{1r} + \bar{j}\delta P_{1t} \tag{76}$$

$$\overline{\delta P}_2 = \bar{i}\delta P_{2t} + \bar{j}\delta P_{2r} \tag{77}$$

The concomittant second moment changes are proportional to the first moment changes and to the axial positions (h_r and h_t) of the radial and tangential first moment changes as in (78) and (79).

$$\delta\left[\Delta\Phi_{ik}\right] = -h_r\delta P_{1r} - h_t\delta P_{2t} \tag{78}$$

$$\delta\left[\Delta\Phi_{jk}\right] = -h_r\delta P_{2r} - h_t\delta P_{1t} \tag{79}$$

The first and second moment changes in (76) through (79) produce changes in the differential and dynamic arm mass balance coefficients as in (80) through (83).

$$\delta K_1 = \left[g/\eta C\right]\left[\delta P_{1t} - \delta P_{2r}\right] \tag{80}$$

$$\delta K_2 = \left[g/\eta C\right]\left[\delta P_{2t} - \delta P_{1r}\right] \tag{81}$$

$$\delta K_4 = \left[h_r\delta P_{1r} + h_t\delta P_{2t}\right]/\eta C \tag{82}$$

$$\delta K_5 = \left[h_r\delta P_{2r} + h_t\delta P_{1t}\right]/\eta C \tag{83}$$

In order to determine the mass moment changes required to reduce a set of coefficient estimates to zero, simply replace the coefficient increments in (80) through (83) with the negative of the coefficient estimates and solve the resultant set of equations for the required first moment changes. This solution is presented as (84) through (87).

$$\delta\hat{P}_{1r} = \left[\frac{h_t}{h_t + h_r}\right]\left[\frac{\eta C}{g}\right]\hat{K}_2 - \left[\frac{\eta C}{h_t + h_r}\right]\hat{K}_4 \tag{84}$$

$$\delta\hat{P}_{1t} = -\left[\frac{h_r}{h_t + h_r}\right]\left[\frac{\eta C}{g}\right]\hat{K}_1 - \left[\frac{\eta C}{h_t + h_r}\right]\hat{K}_5 \tag{85}$$

$$\delta P_{2r} = \left[\frac{h_t}{h_t + h_r}\right]\left[\frac{\eta C}{g}\right]\hat{K}_1 - \left[\frac{\eta C}{h_t + h_r}\right]\hat{K}_5 \tag{86}$$

$$\delta P_{2t} = -\left[\frac{h_r}{h_t + h_r}\right]\left[\frac{\eta C}{g}\right]\hat{K}_2 - \left[\frac{\eta C}{h_t + h_r}\right]\hat{K}_4 \tag{87}$$

The sum-mode mismatch coefficient (K_6) is a function of the difference of the arm polar inertias ($\Delta\Phi_{kk}$), and the differential polar inertia change required by the estimate of this coefficient is given in (88). As indicated, this sensitivity is a function of the sum-mode natural frequency (β_0) and the difference-mode natural frequency (ω_0).

$$\delta(\widehat{\Delta\Phi}_{kk}) = -\eta C\left[\frac{\omega_0^2}{\beta_0^2} - 1\right]\hat{K}_6 \tag{88}$$

Application of (84) through (88) requires quantification of the parameters in these equations. The latest parameters for RGG-2 are as follows:

$C = 38,268$ gm - cm^2

$\omega_0 = 217.8$ rad/sec

$\beta_0 = 138.5$ rad/sec

$h_t = 1.933$ cm (outer-coarse)

$h_t = 1.140$ cm (inner-coarse)

$h_r = 3.073$ cm (outer-coarse)

$h_r = 0.000$ cm (inner-coarse)

$$h_t = 1.933 \text{ cm (fine)}$$

$$h_r = 2.502 \text{ cm (fine)}$$

When the first moment changes are constrained to the outer-coarse adjustment screws, (89) through (92) apply. When the fine adjustment screws are used, (93) through (96) apply. In these equations, the mass moment changes are in gm-cm, and the error coefficients are in EU/g or EU-sec^2.

$$\delta\hat{P}_{1r} = 10^{-8}\left[1.51\,\hat{K}_2 - 764\,\hat{K}_4\right] \tag{89}$$

$$\delta\hat{P}_{1t} = 10^{-8}\left[-2.40\,\hat{K}_1 - 764\,\hat{K}_5\right] \tag{90}$$

$$\delta\hat{P}_{2r} = 10^{-8}\left[1.51\,\hat{K}_1 - 764\,\hat{K}_5\right] \tag{91}$$

$$\delta\hat{P}_{2t} = 10^{-8}\left[-2.40\,\hat{K}_2 - 764\,\hat{K}_4\right] \tag{92}$$

$$\delta\hat{P}_{1r} = 10^{-8}\left[1.70\,\hat{K}_2 - 863\,\hat{K}_4\right] \tag{93}$$

$$\delta\hat{P}_{1t} = 10^{-8}\left[-2.20\,\hat{K}_1 - 863\,\hat{K}_5\right] \tag{94}$$

$$\delta\hat{P}_{2r} = 10^{-8}\left[1.70\,\hat{K}_1 - 863\,\hat{K}_5\right] \tag{95}$$

$$\delta\hat{P}_{2t} = 10^{-8}\left[-2.20\,\hat{K}_2 - 863\,\hat{K}_4\right] \tag{96}$$

The differential polar moment sensitivity for RGG-2 is obtained by substituting the appropriate parameters into (88). The result is given by (97) where the units are (gm-cm^2) and (EU-sec^2).

$$\delta(\widehat{\Delta\Phi}_{kk}) = -5.637 \times 10^{-5}\,\hat{K}_6 \tag{97}$$

The individual balance-screw turns required to obtain the calculated first and second moment changes are not unique. However, a unique method of determining balance changes has been established, and this has proven successful in actual practice. For convenience in describing the process, it is divided into two parts. In the first part, the radial and tangential adjustment screws on each arm are assumed to move as four individual groups to satisfy (89) through (92) or (93) through (96). In the second part, the changes required to satisfy (97) (on the basis of a minimum polar inertia change) are determined.

Generally there are four adjustment screws of equal mass in each group. The number of turns required for each screw in a group for part one of the procedure are obtained from (98) as a function of the required first moment change ($\widehat{\delta P}$), the individual screw mass (m), and the screw pitch ($\Delta\theta/\Delta h$).

$$|\delta\theta| = \left[\frac{\Delta\theta}{\Delta h}\right]\left[|\widehat{\delta P}| \;/4m\right] \tag{98}$$

For the second part of the procedure, it has been determined that the most practical technique is to adjust the differential polar inertia with one group of screws on one arm only. This technique has the potential benefit of minimizing the resultant uncertainty in the final adjustment by minimizing the number of screws to be adjusted. All of the four screws in the group used to satisfy (97) are to be moved in the outward or inward direction such that no first moment changes occur. The required screw turns are obtained from (99) as a function of the required polar moment change ($\widehat{\delta\Delta\Phi}_{kk}$), the individual screw mass (m), the total average displacement of the screw in the adjustment direction (h_0) from the arm axes of symmetry, and the screw pitch ($\Delta\theta/\Delta h$).

$$|\delta\theta| = \left[\frac{\Delta\theta}{\Delta h}\right]\left[|\widehat{\delta\Delta\Phi}_{kk}|\right]/8mh_0 \tag{99}$$

The balance screw turns calculated on the basis of (98) and (99) are combined linearly into one set of adjustments, and the results are rounded to the resolution limit of the adjustments. In order to validate the resolution-limited adjustments, the actual moment changes that they produce are calculated. These moment changes are then used to calculate the resultant error coefficient changes for comparison with the original coefficient estimates used as input data.

APPENDIX D

TARE WEIGHT SELECTION FOR INITIAL ARM BALANCING

INTRODUCTION

It has been determined through experience that the initial arm balance of the RGG should be accomplished by adding tare weights of selected mass to the arms at predesignated positions on the arms. During this process, the normal balance screws are located at their center positions for use in subsequent balance iterations. The purpose of this appendix is to describe a method of tare weight selection based on prior knowledge of the position of each tare weight mass center and based on the prior estimates of certain motion sensitivity coefficients.

TARE WEIGHT POSITIONS AND COORDINATES

Each arm has (by definition) four coplanar tare weight positions. Each tare weight mass center is displaced radially from the arm polar axis ($\bar{k}$) by a fixed distance (r_0), and each of these radial directions is displaced by the angle (α) from the longitudinal axis of symmetry of each arm. Additionally, each tare weight plane is displaced from the RGG rotor reference plane by the axial distance (l_0), positively for arm No. 1 and negatively for arm No. 2 in terms of the rotor axial reference axis ($\bar{k}$).

For convenience in tare weight selection, two non-orthogonal coordinate sets are defined in Figure D-1 by the unit vectors u_1, v_1, and $\bar{u}_2$, $\bar{v}_2$. These unit vectors concide with lines joining tare weight pairs such that the first mass moments of the tare weights may be expressed directly in terms of tare weight mass differences in the non-orthogonal coordinate sets. As will be discussed later, this approach eases the difficulty of selecting eight tare weights to adjust five coefficients.

PRECEDING PAGE BLANK-NOT FILMED

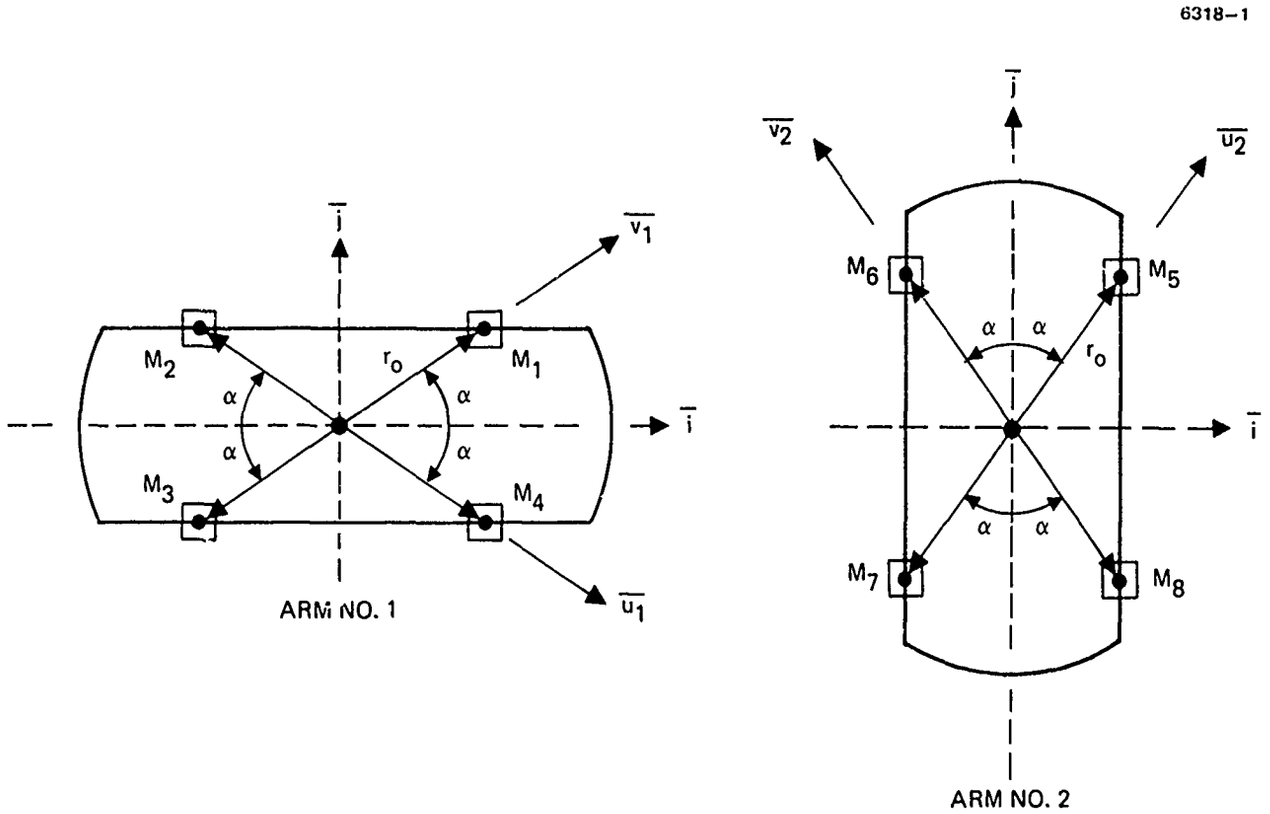

Figure D-1. Tare weight positions.

FIRST MOMENT EQUATIONS

The first moments of each arm must be changed to reduce the differential and dynamic arm mass unbalance coefficients (K_1, K_2 and K_4, K_5) on the basis of prior estimates of these parameters. The changes in these parameters which result from the first moment changes on each arm are described by equations (1) through (4).

$$\Delta K_1 = (g/\eta C)\left[\Delta p_{j1} - \Delta p_{j2}\right] \tag{1}$$

$$\Delta K_2 = (g/\eta C)\left[\Delta p_{i2} - \Delta p_{i1}\right] \tag{2}$$

$$\Delta K_4 = (l_0/\eta C)\left[\Delta p_{i1} + \Delta p_{i2}\right] \tag{3}$$

$$\Delta K_5 = (l_0/\eta C)\left[\Delta p_{j1} + \Delta p_{j2}\right] \tag{4}$$

The first moment changes in (1) through (4) are related to the tare weight first moments by (5) through (8).

$$\Delta p_{i1} = \left[\Delta p_{u1} + \Delta p_{v1}\right] \cos\alpha \tag{5}$$

$$\Delta p_{j1} = \left[\Delta p_{v1} - \Delta p_{u1}\right] \sin\alpha$$

$$\Delta p_{i2} = \left[\Delta p_{u2} - \Delta p_{v2}\right] \sin\alpha \tag{7}$$

$$\Delta p_{j2} = \left[\Delta p_{u2} + \Delta p_{v2}\right] \cos\alpha \tag{8}$$

The first moment changes should be selected such that the resultant coefficient changes are equal and opposite to the coefficient estimates. When this constraint is imposed on (1) through (8), the required tare weight first moments are related to the coefficient estimates by (9) through (12).

$$\left[\Delta p_{u2} + \Delta p_{v2}\right] \cos\alpha + \left[\Delta p_{u1} - \Delta p_{v1}\right] \sin\alpha = \left[\eta C/g\right] \hat{K}_1 \quad (9)$$

$$\left[\Delta p_{u1} + \Delta p_{v1}\right] \cos\alpha + \left[\Delta p_{v2} - \Delta p_{u2}\right] \sin\alpha = \left[\eta C/g\right] \hat{K}_2 \quad (10)$$

$$\left[\Delta p_{v2} - \Delta p_{u2}\right] \sin\alpha - \left[\Delta p_{u1} + \Delta p_{v1}\right] \cos\alpha = \left[\eta C/l_0\right] \hat{K}_4 \quad (11)$$

$$\left[\Delta p_{u1} - \Delta p_{v1}\right] \sin\alpha - \left[\Delta p_{u2} + \Delta p_{v2}\right] \cos\alpha = \left[\eta C/l_0\right] \hat{K}_5 \quad (12)$$

In order to select the tare weights on the basis of (9) through (12), it is convenient to describe the tare weight first moments in terms of the radial position (r_0) and the mass differences on each coordinate, i.e., M_{u1}, M_{v1}, M_{u2}, M_{v2} as in (13) through (16).

$$\Delta p_{u1} = r_0 M_{u1} \quad (13)$$

$$\Delta p_{v1} = r_0 M_{v1} \quad (14)$$

$$\Delta p_{u2} = r_0 M_{u2} \quad (15)$$

$$\Delta p_{v2} = r_0 M_{v2} \quad (16)$$

When (13) through (16) are substituted into (9) through (12), an equation set for the tare weight mass differences is obtained as shown in (17) through (20).

$$\left[M_{u2} + M_{v2}\right] \cos\alpha + \left[M_{u1} - M_{v1}\right] \sin\alpha = \left[\eta C/g r_0\right] \hat{K}_1 \quad (17)$$

$$\left[M_{u1} + M_{v1}\right] \cos\alpha + \left[M_{v2} - M_{u2}\right] \sin\alpha = \left[\eta C/g r_0\right] \hat{K}_2 \quad (18)$$

$$\left[M_{v2} - M_{u2}\right] \sin\alpha - \left[M_{u1} + M_{v1}\right] \cos\alpha = \left[\eta C/l_0 r_0\right] \hat{K}_4 \quad (19)$$

$$\left[M_{u1} - M_{v1}\right] \sin\alpha - \left[M_{u2} + M_{v2}\right] \cos\alpha = \left[\eta C/l_0 r_0\right] \hat{K}_5 \quad (20)$$

The solution of (17) through (20) may be expressed in terms of four constants (A_1, A_2, A_3, A_4) as shown in (21) through (25).

$$A_1 \triangleq \left[\eta C/4gr_0 \sin\alpha\right] \quad (21)$$

$$A_2 \triangleq \left[\eta C/4gr_0 \cos\alpha\right] \quad (22)$$

$$A_3 \triangleq \left[\eta C/4l_0 r_0 \sin\alpha\right] \quad (23)$$

$$A_4 \triangleq \left[\eta C/4l_0 r_0 \cos\alpha\right] \quad (24)$$

$$\begin{bmatrix} M_{u1} \\ M_{v1} \\ M_{u2} \\ M_{v2} \end{bmatrix} = \begin{bmatrix} A_1 & A_2 & -A_4 & A_3 \\ -A_1 & A_2 & -A_4 & -A_3 \\ A_2 & -A_1 & -A_3 & -A_4 \\ A_2 & A_1 & A_3 & -A_4 \end{bmatrix} \begin{bmatrix} \hat{K}_1 \\ \hat{K}_2 \\ \hat{K}_4 \\ \hat{K}_5 \end{bmatrix} \quad (25)$$

POLAR MOMENT EQUATIONS

The polar moment difference of the arms must be changed to reduce the sum-mode mismatch coefficient (K_6) within the constraints imposed by the first moment requirements described in the previous section. The sum-mode mismatch coefficient change produced by a change in the difference of the arm polar moments is described by (26).

$$\Delta K_6 = \left[\frac{\beta_0^2}{\omega_0^2 - \beta_0^2}\right] \left[\frac{\Delta\Phi_1 - \Delta\Phi_2}{\eta C}\right] \quad (26)$$

The required polar moment change is just the negative of the sum-mode mismatch coefficient estimate ($\hat{K}_6$) as described by (27).

$$\left[\Delta\Phi_1 - \Delta\Phi_2\right] = \eta C \left[1 - \left[\frac{\omega_0}{\beta_0}\right]^2\right] \hat{K}_6 \tag{27}$$

where

ω_0 = Differential Mode Natural Frequency

β_0 = Sum Mode Natural Frequency

The polar moment changes that arise by adding the tare weights may be written directly from Figure D-1 as (28) and (29).

$$\Delta\Phi_1 = r_0^2 \left[m_1 + m_2 + m_3 + m_4\right] \tag{28}$$

$$\Delta\Phi_2 = r_0^2 \left[m_5 + m_6 + m_7 + m_8\right] \tag{29}$$

A unique solution for the required tare weight masses does not exist, but a unique method of tare weight selection does exist! The method is based on the use of a common, but arbitrary, additive mass at each tare weight location. These additive masses are designated as Δm_1 for arm No. 1 and Δm_2 for arm No. 2. The individual masses are expressed in terms of the previously defined differential masses as follows:

$$m_1 = \left[\Delta m_1 + M_{v1}\right] \;\&\; m_3 = \Delta m_1 \;;\; M_{v1} > 0$$

$$m_1 = \Delta m_1 \;\&\; m_3 = \left[\Delta m_1 - M_{v1}\right] \;;\; M_{v1} < 0$$

$$m_2 = \Delta m_1 \;\&\; m_4 = \left[\Delta m_1 + M_{u1}\right] \;;\; M_{u1} > 0$$

$$m_2 = \left[\Delta m_1 - M_{u1}\right] \;\&\; m_4 = \Delta m_1 \;;\; M_{u1} < 0$$

Using the above definitions for the individual tare weight masses on arm No. 1, it is possible to express the polar moment change of (28) by (30).

$$\Delta\Phi_1 = r_0^2\left[4\Delta m_1 + |M_{u1}| + |M_{v1}|\right] \tag{30}$$

Similarly, the individual tare weight masses on arm No. 2 are defined in terms of the differential masses $\left[M_{u2} \text{ and } M_{v2}\right]$ and the additive mass $\left[\Delta m_2\right]$ as follows:

$$m_5 = \left[\Delta m_2 + M_{u2}\right] \;\&\; m_7 = \Delta m_2 \;;\; M_{u2} > 0$$

$$m_5 = \Delta m_2 \;\&\; m_7 = \left[\Delta m_2 - M_{u2}\right] \;;\; M_{u2} < 0$$

$$m_6 = \left[\Delta m_2 + M_{v2}\right] \;\&\; m_8 = \Delta m_2 \;;\; M_{v2} > 0$$

$$m_6 = \Delta m_2 \;\&\; m_8 = \left[\Delta m_2 - M_{v2}\right] \;;\; M_{v2} < 0$$

The polar moment change of (29) is expressed as (31).

$$\Delta\Phi_2 = r_0^2\left[4\Delta m_2 + |M_{u2}| + |M_{v2}|\right] \tag{31}$$

Now take the difference between (30) and (31) and substitute the result into (27) to obtain (32).

$$\eta C\left[1 - \frac{\omega_0^2}{\beta_0^2}\right]\hat{K}_6 = 4r_0^2\left[\Delta m_1 - \Delta m_2\right] + r_0^2\left[|M_{u1}| + |M_{v1}| - |M_{u2}| - |M_{v2}|\right] \tag{32}$$

The additive mass difference is obtained from (32) as (33).

$$\left[\Delta m_1 - \Delta m_2\right] = \left[\frac{\eta C \hat{K}_6}{4r_0^2}\right]\left[1 - \frac{\omega_0^2}{\beta_0^2}\right] - \frac{1}{4}\left[|M_{u1}| + |M_{v1}| - |M_{u2}| - |M_{v2}|\right] \tag{33}$$

If the rhs of (33) is positive, Δm_2 can be set to zero to yield a unique solution for Δm_1; and if the rhs of (33) is negative, setting Δm_1 to zero gives a unique solution for Δm_2. Once the additive masses (Δm_1, Δm_2) are defined, all of the individual tare weight masses are defined by the logic statements preceeding (30) and (31).

SUMMARY OF TARE WEIGHT SELECTION

The tare weight selection process is straight forward using the following recipe:

Input Data

Solve for (A_1, A_2, A_3, A_4) from (21) through (24).

Coefficient estimates ($\hat{K}_1$, $\hat{K}_2$, $\hat{K}_4$, $\hat{K}_5$, $\hat{K}_6$).

Differential Mass Parameters

Solve for $\left[M_{u1}, M_{v1}, M_{u2}, M_{v2}\right]$ from (25).

Additive Mass Parameters

Solve for ($\Delta m_1 - \Delta m_2$) from (33) and select Δm_1 and Δm_2.

Tare Weight Mass Selection

Use differential and additive mass parameters in logic statements preceeding (30) and (31) to define tare weight masses.

TARE WEIGHT GEOMETRY

The tare weight geometrical parameters for RGG-1 and RGG-1S may be derived from the following definitions:

$$r_0 = 5.558 \text{ cm}$$

$$r_0 \sin \alpha = 1.816 \text{ cm}$$

$$r_0 \cos \alpha = 5.253 \text{ cm}$$

$$l_0 = 1.653 \text{ cm}$$

$$\eta C = 4.1 \times 10^4 \text{ gm - cm}^2$$

The resultant parameters computed from (21) through (24) are as follows:

$$A_1 = 5.76 \times 10^{-9} \text{ gm/(EU/g)}$$

$$A_2 = 1.99 \times 10^{-9} \text{ gm/(EU/g)}$$

$$A_3 = 3.42 \times 10^{-6} \text{ gm/(EU-Sec}^2\text{)}$$

$$A_4 = 1.18 \times 10^{-6} \text{ gm/(EU-Sec}^2\text{)}$$

The tare weight parameters for RGG-2 are computed from (21) through (24) using the following constants:

$$r_0 = 5.486 \text{ cm}$$

$$r_0 \sin \alpha = 1.580 \text{ cm}$$

$$r_0 \cos \alpha = 5.253 \text{ cm}$$

$$l_0 = 1.140 \text{ cm}$$

$$\eta C = 3.8268 \times 10^4 \text{ gm - cm}^2$$

The resulting parameters for RGG-2 are as follows:

$$A_1 = 6.18 \times 10^{-9} \text{ gm/(EU/g)}$$

$$A_2 = 1.86 \times 10^{-9} \text{ gm/(EU/g)}$$

$$A_3 = 5.31 \times 10^{-6} \text{ gm/(EU-Sec}^2\text{)}$$

$$A_4 = 1.60 \times 10^{-6} \text{ gm/(EU-Sec}^2\text{)}$$

COEFFICIENT CHANGE VERIFICATION

After the tare weights have been selected, it is advisable to calculate the resultant influence on the RGG motion sensitivity coefficients to ensure that the calculated coefficient changes are approximately equal in magnitude and of opposite sign to the original coefficient estimates. This objective is accomplished without difficulty in two steps: (1) calculate the appropriate mass moment changes for each arm and (2) calculate the motion sensitivity changes from the mass moment changes.

The mass moment changes for each arm may be written directly from Figure 1 as follows:

$$\Delta P_{i1} = r_0 \cos \alpha \left[m_1 + m_4 - m_2 - m_3 \right] \tag{33}$$

$$\Delta P_{j1} = r_0 \sin \alpha \left[m_1 + m_2 - m_3 - m_4 \right] \tag{34}$$

$$\Delta P_{i2} = r_0 \sin \alpha \left[m_5 + m_8 - m_6 - m_7 \right] \tag{35}$$

$$\Delta P_{j2} = r_0 \cos \alpha \left[m_5 + m_6 - m_7 - m_8 \right] \tag{36}$$

$$\Delta \Phi_1 = r_0^2 \left[m_1 + m_2 + m_3 + m_4 \right] \tag{37}$$

$$\Delta \Phi_2 = r_0^2 \left[m_5 + m_6 + m_7 + m_8 \right] \tag{38}$$

The resultant coefficient changes are defined by (1) through (4) and by (26). These equations are repeated here for convenience.

$$\Delta K_1 = (g/\eta C) \left[\Delta P_{j1} - \Delta P_{j2} \right] \tag{1}$$

$$\Delta K_2 = (g/\eta C) \left[\Delta P_{i2} - \Delta P_{i1} \right] \tag{2}$$

$$\Delta K_4 = (l_0/\eta C) \left[\Delta P_{i1} + \Delta P_{i2} \right] \tag{3}$$

$$\Delta K_5 = (l_0/\eta C) \left[\Delta P_{j1} + \Delta P_{j2} \right] \tag{4}$$

$$\Delta K_6 = \left[\frac{\beta_0^2}{\omega_0^2 - \beta_0^2} \right] \left[\frac{\Delta \Phi_1 - \Delta \Phi_2}{\eta C} \right] \tag{26}$$

The numerical coefficients required to evaluate the mass moment changes and coefficient changes were defined previously for both RGG-1 and RGG-2 with the exception of the sum and difference mode natural frequencies (β_0 and ω_0). These frequencies are estimated for each RGG to be as follows:

Unit	β_0(rad/sec)	ω_0(rad/sec)
RGG-1	120.0	223.0
RGG-2	138.5	217.8

☆U. S. GOVERNMENT PRINTING OFFICE: 1977--760-002--105